

AD-A116 670

TECHNICAL LIBRARY AD A-116 670



DETERMINATION OF MATERIAL PROPERTIES BY LIMITED SCAN X-RAY TOMOGRAPHY

SCIENTIFIC SYSTEMS, INC.
54 RINDGE AVENUE EXTENSION
CAMBRIDGE, MA 02140

SEPTEMBER 1981

TECHNICAL REPORT AFWAL-TR-81-4050
Final Report for Period September 1979 — January 1981

Approved for public release; distribution unlimited

MATERIALS LABORATORY
AIR FORCE WRIGHT AERONAUTICAL LABORATORIES
AIR FORCE SYSTEMS COMMAND
WRIGHT-PATTERSON AIR FORCE BASE, OHIO 45433

NOTICE

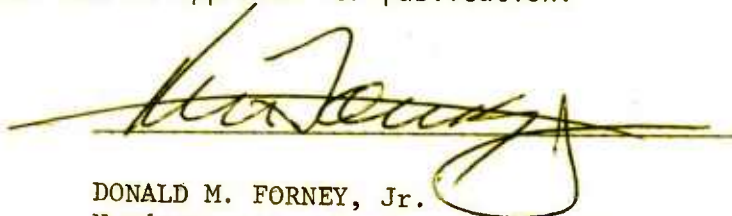
When Government drawings, specifications, or other data are used for any purpose other than in connection with a definitely related Government procurement operation, the United States Government thereby incurs no responsibility nor any obligation whatsoever; and the fact that the government may have formulated, furnished, or in any way supplied the said drawings, specifications, or other data, is not to be regarded by implication or otherwise as in any manner licensing the holder or any other person or corporation, or conveying any rights or permission to manufacture use, or sell any patented invention that may in any way be related thereto.

This report has been reviewed by the Office of Public Affairs (ASD/PA) and is releasable to the National Technical Information Service (NTIS). At NTIS, it will be available to the general public, including foreign nations.

This technical report has been reviewed and is approved for publication.

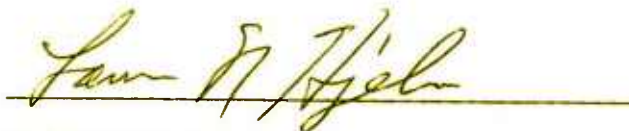


Robert L. Crane
Project Engineer



DONALD M. FORNEY, Jr.
Nondestructive Evaluation Branch
Metals and Ceramics Division

FOR THE COMMANDER



LAWRENCE N. HJELM, Asst. Chief
Metals and Ceramics Division
Materials Laboratory

"If your address has changed, if you wish to be removed from our mailing list, or if the addressee is no longer employed by your organization please notify AFWAL/MLLP, W-PAFB, OH 45433 to help us maintain a current mailing list".

Copies of this report should not be returned unless return is required by security considerations, contractual obligations, or notice on a specific document.

REPORT DOCUMENTATION PAGE		READ INSTRUCTIONS BEFORE COMPLETING FORM
1. REPORT NUMBER AFWAL-TR-81-4050	2. GOVT ACCESSION NO.	3. RECIPIENT'S CATALOG NUMBER
4. TITLE (and Subtitle) DETERMINATION OF MATERIAL PROPERTIES BY LIMITED SCAN X-RAY TOMOGRAPHY		5. TYPE OF REPORT & PERIOD COVERED Final Report Sept 79 - Jan 81
		6. PERFORMING ORG. REPORT NUMBER
7. AUTHOR(s) Wolfram Jarisch, PhD		8. CONTRACT OR GRANT NUMBER(s) F33615-79-C-5132
9. PERFORMING ORGANIZATION NAME AND ADDRESS Scientific Systems, Incorporated 54 Rindge Avenue Extension Cambridge, MA 02140		10. PROGRAM ELEMENT, PROJECT, TASK AREA & WORK UNIT NUMBERS 24180604
11. CONTROLLING OFFICE NAME AND ADDRESS Materials Laboratory (AFWAL/MLLP) AF Wright Aeronautical Laboratories (AFSC) Wright-Patterson AFB, Ohio 45433		12. REPORT DATE September 1981
		13. NUMBER OF PAGES 133
14. MONITORING AGENCY NAME & ADDRESS (if different from Controlling Office)		15. SECURITY CLASS. (of this report) Unclassified
		15a. DECLASSIFICATION/DOWNGRADING SCHEDULE
16. DISTRIBUTION STATEMENT (of this Report) Approved for public release; distribution unlimited.		
17. DISTRIBUTION STATEMENT (of the abstract entered in Block 20, if different from Report)		
18. SUPPLEMENTARY NOTES		
19. KEY WORDS (Continue on reverse side if necessary and identify by block number) Computed tomography; nondestructive evaluation; X-radiography; carbon/carbon		
20. ABSTRACT (Continue on reverse side if necessary and identify by block number) The purpose of this program was to explore methods of increasing the speed of the computed tomography (C/T) inspection process. The report presents an analysis of a translational data collection scheme and compares that to the tradition rotation data taken when used in most C/T machinery.		

FOREWORD

This work was performed under Materials Laboratory Contract F33615-79-C-5132 with Project, Task Area and Work Unit Numbers assigned as 2418 06 04. The Air Force project manager was Dr R. L. Crane, AFWAL/MLLP. and the work was conducted by Scientific Systems, Inc., Cambridge, Mass. The Program Manager and Principle Investigator was Dr Wolfran Jarisch.

TABLE OF CONTENTS

	<u>page</u>
1. INTRODUCTION.....	2
2. BASIC CONSIDERATIONS ABOUT PROJECTIONS.....	7
2.1 Use of Projections in Image Reconstruction.....	7
2.2 The limited scan approach - deterministic aspect.....	10
2.3 Probabilistic approaches.....	18
2.3.1 Decision theoretic approach.....	33
2.3.2 Distribution of quadratic and bilinear terms..	37
2.3.3 Simplified models.....	43
3. PHYSICAL ASPECTS OF PROBLEM.....	50
3.1 X-ray Sources.....	50
3.2 Properties of X-rays Absorption and Secondary Radiation.....	63
3.3 Scattering of X-rays.....	68
3.4 Measurement of X-rays.....	77
4. STRUCTURAL MODELING.....	83
4.1 Modeling of Object.....	83
4.2 Modeling Projection.....	88
4.3 Basic Signal-to-Noise considerations.....	97
4.3.1 Concept of optimal beams hardness.....	97
4.3.2 Selection of best projection.....	100
4.3.3 The relation of Noise terms to multiscan.....	100
4.3.4 Uncertainty in multiscan when beams overlap...	104
4.3.5 Collimators.....	106
5. COMPARISON OF PERFORMANCE OF STATE OF THE ART CT AND LIMITED SCAN FLAW DETECTION.....	111
5.1 Computational complexity.....	111
5.2 Data Acquisition Time.....	112
5.3 Error Rates.....	113

REFERENCES

BIBLIOGRAPHY

APPENDICES

LIST OF SYMBOLS AND ABBREVIATIONS

Notation

α	proportional to, attenuation coefficient
\sim	distributed as
\approx	approximately equal
$E[\cdot]$	expected value of \cdot
$\text{var}[\cdot]$	variance of \cdot
$\text{cov}[\cdot]$	covariance, especially for vectors
μ	$E[\cdot]$, mean
σ	standard deviation= $\text{var}^{\frac{1}{2}}$, or scatter
kV	kilo volts
MV	mega volts
$[\text{\AA}]$	Angstrom, 10^{-10} meters
e	electron charge
m_e	mass of electron
h	Planck's constant
c	speed of light
λ	wavelength
U	voltage
J	current
ρ	specific gravity
μ	specific attenuation coefficient
τ	specific absorption

1. INTRODUCTION

The use of composite materials in light weight high performance components has become increasingly more popular [Reference 31], especially for aircraft components. Some of the advantages they offer over conventional materials are their increased stiffness to weight ratio while resisting to extreme environmental conditions, such as high temperature and chemical corrosion. Common to such components is their complicated internal structure.

Examples of such components are carbon-carbon composites which form parts of rocket motors (fabricated from three dimensional woven preforms) and engine turbine blades with internal cooling passages. Among the various non-destructive evaluation (NDE) methods X-ray techniques are regarded as being very promising for detecting deep subsurface flaws.

The success and fine resolution of computer aided tomography (CT) scanners in medical diagnosis [References 16, 17, 19, 41] for the detection of tissue density abnormalities in complex anatomical structures prompted the interest in how this technique might be adapted to serve as a new NDE tool. However, many of the objectives and the structure of certain cost functions and the degree of variability of structures to be examined distinguish the NDE environment from the medical. Thus, an investigation and somewhat different analysis of the performance of Tomography when applied to the NDE environment is called for.

One of the first questions which arise in this new context concerns

the understanding of the relation between the complexity of a test object and the number of projections (scans) necessary for detecting abnormalities. Intuitively there appears to be a relationship. Consider first the problem of detecting a void in a homogenous cube by taking a face-on X-ray projection. Apparently a single projection would suffice to detect the presence of that void, although some uncertainty would remain regarding its precise three dimensional location.

Alternatively consider the human head with its variable geometry and the many different materials with variable X-ray density of which it is made up. Here the detection of a slight abnormality-even with perfect measurements - would not be possible with a single projection. This is recognized in CT-scanners which use of the order of 100 projections for image reconstruction.

Some of the materials of interest for NDE appear to have an intermediate level of structural complexity, when compared with above examples. Consider for example the rocket nozzle shown in Figure 1.1. A counterpart in terms of complexity, in the medical environment, is apparently the human breast with its glandular structure. It is interesting to note that for mammography two projections of the compressed breast provide often adequate diagnostic information and seem to be preferred over tomographic methods. These observations suggest to investigate the possibility to examine also composite materials with an intermediate level of scans (projections), say two or three [Figure 1.2].

In NDE of composite materials, where often a large number of similar parts are inspected, further aspects enter consideration of limited scan

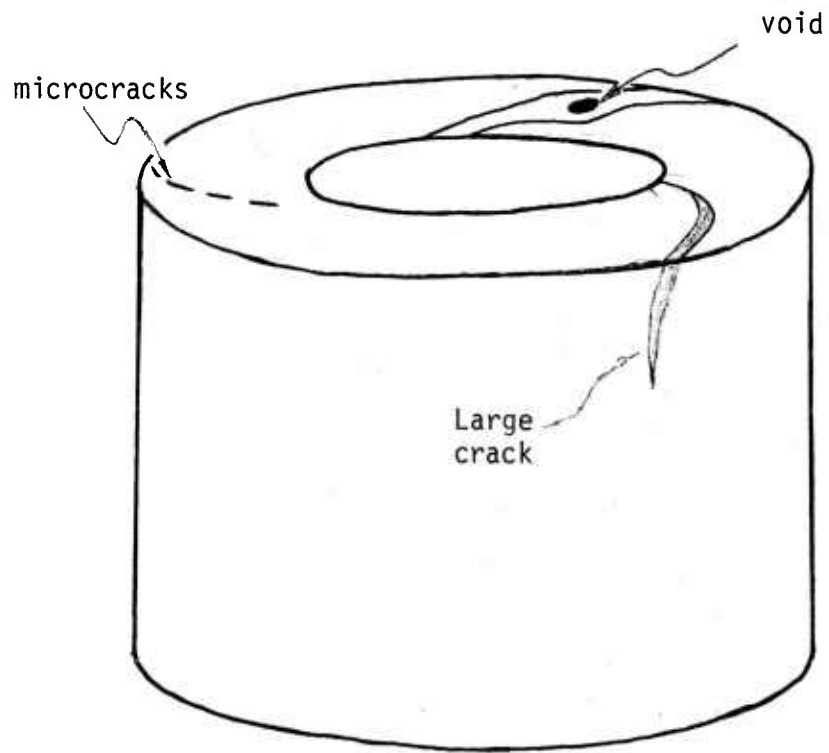


Figure 1.1: Schematic of a Cylinder manufactured from layers of woven carbon fibers. In this example the layers follow an Archimedes spiral. Interfaces are particularly susceptible to contain cracks.

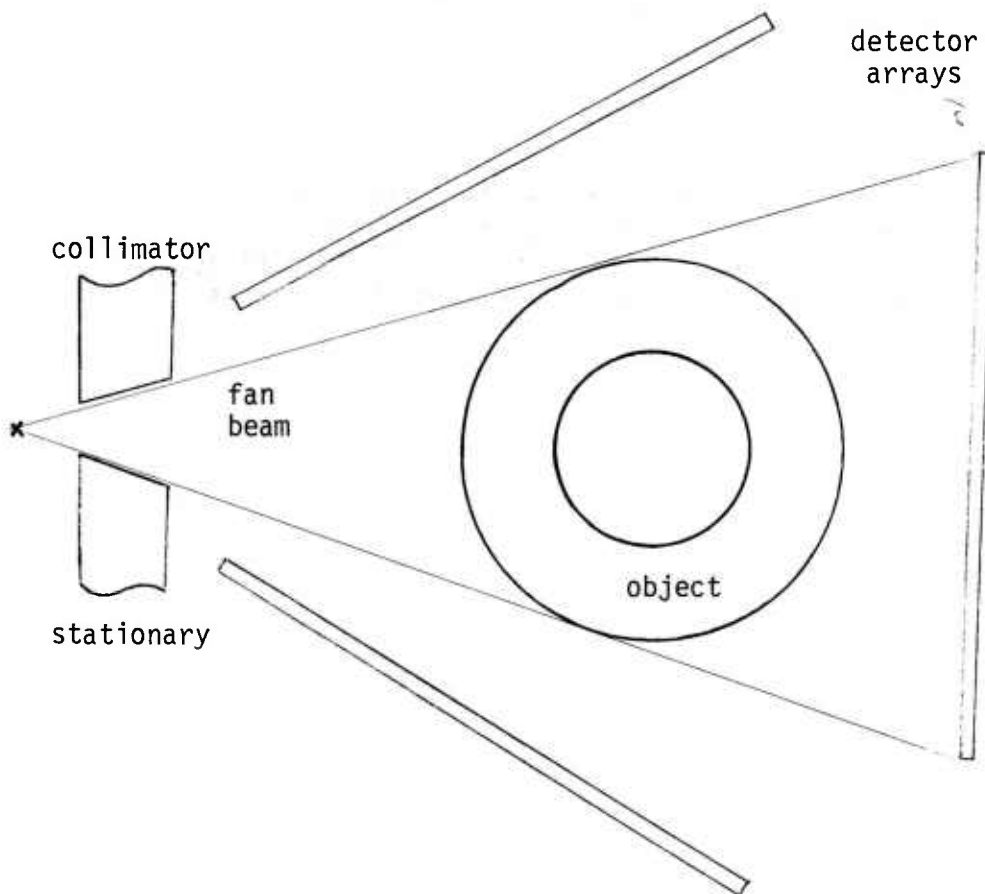
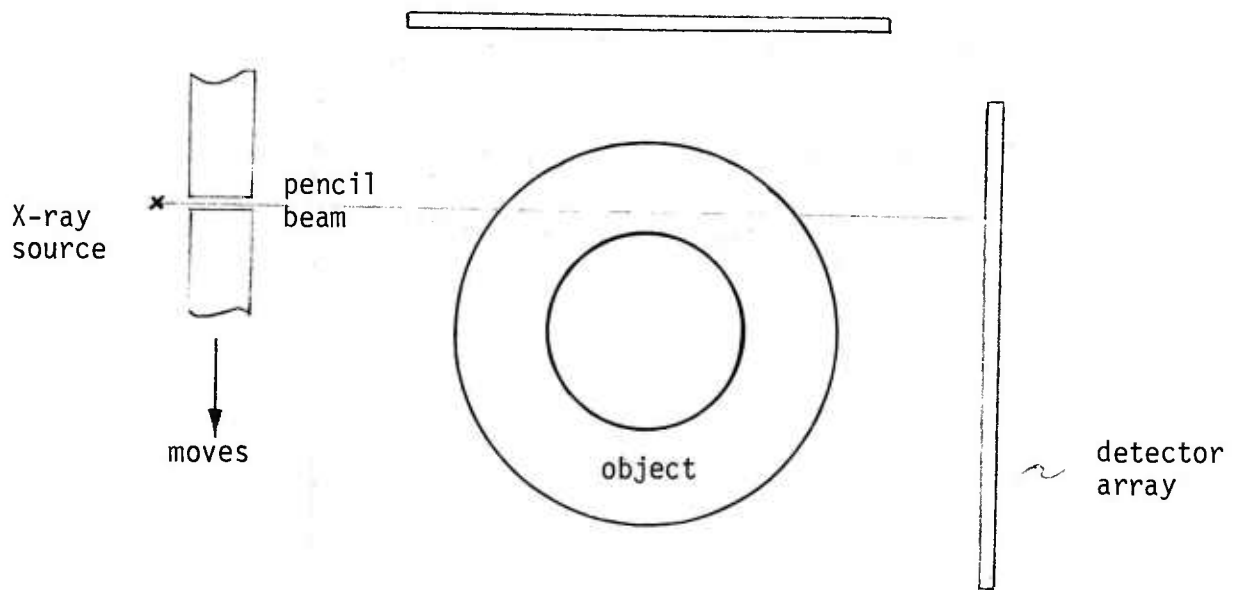


Figure 1.2: Examples of 2-scan pencil beam and 3-scan fan beam arrangement. For clarity only one X-ray source is indicated in each example.

tomography. For example it appears that relatively precise prior information about a test object is available and should be used. Another aspect is the desire to reduce scanning time for high speed NDE. The questions are: how can this be accomplished and what are the limitations of possible techniques or should this technique be combined with other techniques such as full CT scanning of suspicious parts. In order to respond to such questions a systematic approach is necessary. For the particular problem of flaw detection by radiographic techniques modern estimation theory provides this systematic approach.

The first requirement in the analysis through estimation theory is the development of models of phenomena which are capable of mathematical analysis. Typically, we start out with very simple models which show some select major properties of a problem. Then progressively other phenomena are incorporated into the simpler models and their performance degrading or improving properties are studied.

Following this concept we start out (Section 2.1) with some basic considerations about projections and solutions to the full-scan CT. Next we introduce basic considerations and a description of what could be regarded as limited scan CT for discrete image elements; this is followed by the introduction of a probabilistic generalization. At this point in Section 3 it becomes important to study in more detail the basic physical phenomena of X-ray generation, absorption, scatter and detection before moving on to an analysis of the impact of these on estimation (Section 4). As we go along we develop the necessary models based on the basic physical phenomena and give approaches to optimal or suboptimal estimation. Finally in section 5 we give a comparison of the performance of the full scan with the limited scan technique.

2. BASIC CONSIDERATIONS ABOUT PROJECTIONS

2.1 Use of Projections in Image Reconstruction

The most basic way to study properties of X-ray images begins with the analysis of a highly idealized situation. As shown in Figure 2.1 the projection (line integral) at every point s for a given projection angle θ is described by the linear model [Reference 10]

$$P_{\theta} f(s) = \int_a^b f[s\underline{u}(\theta) + t\underline{n}(\theta)] dt \quad (2.1)$$

where

$$\begin{aligned} \underline{u}(\theta) &= (\cos \theta, \sin \theta)^T \\ \underline{n}(\theta) &= (-\sin \theta, \cos \theta)^T \end{aligned} \quad (2.2)$$

Roughly, this quantity $P_{\theta} f(s)$ is measured in CT. In full scan CT the problem is to reconstruct $f[s\underline{u}(\theta) + t\underline{n}(\theta)] = f(x,y)$ from many projections P_{θ_i} . This problem has first been considered by Radon [Reference 34] and many methods for solving this problem approximately are available today [Reference [17]].

Since the projection as defined in (Equation 2.1) is a linear transform of $f[x,y]$ it is appealing to approach the inversion (reconstruction) by a linear transform. Using a linear reconstruction scheme has many advantages on an analytic level and from a numerical point of view. A method which has become particularly popular in medical CT-scanning is the filtered backprojection method which provides one such linear transform of measured projections.

The filtered backprojection method is specified in the following way [Reference 10]. Define the backprojection operator B_i for direction θ_i by

$$[B_i(\gamma)](\underline{x}) = \gamma(s_i) = \gamma(x_1 \cos \theta_i + x_2 \sin \theta_i). \quad (2.3)$$

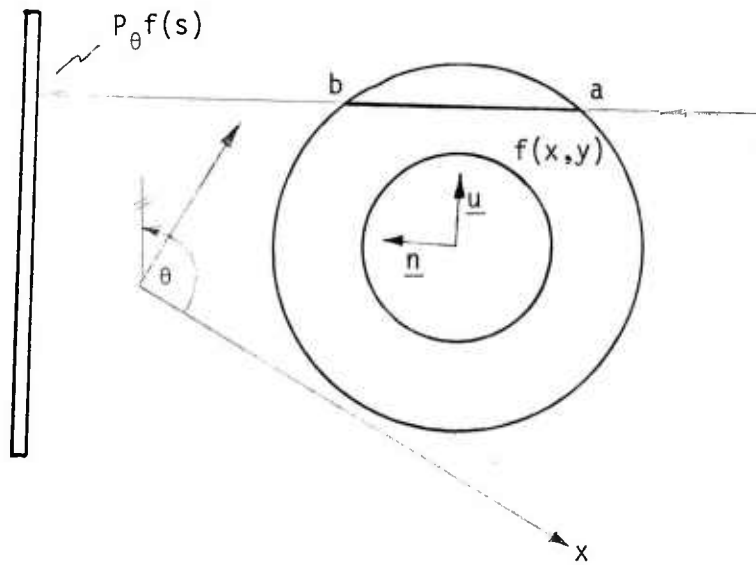


Figure 2.1: Projections $P_{\theta} f(s)$ as line integrals over a function $f(x, y)$

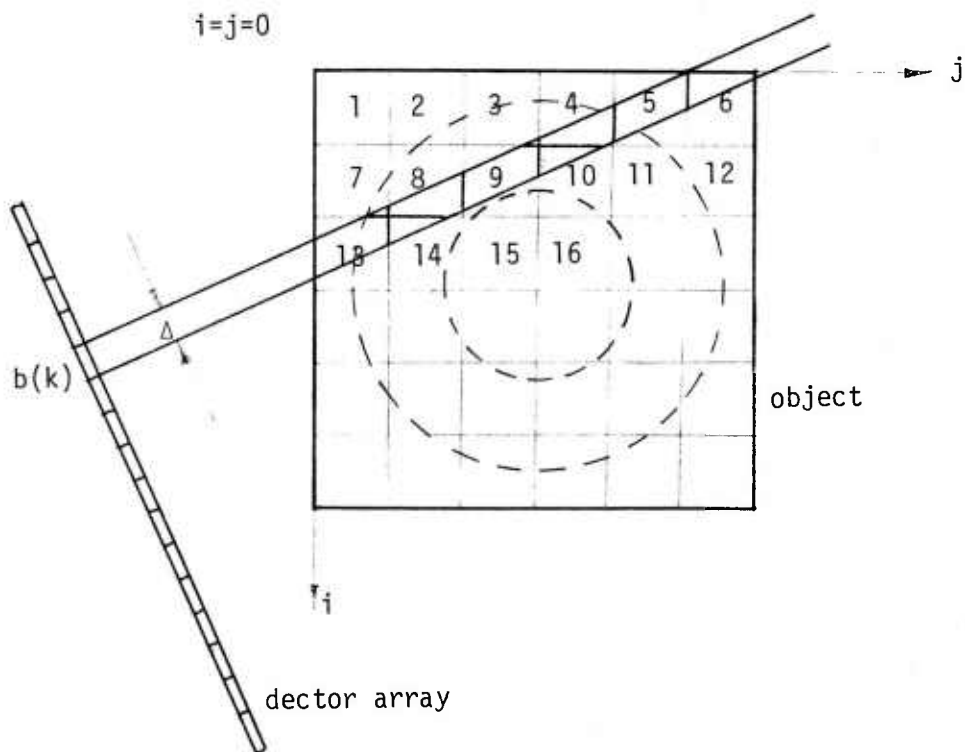


Figure 2.2: Relation of picture elements $a(\ell)$ to projection $b(k)$. From the area of intersection of the receptive field of detector k the elements of the matrix A may be computed. For the general relation shown analytic approaches are difficult.

Then, for projection i , filter the measurement with the (noncausal) filter $\alpha_i(s_i)$ to yield a smoothed projection $B_i(s_i) = P_{\theta_i} f(s_i) * \alpha_i(s_i)$ and finally average over all projections θ_i to obtain an approximation $f[\underline{x}]$ of the original $f[\underline{x}]$ as

$$\tilde{f}[\underline{x}] = \frac{1}{m} \sum_{i=1}^m [B_i(P_{\theta_i} f * \alpha_i)](\underline{x}) \quad (2.4)$$

which, as shown by Davison [10] equals also

$$\frac{1}{m} \sum_{i=1}^m (P_{\theta_i} f * \alpha_i)(\langle \underline{x}, \underline{u}(\theta_i) \rangle) \quad (2.5)$$

where \langle, \rangle indicates the inner product. In this case it is convenient to regard

$$F(\underline{x}) = \left[\frac{1}{m} \sum_{i=1}^m B_i \quad \alpha_i \right](\underline{x}) \quad (2.6)$$

as the point response function of the method - a point function located at $\underline{x}=0$ would precisely generate it. Note that the approximation in (2.4) is therefore equivalent to a 2-dimensional convolution (smoothing) of the original $f(x)$ by means of the point response function $F(\underline{x})$. Typically the filters α_i are smoothing the projection data leading to an image which is a smoothed version of the original.

As we mentioned before, the filtered back projection method is one particular method for finding a linear transform of measurements. The method could easily be generalized by assuming α_i to be nonstationary, in s or by assuming a more general linear transform than the filtered back-projection, $B_i \alpha_i$, say, by a general 2 dimensional weight function. In section 4 we will discuss some indication in which way one may wish, to modify the filtered backprojection method. One of the conveniences of the filtered backprojection method, its numerical simplicity, would be lost when more general weight functions are used. For example, convolution as need in the

filtered backprojection, can be executed very fast in the Fourier domain.

An interesting aspect of the choice of different filters is the following uncertainty principle. Consider the reconstruction of a function $f(\underline{x})$ by use of a desired point response function $Q_1(\underline{x})$ which is normalized by $\int_D Q_1(\underline{x}) d\underline{x} = 1$. Next assume the point response function to be scaled by $Q_t(\underline{x}) = t^2 Q(t\underline{x})$, $t \geq 1$, which increases spatial resolution while preserving the normalization. Then, while minimizing the error between Q_t and its approximation $1/m \sum B_i(\alpha_{ti})$ for all filters α_{ti} , that is minimizing for all $t \geq 1$ with respect to (α_{ti}) the quantity

$$\int_D [Q_t - \frac{1}{m} \sum B_i(\alpha_{ti})]^2 \quad (2.7)$$

implies [10]

$$(\frac{1}{t}) \int_D [Q_t - \frac{1}{m} \sum B_i(\alpha_{ti})]^2 \geq \int_D [Q_1 - \frac{1}{m} \sum B_i(\alpha_{1i})]^2 \quad (2.8)$$

Roughly, this implies the product of spatial resolution and contrast resolution (error) are bounded (from below) for increasing spatial resolution. This result has a similar character as one arising in a stochastic environment (Section 2.3).

After this basic introduction into some of the aspects of filtered back projection we will turn to the limited scan problem. This will give the opportunity to introduce aspects unique to discrete representation of picture elements.

2.2. The limited scan approach - deterministic aspects

Similar to the one before we will consider the arrangement shown in Figure 2.2. However instead of using continuous functions f we consider picture elements (pixels) over which the function is constant

$$\begin{aligned}
f(x,y) &= p(i,j); \text{ if } id \leq x < (i+1)d \\
&\quad jd \leq y < (j+1)d \\
&0 \quad ; \text{ otherwise}
\end{aligned} \tag{2.9}$$

Also, we replace the line integrals defining projection P in equation (2.1), be integrals over narrow stripes of width Δ and area Δ and evaluate

$$\tilde{P} f(s) = \int_A \int f(s \underline{u}_\theta + t \underline{n}_\theta) d\tau dt \tag{2.10}$$

We may select only discrete values of s in the direction of \underline{u}_θ which is expressed by

$$s = k \cdot \Delta \tag{2.11}$$

In this case we can stack all $p(i,j)$ into a vector \underline{a} by setting $a(\ell) = p(i,j)$, $\ell = n(i-1) + j$ as shown in Figure 2.2, $1 \leq i, j \leq n$.

Similarly stack all $\tilde{P}_\theta f(k\Delta)$ for all directions of θ into a vector \underline{b} and express the linear relationship between \underline{a} , the pixels and \underline{b} , the measurements by

$$\underline{b} = A \underline{a} \tag{2.12}$$

Here, the reconstruction problem is to find \underline{a} given \underline{b} . Clearly for arbitrary A a solution need not exist (inconsistency), there may be a unique solution - or infinitely many.

A general solution to (2.12) is given by [35].

$$\underline{a} = A^- \underline{b} + (H-I) \underline{z} \tag{2.13}$$

where A^- is any generalized matrix inverse (g-inverse) of the $M \times N$ matrix A , satisfying $A A^- A = A$, $H = A^- A$, and \underline{z} is arbitrary. The solution is complete if A^- has maximum rank regardless of rank $[A]$, that is rank $[A^-] = \min(M, N)$. Note that rank $[A]$ need not be maximal e.g. rank $A \leq \min[M, N]$.

Since we assume Equation (2.12) to be constructed from Equation (2.10) consistency of solution will at the moment not concern us (here it may be used to check numerical accuracy). What does concern us is the possible uniqueness of solutions in Equation (2.13). Clearly, if $H-I \underline{a}$ is unique, and required $\text{rank}[A] = \text{rank}[H] = N$. These relations suggest the following terminology: the full scan provides us with $\text{rank}[A]=N$, while the limited scan technique is one which provides us with $\text{rank}[A]<N$.

We will pursue now limited scan techniques somewhat further. For a general matrix A it may not be easy to find its rank numerically. However it is useful to look at certain special cases for which the rank can be determined analytically. For this purpose consider the arrangement of projections shown in Figure 2.3. For squares with unit area the matrix A in Equation (2.12) becomes

$$A = \left[\begin{array}{cccccccccccc} \overbrace{1 & 1 & 1 & 1}^{n\text{-times}} & & & & & & & & \\ & & & & 1 & 1 & 1 & 1 & & & & \\ & & & & & & & & 1 & 1 & 1 & 1 \\ & & & & & & & & & & 1 & 1 & 1 & 1 \\ 1 & & & 1 & & & 1 & & & 1 & & & 1 & \\ & 1 & & & 1 & & & 1 & & & 1 & & & \\ & & 1 & & & 1 & & & 1 & & & 1 & & \\ & & & 1 & & & 1 & & & 1 & & & 1 & \end{array} \right] \left. \begin{array}{l} \text{N-times} \\ \text{N-times} \end{array} \right\} \quad (2.14)$$

For this matrix we have $M=2n$, $N=n^2$ and, as can be shown easily by elementary row operation, $\text{rank}[A]=M-1$. (We remark - if the width of stripes for projection in Equation 2.11 is made smaller $\text{rank}[A]=2n-1$ regardless of M).

An interesting question concerns now the part $(H-I)\underline{z}$ in Equation (2.13) since this part is independent of measurements \underline{b} . In particular we are interested in understanding the pattern of values of pixels $p(i,j)$ which correspond to this part. This problem may be approached in the following

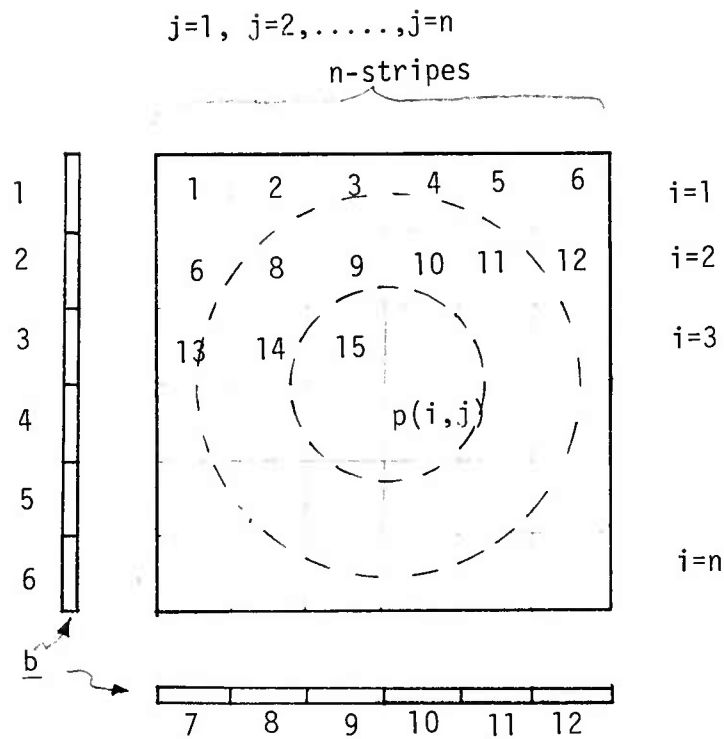


Figure 2.3: Relation of picture elements (pixels) $p(i,j)=a(\ell)$ to projections $b(k)$ for 2-scan technique.

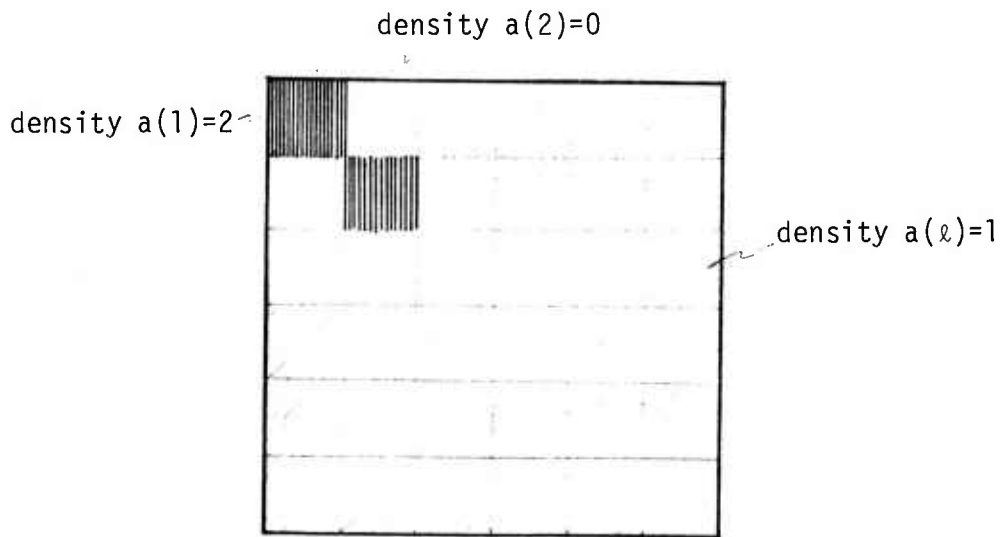


Figure 2.4: A basic pattern which is not observable by the 2-scan technique of Figure 2.3. This pattern can be moved into $(n-1)^2$ position and forms a complete basis for all unobservable patterns (assumption of shift in only multiples of the smallest unit).

way: we look for a set of k linearly independent patterns with $k = \text{rank } [H-I]$. These (non-unique) patterns correspond to a basis in the non-observable part of the space of \underline{a} and may be regarded as basic non-observable patterns. One solution for a set of basis vectors is one corresponding to the patterns shown in Figure 2.4. There are clearly $(n-1)^2$ such patterns, each of which is linearly independent of all others. In order to show that this set is also complete (e.g., spans all of $(H-I)z$) find $\text{rank } [H-I]$. Now since $(I-H)^2 = (I-H)$, that is, $(I-H)$ is idempotent, and $\text{rank } [H] \leq \text{rank } [I]$,

$$\text{rank } [I-H] = \text{trace}[I-H] = \text{trace}[I] - \text{trace}[H] \quad (2.15)$$

Furthermore

$$\begin{aligned} \text{rank } [H] &= \text{rank}[A^T A] = \min(\text{rank}[A^T], \text{rank } [A]) \\ &= \text{rank } [A] \end{aligned} \quad (2.16)$$

since $\text{rank } [A^T] \geq \text{rank } [A]$ (35). So we have $\text{rank } [H] = M-1 = 2n-1$. Thus with $\text{trace } [I] = n^2$ we obtain from Equation (2.15)

$$\text{rank}[I-H] = n^2 - (2n-1) = (n-1)^2 \quad (2.17)$$

Hence the $(n-1)^2$ pattern as shown in Figure 2.4. form a complete basis of the unobservable space. In other words, all other unobservable patterns can be formed by linear combinations of these basic patterns. Some examples are shown in Figure 2.5.

The consequence of this above result is, one should avoid positioning of objects, which are to be examined, in such a way that critical components form these basic patterns. Actually, one should avoid all positions which form any linear combinations of these basic patterns. For simple objects with only few critical places this may easily be judged. In the more general case, when there are many critical locations one should write down

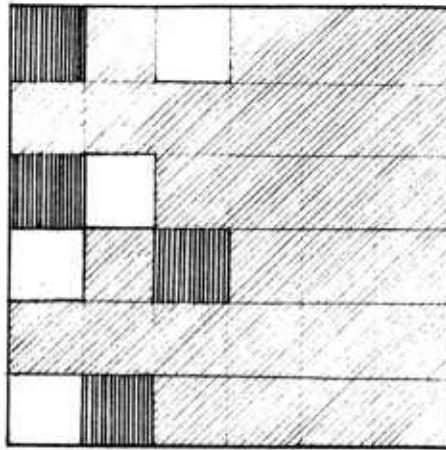


Figure 2.5: An example of an unobservable pattern generated by the linear combination of basic unobservable patterns (2-scan technique), of Figure 2.4.

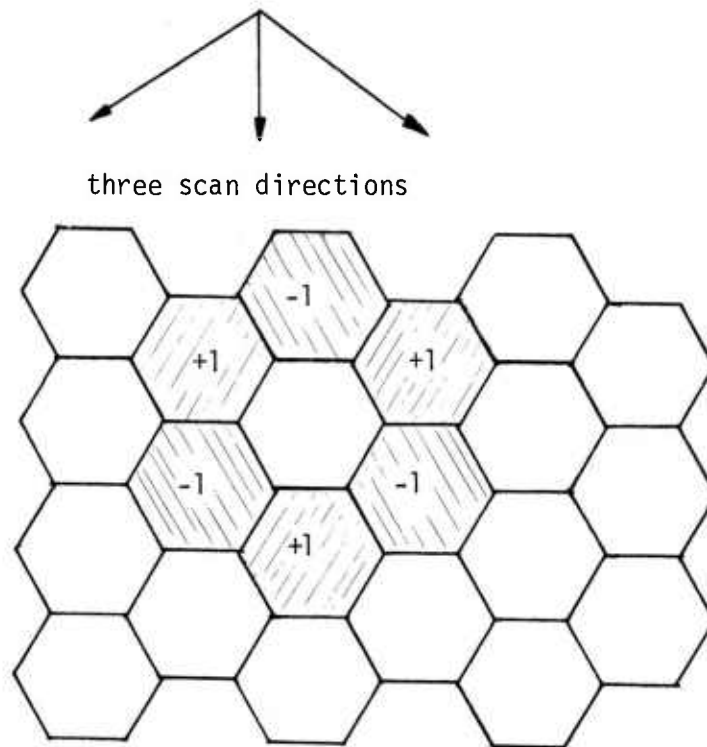


Figure 2.6: A basic unobservable pattern for the three scan directions shown.

the projection matrix L of just these k locations and examine whether the rank of this projection matrix is equal to ℓ . If so there is no problem in detecting abnormalities. If, however, $\text{rank}[L] < \ell$ it is either necessary to position an object differently or to take additional measurements until $\text{rank}[L] = \ell$.

All the considerations discussed here carry easily over to the three scan technique. In order to obtain a simple matrix A here it may be more useful to consider six cornered pixels giving an arrangement like in honey combs. For such an arrangement the corresponding matrix A is easily written down for a given range of pixels and allows again analytic evaluation of its rank. From analogy considerations to the two-scan technique a set of basic unobservable patterns will have the shape shown in Figure 2.6.

For the fan beam 2-scan technique the choice of a convenient shape of pixels is somewhat more difficult. But consider that this arrangement corresponds to a collinear transformation of the parallel beam configuration as shown in Figure 2.7 and may thus be analyzed similar to the parallel beam problem. In some situations it may be useful to combine pixels especially near the X-ray source if it is desired to maintain approximately constant pixel area. The same approach of a collinear transformation can be taken for the 3-scan technique (Figure 2.8). All of above results will thus not change since (except for the focal point) they are in a 1-1 correspondance to the parallel beam configuration.

In summary, the complete solution to the inverse problem $\underline{b} = A\underline{x}$ is given by Equation (2.13). It is clear that for an increasing number of pixels the solution space \underline{x} grows very fast regardless of the spatial resolution of the detectors (Equation 2.17). Thus, in order to say

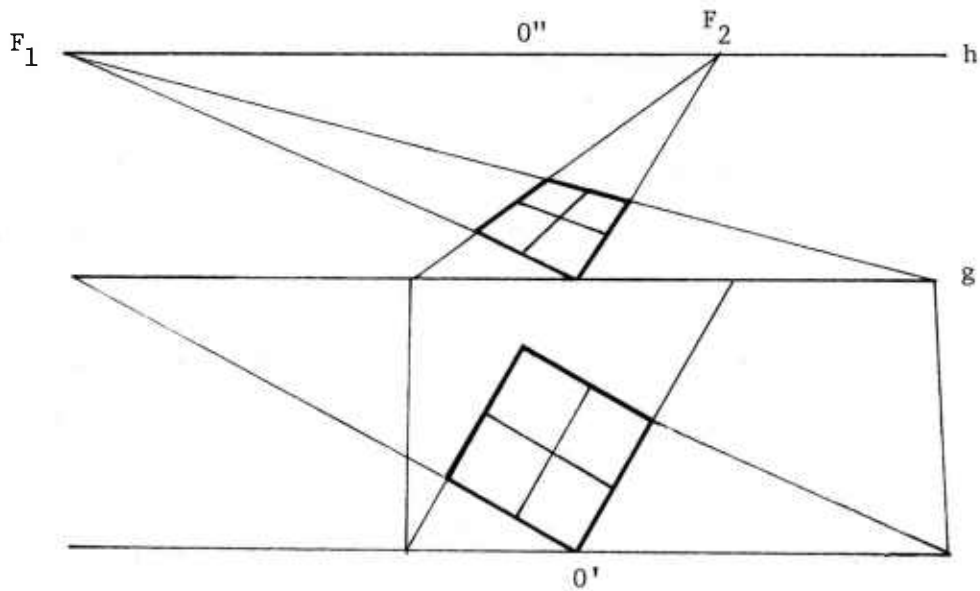


Figure 2.7: Collinear transformation, as in perspective, can be used to transform the 2-scan parallel beam projections into a fan beam geometry with X-ray sources at F_1 and F_2 .

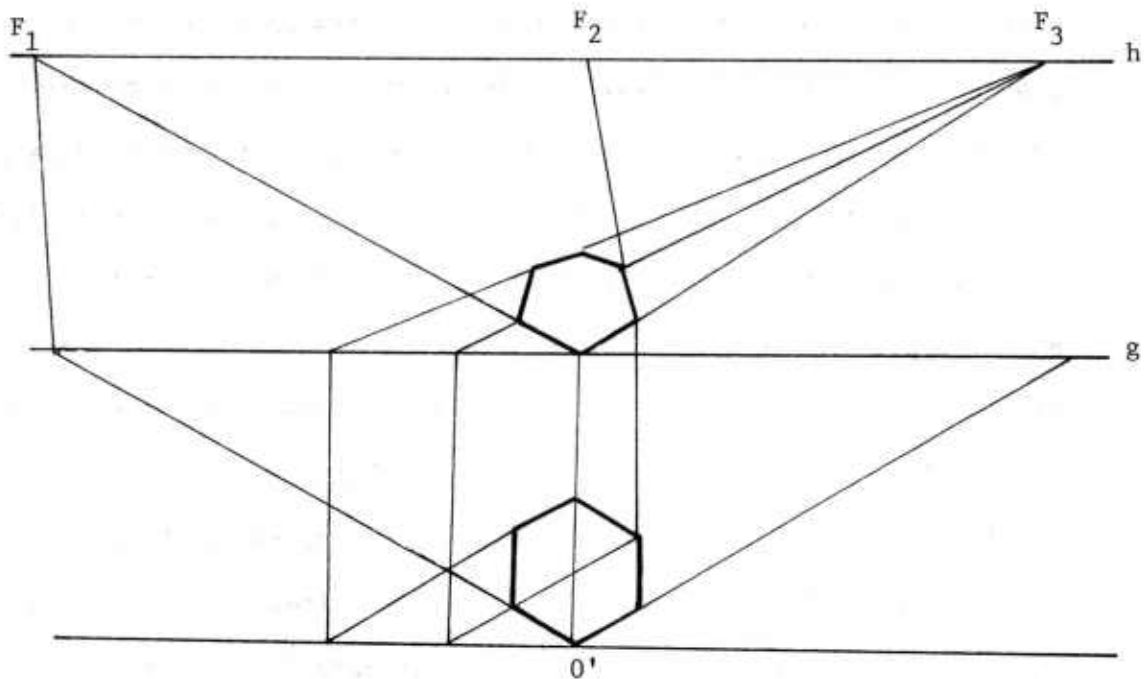


Figure 2.8: Provided that all three X-ray sources F_1 , F_2 , F_3 lie on a straight line a collinear transformation of the parallel beam geometry permits to use a transformed honeycomb pattern for picture elements while maintaining the projection matrix A simple.

more about \underline{x} given \underline{b} more constraints have to be placed on \underline{x} . Beside the introduction of additional scans in new directions, this space can be constrained in a probabilistic way and is subject of the following section.

2.3 Probabilistic approaches

This section starts out with an exposition of the problem in a Bayesian framework. Then, a simple model for quantum mottle in measurement is introduced and approximations for dealing with the nonlinear relationship between image and measurements are developed. Next, two limiting situations and their value for the limited scan problem is assessed.

One limiting situation assumes large measurement noise - the other perfect measurements. In this latter case the stochastic nature of the problem is maintained by assuming an object of constant average density, but with random variations of this density. It is shown, for the two-scan technique, that an optimal detection scheme is computationally not feasible and that one version of a suboptimal scheme which uses the correlation structure of measurements discriminates quite well against flaws.

Another suboptimal approach, neglecting the correlation structure of measurements, is shown to perform similarly well. In this approximation, the distribution function of certain random variables remains unchanged except for the mean, when alternative hypotheses are made (presence vs. absence of a flaw). With this suboptimal approach a sequential probability ratio test is ultimately developed and an example of its performance is given. The main conclusion is that for most materials with random density variations in the percent range, a rather large number of scans has to be performed in order to decide about the presence of flaws. For the example given, (with rather large quantum mottle) this number comes closest to the number used for full scan tomography. However, the average cost due to using this procedure is shown to be small, almost independent of

the loss which would arise with failure of the component due to presence of a flaw, simply because the probability of errors is extremely small.

Let us turn now to the exposition of the new framework. Probabilistic considerations enter the limited scan and the full scan techniques in several ways. Two important aspects are the well known quantum mottle and the, possibly not so obvious, random material density variations. The latter may result from variations in chemical composition, microporosity or, on a still larger scale, from variations of location of fibers such as in woven performs.

As before we consider the evaluation of (the absorption due to) pixels $p(i,j)$ represented by a vector \underline{a} given some measurements \underline{b} . This time however we have a probabilistic description of the absorption of the pixels and a probabilistic description of \underline{b} even when \underline{a} is fixed; this latter description accounts for uncertainty due to quantum mottle. More formally we assume to know the distributions $p(\underline{a})$ and $p(\underline{b}|\underline{a})$ and wish to obtain the distribution $p(\underline{a}|\underline{b})$. This problem is solved formally by Bayes rule

$$p(\underline{a}|\underline{b}) = \frac{p(\underline{b}|\underline{a}) \cdot p(\underline{a})}{\int_A p(\underline{b}|\underline{a}') p(\underline{a}') d\underline{a}'} \quad (2.18)$$

In practice, solving equt. (2.18) can be difficult or even impossible. This is due to the necessary integration in the denominator of Equation (2.18). For our purposes of image analysis this integration has to be performed over a $10^4 \dots 10^6$ dimensional space when images with 100x100 or 1000x1000 pixels resolution are desired.

Several approaches exist to dealing with this problem. Mainly, they are based on approximations. First, one may try to replace the general distribution with certain types of analytic approximations which then allow

analytic integration. Second, especially when the prior distribution is "flat" such as when \underline{a} is highly uncertain, $p(\underline{b}|\underline{a})$ can approximate the shape of $p(\underline{a}|\underline{b})$ (the denominator, when the measurements \underline{b} are given represents merely a scaling). We note that maximizing $p(\underline{b}|\underline{a})$ leads to the so-called maximum likelihood (ML) - estimator which has often many desirable properties.

The approach based on analytic approximations uses distributions for which the posterior $p(\underline{a}|\underline{b})$ belongs to the same simple family of distributions as the prior $p(\underline{a})$. However the distribution pair $p(\underline{b}|\underline{a})$ and $p(\underline{a})$ need not belong to the same family of distributions and are called conjugate. Typically, these conjugate pairs are used for sampling schemes for which \underline{b} is a linear function of \underline{a} . If this condition of linearity is not met (as in X-ray imaging) further approximations are necessary to estimate \underline{a} .

At this point an important aspect of estimation should be clarified. Estimation is closely linked to cost structures in a problem. For example, an estimate of a quantity is a good (bad) estimate if the expected cost associated with it is small (large). For many reasons the quadratic loss functions in the error of an estimate arises naturally, and is used in analysis of many problems. Thus for an estimate $\hat{\underline{x}}$ of a quantity \underline{x} we associate often the loss

$$L(\hat{\underline{x}}) = (\underline{x} - \hat{\underline{x}})^T M (\underline{x} - \hat{\underline{x}}) \geq 0 \quad (2.19)$$

and the risk (the average or expected loss over all estimates $\hat{\underline{x}}$)

$$E[L(\hat{\underline{x}})] \geq 0 \quad (2.20)$$

where M is some positive (semi) definite matrix. The matrix M will typically reflect the particular cost structure in the neighborhood of the

true value \underline{x} . The objective in estimation can now be viewed as the problem of finding the minimum of $E[L(\hat{X})]$.

After these preliminary remarks on finding probability density functions and good estimates we may turn to the particular problem of CT-scanning. First we wish to find an approximation to the nonlinear relation of material density to photon count. A frequently used approximate model assumes exponentially declining photon flux. Thus for a source releasing I_0 photons a detector sees on the average

$$\mu_I = E[I] = I_0 \exp \left\{ - \int_A f(t,s) dt ds \right\} \quad (2.21)$$

The distribution of the photon count is well described by a Poisson density

$$p(I) = e^{-\mu_I} \sum_{k=0}^{\infty} (\mu_I)^k \delta(I-k) \quad (2.22)$$

When the photon count is large one can make use of a Gaussian approximation F of the cumulative Poisson distribution P , e.g.

$$P(I < C) = F(I < C) + \epsilon \quad (2.23)$$

where ϵ is often negligible. For $E[I]$ of more than a few hundred, which will be a typical situation in X-ray imaging, this approximation is very useful. Once we characterize the photon count by a Gaussian distribution we need only to specify its mean and variance to specify the entire distribution. For this case one has

$$\begin{aligned} \mu_I &= E[I] \\ \sigma_I^2 &= E[(I - \mu_I)^2] = \mu_I \end{aligned} \quad (2.24)$$

Consider now the problem of estimating $G = \int_A f(t,s)$. It is well known

that the ML-estimator of G formed by

$$\hat{G}_b = -\ln I/I_0 \quad (2.25)$$

leads to biased estimators e.g. $E[\hat{G}_b - G] = g \neq 0$ [Reference 36]. This implies that a risk of the type (Equation 2.20) is not minimized by \hat{G}_b . However it is easily shown that correcting for this bias by using

$$\hat{G} = \hat{G}_b - g \quad (2.26)$$

does minimize Equation (2.20). Rockmore [Reference 36] gives for g (for the Poisson-case)

$$g = \frac{1}{2\mu_I} + \frac{1}{12\mu_I^2} + \frac{3}{4\mu_I^3} + \dots \quad \dagger \quad (2.27)$$

For us the problem exists that, due to the material uncertainties, we do not know μ_I a priori. So, again we have to use an estimator-possibly one a posteriori. It appears that for the situation in limited scan CT for NDE the bias could easily be made small relative to other effects such as the uncertainty expressed by the standard deviation of \hat{G} .

The variance of \hat{G} is given by [36] as

† It should be made clear, however, that this series expansion requires for its convergence a pseudo-Poisson variate of I : namely it is required that $P[I=0] \approx 0$. Since $P[I=0] = e^{-\mu_I}$ for a Poisson variate this quantity is indeed extremely small for $\mu_I > 100$. The requirement $P[I=0] \approx 0$ can be satisfied by rejecting any measurement with $I=0$. In fact we can even afford to reject all $I < \mu_I/2$ provided $\mu_I > 100$. For example for $\mu_I = 100$ $P[I < 50] < 10^{-6}$. So in all series expansion in which we may need an estimate of μ_I and replace it by I , convergence occurs rapidly with large probability. It appears that with much larger probability other effects would result in degradation of performance of any practical estimation scheme than are due to above approximations. Subsequent expansions are all based on this approximation.

$$v = \frac{1}{\mu_I} + \frac{3}{\mu_I^2} + \frac{43}{12\mu_I^3} + \dots \quad (2.28)$$

Thus even for "small" photon counts in the order of a few hundred the ratio of g/\sqrt{v} is only a few percent. Nevertheless it is easy to correct - at least to first order - the bias by using the revised estimator (for I large, say $I > 100$)

$$\hat{G}' = -\ln(I/I_0) + \frac{1}{2\mu_I} \quad (2.29)$$

From some rough calculation (using a simple linearization technique and a 4σ threshold) one can evaluate performance for this estimator: with only .01 percent probability does the residual bias exceed a fraction $f = 4/\sqrt{I}$ of the uncorrected bias. This suggests that the ratio of residual bias to standard deviation exceeds $2/I$ in less than .01 percent of all cases. One may argue further that of the order of I independent measurements are necessary to detect with 95% probability such small bias. Of course, if desired a still more sophisticated approach may be used to correct bias but other uncertainties associated with the polychromaticity of X-rays will become important suggesting a more rigorous modeling of nonlinearities (Section 4.2).

Let us return now to the general problem of estimating $p(\underline{a}|\underline{b})$. As we have shown, the relation between \underline{a} and \underline{b} are nonlinear - but we discussed how, and under what conditions (e.g. $I > 100$) linearization of that problem becomes useful. We may thus consider the linearized estimation problem (linearized around the measured \underline{b}). For the linearized problem the probabilistic relation between \underline{a} and \underline{b} are (in contrast to Equation 2.12) described by

$$p(\underline{a}) \sim N(\underline{\mu}_a, \Sigma_a) \quad (2.30)$$

and

$$p(\underline{b}|\underline{a}) = N(\underline{\mu}_b(\underline{a}), \Sigma_{b|a}(\underline{a})). \quad (2.31)$$

As can easily be shown, due to linearization the second order moment in terms of $\Sigma_{b|a}(\underline{a})$ is approximated by $\Sigma_{b|a}(\mu_a)$. (If such an approximation is insufficient certain iterative procedures described by [Reference 21] can be used).

We are now in the position to solve approximately Bayes theorem Equation (2.18); $p(\underline{b}|\underline{a})$ and $p(\underline{a})$ are conjugate distributions which are fully described by their first and second moments $\underline{\mu}$ and Σ respectively. In this case the posterior mean $\underline{\mu}_{a|b}$ and covariance matrix $\Sigma_{a|b}$ are found by the Kalman Filter algorithm [References 21, 37].

$$\underline{\mu}_{a|b} = \underline{\mu}_a + W[\underline{b} - A^* \underline{\mu}_a], \quad (2.32)$$

$$W = \Sigma_a A^{*T} [A^* \Sigma_a A^{*T} + \Sigma_b]^{-1}, \quad (2.33)$$

$$\Sigma_{a|b} = \Sigma_a - W A^* \Sigma_a. \quad (2.34)$$

Here however

$$A^* = \frac{\partial \underline{b}}{\partial \underline{a}} \quad (2.35)$$

and with Equation (2.29)

$$b_i = -\ln(I_i/I_0) + \frac{1}{2I_i} \quad (2.36)$$

It is easily shown (Appendix A2.1) that A^* is closely related to A in Equation (2.12) by

$$A^* = \begin{bmatrix} 1 + \frac{1}{2I_1} & & 0 \\ & 1 + \frac{1}{2I_2} & \\ 0 & & \ddots \end{bmatrix} A \quad (2.37)$$

being equivalent to a slight rescaling of the dependent variable b .

The covariance matrix $\Sigma_{b|a}$ is, due to the independence of quantum mottle between detectors, diagonal:

$$\Sigma_{b|a} = \begin{bmatrix} v_1 & & 0 \\ & v_2 & \\ 0 & & v_M \end{bmatrix} \quad (2.38)$$

where from Equation (2.23) we may use for the estimates of v_i the series

$$\hat{v}_i = \frac{1}{I_i} + \frac{3}{2I_i^2} + \frac{43}{12I_i^3} + \dots \quad (2.39)$$

which converges with large probability rapidly (for $\mu_i > 100$).

We are now in the position to answer some questions for the limited scan problem. First let us consider the problem of using transmission data which is relatively noisy due to quantum mottle rather than material density variations. More formally assume

$$x^T A^* \Sigma_a A^{*T} x \ll x^T \Sigma_{b|a} x \quad (2.40)$$

and let $\Sigma_a = \sigma_a^2 I$ and $\Sigma_{b|a} = \sigma_b^2 I$. For the purpose of the current analysis replace also A^* by A (Equation 2.37) as this simplifies notation and does not change any of the conclusions. In this case we can approximate Equations (2.32)-(2.34) by

$$\begin{aligned} \underline{\mu}_{a|b} &\approx (I - \sigma_a^2 \sigma_b^{-2} A^T A) \underline{\mu}_a + \underline{W} b \approx \underline{\mu}_a + \underline{W} b \\ \underline{W} &\approx \sigma_a^2 \sigma_b^{-2} A^T \\ \Sigma_{a|b} &\approx \sigma_a^2 (I - \sigma_a^2 \sigma_b^{-2} A^T A) \approx \sigma_a^2 I \end{aligned}$$

Roughly, what is seen in this algorithm is very similar to the unfiltered backprojection method - data in \underline{b} is evenly distributed in its effect over the corresponding strip i over which measurement i has been taken, weighted by the ratio of "signal" power (σ_a^2) to measurement noise power v_i .

Let us evaluate the useful range of above model. For our situation, assume materials with $\sigma_a = x\%$ density variation over, say 5mm x 5mm pixels and assume $n = 100$, corresponding to an X-ray path of 500mm. The standard deviation of a projected measurement is

$$\sigma_p = \sqrt{n} \sigma_a = 10x\% \quad 2.42$$

This quantity was assumed to be small compared to quantum mottle, e.g.,

$$\sigma_p \ll \sqrt{v} \quad 2.43$$

or by Equation (2.28)

$$\sigma_p \ll (\mu_I)^{-\frac{1}{2}} \quad 2.44$$

We assume usually $\mu_I > 100$ and thus require

$$\sqrt{n} \sigma_a \ll (\mu_I)^{-\frac{1}{2}} \quad 2.45$$

In this case, we obtain the requirement

$$\sigma_a \ll 1\%.$$

$$\text{or } x \ll 1. \quad 2.46$$

As an alternative way to investigate the estimation problem, we may check what happens if we perform very precise measurements, e.g., $I_i \rightarrow \infty$, $I_i/I_0 \rightarrow C_i$ in Equation (2.36) and look at the simple 2-scan problem. In this case, we encounter a difficulty with Equation (2.33). The matrix $A^* \Sigma_a A^{*T} + \Sigma_{b|a}$ becomes singular since rank $[A]$ as defined is not maximum and $\Sigma_{b|a} \rightarrow 0$. There are several ways to deal with this situation. A simple possibility is to eliminate those rows of A in equation (2.14) which are linearly dependent on all others; omitting for example the last row would generate a new matrix \tilde{A} with maximum rank. Thus we are again in a position to use, although with one less measurement (but without

loss of information) Equations 2.32-2.34. Now we obtain

$$\underline{\mu}_a|b = [I - \Sigma_a \tilde{A}^T [\tilde{A} \Sigma_a \tilde{A}^T]^{-1} \tilde{A}] \underline{\mu}_a + \Sigma_a \tilde{A}^T [\tilde{A} \Sigma_a \tilde{A}^T]^{-1} \tilde{A} b \quad 2.47$$

$$\Sigma_a|b = [I - \Sigma_a \tilde{A}^T [\tilde{A} \Sigma_a \tilde{A}^T]^{-1} \tilde{A}] \Sigma_a \quad (2.48)$$

Here we would again like to know how an estimate $\underline{\mu}_a$ is modified by perfect measurements b and to what extent the precision of this estimate is changed.

For this purpose consider the model of equal uncertainty throughout all pixels, and that no pixel depends on any other pixel (maximum entropy). This corresponds to

$$\Sigma_a = \sigma_a^2 I \quad (2.49)$$

To investigate this problem we computed the matrices \tilde{A} , $\tilde{A} \tilde{A}^T$, $(\tilde{A} \tilde{A}^T)^{-1}$, $\tilde{A}^T (\tilde{A} \tilde{A}^T)^{-1}$ and $\tilde{A}^T (\tilde{A} \tilde{A}^T)^{-1} \tilde{A}$ for $n = 1, 2, 3, 4$ (Tables 2.1. - 2.4). As expected these matrices exhibited some simple patterns for the distribution of their elements. Furthermore by checking the elements for $n=2$ and $n=3$ a simple relationship of their values to n was found and confirmed for $n=4$ and 5.

The matrices \tilde{A} and $\tilde{A} \tilde{A}^T$ are trivial and we refer simply to tables 2.1-2.4. Somewhat more interesting were the matrices $(\tilde{A} \tilde{A}^T)^{-1}$ (which we will use repeatedly), the update matrix $\tilde{A}^T (\tilde{A} \tilde{A}^T)^{-1}$ and the matrix $\tilde{A}^T (\tilde{A} \tilde{A}^T)^{-1} \tilde{A}$ which expresses improved precision in the description $\underline{\mu}_a|b$ of the material. We found that only a few distinct values could arise in the matrices and there is good reason to believe that these are all possible values for any n . The values relate to the following:

1. the relation of one pixel to itself
2. the relation of one pixel to the stripe in which it is contained;
3. the relation of one pixel to another pixel within the same stripe;
4. the relation of one pixel to one in another stripe;
5. and whether measurements relate to the side on which one strip of measurements has been removed (recall the last row of A has been omitted).

TABLE 2.1: Matrices A , AA^T , $(AA^T)^{-1}$, $A^T(AA^T)^{-1}$, $A^T(AA^T)^{-1}A$
for $n=1$; Note: $\det(AA^T)=1$

```

$ RUN TOMOMAT
DIMENSION OF N = ?
A1
  1.000
AA*=
  1.000

IDGT,D1,D2,IER =          50 1.000    0.000    0
(AA*)# =
  1.000
A*(AA*)# =
  1.000
A*(AA*)#A =
  1.000
$

```

TABLE 2.2: Matrices A , AA^T , $(AA^T)^{-1}$, $A^T(AA^T)^{-1}$, $A^T(AA^T)^{-1}A$
for $n=2$; Note: $\det(AA^T)=4$

```

$ RUN TOMOMAT
DIMENSION OF N = ?
A2
  1.000    1.000    0.000    0.000
  0.000    0.000    1.000    1.000
  1.000    0.000    1.000    0.000
AA*=
  2.000    0.000    1.000
  0.000    2.000    1.000
  1.000    1.000    2.000

IDGT,D1,D2,IER =          7 0.250    4.000    0
(AA*)# =
  0.750    0.250   -0.500
  0.250    0.750   -0.500
 -0.500   -0.500    1.000
A*(AA*)# =
  0.250   -0.250    0.500
  0.750    0.250   -0.500
 -0.250    0.250    0.500
  0.250    0.750   -0.500
A*(AA*)#A =
  0.750    0.250    0.250   -0.250
  0.250    0.750   -0.250    0.250
  0.250   -0.250    0.750    0.250
 -0.250    0.250    0.250    0.750
$

```

TABLE 2.3: Matrices A , AA^T , $(AA^T)^{-1}$, $A^T(AA^T)^{-1}$, $A^T(AA^T)^{-1}A$ for $n=3$; Note: $\det(AA^T)=81$

[illegible]

For these various matrix elements t_i it has been found for $n \times n$ pixels (see table 2.1-2.4) which are, ordered by magnitude

example of location	
$t_0 = \left(\frac{2n-1}{n^2}\right)$	relation for a pixel to itself
$t_1 = t_0 \left(\frac{1n}{2n-1}\right)$ for pixels within a stripe for side with all stripes measured
$t_2 = t_1 \left(\frac{n-1}{n}\right)$ within stripe for side with omitted stripe
$t_3 = t_2 \left(\frac{1}{n}\right)$ between pixels not sharing a stripe
$t_4 = 0$ for update from side with omitted stripe
$ M = AA^T = n^{2(n-1)}$	determinant (2.50)

What is important here is the asymptotic behavior as $n \rightarrow \infty$. It is seen that, as one might suspect also from other considerations, the behavior of these terms, is

$$\begin{aligned}
 t_0 &\approx 2/n \\
 t_1 &\approx 1/n \\
 t_2 &\approx 1/n \\
 t_3 &\approx 2/n^2
 \end{aligned}
 \tag{2.51}$$

Checking some more the behavior of $\tilde{A}^T(\tilde{A} \tilde{A}^T)^{-1}$ suggest again a performance of updating the pixels (except for the ones in the stripe corresponding to the missing row in A) very similar to the filtered back projection (Figure 2.9). Note, that the mean of a_{ij} changes by

$$\Delta \mu_{a_{i,j}} = b_i t_2 + b_j t_1 \approx (b_i + b_j)/n
 \tag{2.52}$$

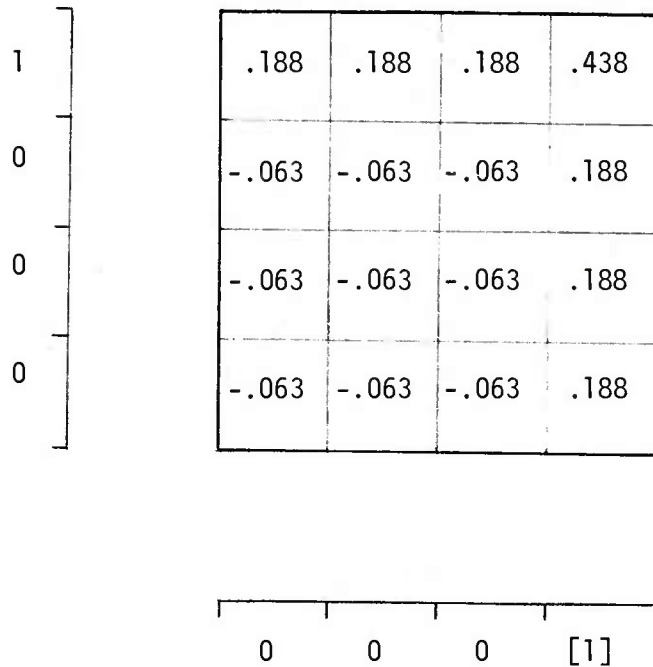


Figure 2.9: Example for updating when $\underline{b}^T = (1, 0, 0, 0, 0, 0, 0)$. The element [1] is not observed as it must be linearly dependent on all other values in \underline{b} . This example is obtained from $A^T(AA^T)^{-1}$ in Table 2.4.

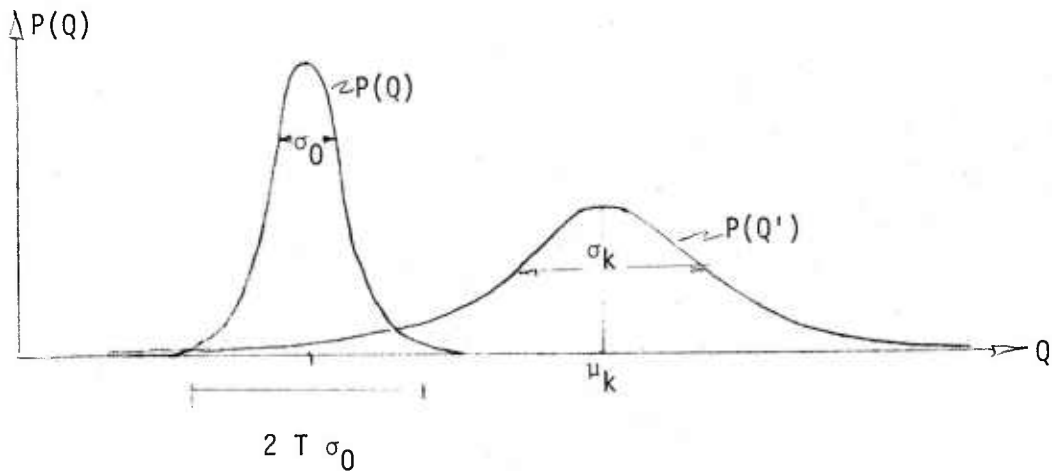


Figure 2.10: Distributions of the quadratic terms Q and Q' where $\underline{x}^T M \underline{x}$ is used. Q will typically arise in the problem formulation associated with H_0 and Q' with H_k . If however a flaw $\underline{\epsilon}$ at location k is known a complimentary quadratic form $(\underline{x}-\underline{\epsilon})^T M (\underline{x}-\underline{\epsilon})$ can be set up. For this form the roles of Q and Q' are reversed.

if both stripes i and j are measured. However it changes by

$$\Delta\mu_{a_{i,j}} = b_i \cdot t_0 \approx 2b_i/n \quad (2.53)$$

for the column j in the image which contains no measurement - as the corresponding observation in A has been omitted. Note that from Equation (2.50) $t_1 + t_2 = t_0$. With regard to the variance for pixel $a(i,j)$ observe it declines only by a factor of $(1-t_0)$ which does not seem to be of much significance. Note: $\Sigma_{a|b}$ is strongly diagonal although only of rank $(n-1)^2$.

In order to detect and locate a change in density it will be required to have a large change $\Delta\mu_{a_{ij}}$ relative to σ_a^2 . This is somewhat of a problem as will be shown because there is only weight $b_i t_2$ added to the strip containing all pixels $p(i,j)$ $i=1\dots n$ and weight $b_j t_3$ to the strip containing all pixels $p(i,j)$ $i = 1\dots n$ (aside from those corresponding to the missing row in A). Performance of a flaw detection and location scheme, based on this information, can now be approached by formulating a decision problem [Reference 11].

2.3.1 Decision theoretic approach

Let the parameter space Ω in the presence of a single flaw (in any pixel) consist of n^2 values w_i plus a value w_0 for absence of flaws. The loss table L for decisions $d_0 \dots d_{n^2}$ would possibly be

	d_0	d_1	d_2	d_{n^2}
w_0	0	e	e e	e
w_1	f	g	h h	h
w_2	f	h	g		\vdots
\vdots	\vdots	\vdots		\cdot	\vdots
\vdots	\vdots	\vdots		\cdot	\vdots
w_{n^2}	f	h.....	g		\vdots

(2.54)

With regard to the values expressed in the loss table, f will probably be the largest as the cost of missing a flaw may be deleterious.

The value of e would possibly be next since some more extensive testing would be necessary to correct the false alarm or to loose the good test object. Values g and h may be nearly the same, although h may be slightly larger corresponding to the additional effort to correct estimation of flaw location and insure it is not at a vital point in the object. Hence we would typically have

$$f \gg e > h > g \quad (2.55)$$

In order to obtain a well specified flaw detection problem we set up a risk minimization problem. For this we require some prior estimator ζ_k of the probability that w_k occurs [flaw in pixel (i,j)]. When ζ is the probability of no flaw and all other ζ_i are equal

$$\zeta(w_k) = \zeta_k = \frac{1 - \zeta_0}{n^2} \quad (2.56)$$

If we take decision d_k with probability p_k the total risk becomes [Reference 11]

$$\rho(\underline{\zeta}, d) = \sum_k \sum_{\ell} \zeta_k p_{\ell} \ell(w_k, d_{\ell}) = \underline{\zeta}^T L \underline{p} \quad (2.57)$$

The decision which minimizes $\rho(\underline{\zeta}, d)$ (depends on the estimate of the distribution $p(\underline{a})$) is called the Bayes decision d^* . In order to minimize $\rho(\underline{\zeta}, d)$ we need to choose a function $\delta(\underline{a})$ and have only to minimize, following [Reference 11]

$$\sum_k \ell[w_{\ell}, \delta(\underline{a})] \zeta_k p(\underline{a} | w_k) \quad (2.58)$$

(Note here $p(\underline{a}|\underline{w}_k)$ may include the measurements \underline{b} and may then be written $p(\underline{a}|\underline{w}_k, \underline{b})$). One slight problem exist now: clearly at the location of a void like flaw both mean and variance will be smaller than at other pixels and this should be expressed in $\mu_{\underline{a}|\underline{w}_k}$ and $\Sigma_{\underline{a}|\underline{w}_k}$; in the extreme, both would have a zero component at the corresponding locations. In this latter case the new distributions are obtained by precisely omitting these elements (e.g., the k^{th} element of $\mu_{\underline{a}|\underline{w}_k}$ and the k^{th} row and columns in $\Sigma_{\underline{a}|\underline{w}_k}$ are removed.) A second problem exists in specifying $p(\underline{a}|\underline{w}_k)$: As mentioned before, (under \underline{w}_0) $\Sigma_{\underline{a}|\underline{b}}$ is not of maximum rank but of rank $(n-1)^2$ due to the assumption of perfect measurements. Thus, a vector $\tilde{\underline{a}}$ with $(n-1)^2$ components carries all information about the image and we need to consider only this vector for any decisions (e.g., remove any two orthogonal strips which do not contain a void). For our Gaussian model

$$p(\tilde{\underline{a}}|\underline{w}_k) = \frac{1}{(2\pi)^{\ell/2} |\Sigma(k)|} \exp \left[-\frac{1}{2} (\tilde{\underline{a}}(k) - \underline{\mu}(k))^T \Sigma(k)^{-1} (\tilde{\underline{a}}(k) - \underline{\mu}(k)) \right] \quad (2.59)$$

where $\ell = (n-1)^2$ under \underline{w}_0 (and $\ell = (n-1)^2 - 1$ under \underline{w}_k , $k \neq 0$).

Now, minimizing Equation (2.58) with respect to a decision $\delta(\underline{a})$ requires to search over n^2+1 possibly values of $\delta(\underline{a})$ and to choose \underline{d}_k which minimized Equation (2.58). The approach is unfortunately not feasible, simply because of the size of Σ_k^{-1} , a $(n-1)^2 \times (n-1)^2$ matrix.

Alternatively, decisions can also be based on the perfect measurements \underline{b} directly. This approach is slightly simpler but quite similar. The main value of this approach is that it provides a relatively simple way to evaluate performance of certain schemes. This can permit one to suggest under what conditions measurements are of value. For example, it is perceivable, that measurements bring so little

information that it is not worth taking them - suggesting another measurement technique should be used instead.

Consider the distribution of $p(\underline{b})$. Since flaws can be located in any pixel $p(\underline{b})$ will be a mixture distribution

$$p(\underline{b}) = \sum_j \zeta_j p(\underline{b}|w_j) \quad (2.60)$$

The loss table is specified by

	d_0	d_1
w_0	0	e
w_1	f	g

(2.61)

where the notation of Equation (2.54) is used.

As to the model of $p(\underline{b}|w_j)$ we assume all elements of \underline{b} to be linearly independent e.g. by forming \tilde{A} from A in Equation (2.14), by omitting the last row. We may at this time neglect the (small) influence of a void in one pixel on the covariance of \underline{b} ; however we do not neglect the effect of a void on the mean $\underline{\mu}_b$. Taking the best decision amounts to minimizing

$$\begin{aligned} & \sum_{k=0}^{n-1} \ell[w_k, \delta(\underline{b})] \zeta_k p(\underline{b} | w_k) \\ = & \sum_{k=1}^{n-1} \ell[w_k, \delta(\underline{b})] \zeta_k \frac{1}{2\pi^{\frac{2n-1}{2}} |\Sigma|^{1/2}} \exp\left[-\frac{1}{2}(\underline{b}-\underline{\mu}_b(k))^T \Sigma_b^{-1}(\sim)\right] \end{aligned} \quad (2.62)$$

The advantage of Equation (2.62) over Equation (2.59) is the size of the matrix Σ_b - it is only $(2n-1) \times (2n-1)$ in case of using \tilde{A} from the two-scan

technique. Furthermore, we know explicit solutions to $\Sigma_b^{-1} = \sigma_a^{-2}(\tilde{A} \tilde{A}^T)^{-1}$ (by $\Sigma_a = \sigma_a^2 I$) from Equation (2.50) and $|\Sigma_b|$ is also known.

Still it is difficult to find the location of a flaw by minimizing 2.62: for n^2 pixels to be tested, each requiring evaluation of the exponent of (2.62), amounts to the order of $c \cdot n^4$ ($c \approx 5 \dots 10$) operations. Even for a modest $n=100$ the computational burden gets out of hand.

2.3.2 Distribution of quadratic and bilinear terms

We may approach the problem differently. Roughly, since we wish to minimize Equation (2.62) $p(\underline{b}|w_0)$ should be small if a flaw is present. We may then ask - how large does a flaw have to be in order to make $p(\underline{b}|w_0)$ small (relates to the power to reject the null hypothesis).

For this purpose, we consider the two scan techniques and assume a void within one pixel occupying a fraction ε of the area. Corresponding to this location (i,j) the measurements will be decreased in the i^{th} and j^{th} strip by ε , $0 \leq \varepsilon \leq 1$. Now, the distribution of the exponent of Equation (2.62) if w_0 is true (with the notation $\Sigma_b(w_0) = \Sigma_b$), is given by a χ^2 distribution, that is

$$Q = \underline{x}^T \Sigma_b^{-1} \underline{x} \sim \chi_{2n-1}^2 \quad (2.62)$$

where

$$\underline{x} = \underline{b} - \underline{\mu}$$

For $(2n-1)$, large, $\chi_{2n-1}^2 \approx N(2n-1, 2n-1)$. Thus, under w_0 and for large n , $p(\underline{b}|w_0)$ will be considered small (or too large for the model) in the rare instances when

$$|\underline{x}^T \Sigma_b^{-1} \underline{x} - (2n-1)| > T \sqrt{(2n-1)} \quad (2.64)$$

where we will typically consider $T=3\dots 5$ (Figure 2.10).

If however a flaw is present inequality (Equation 2.64) may easily come true. In this event \underline{x} will be changed to

$$\underline{x}' = \underline{x} - \epsilon [000\dots 1\dots 000\dots 1\dots 000]^T \quad (2.65)$$

where the nonzero components at locations k and ℓ express the void in two directions of projections. The distribution of this new exponent Q' can be found by use of $\Sigma_b^{-1} = \sigma_a^2 M$

$$Q' = \sigma_a^{-2} \underline{x}^T M \underline{x} - 2\epsilon \sigma_a^{-2} ([\text{row}_k(M)] + [\text{row}_\ell(M)] \underline{x} + \sigma_a^{-2} \epsilon^2 (m_{kk} + 2m_{k\ell} + m_{\ell\ell})) \quad (2.66)$$

Here, M is known to be $(A A^T)^{-1}$. Although the distribution of Q is a noncentral χ^2 a Gaussian approximation should be possible. Finding an approximation or a bound would be interesting. In fact we know all the $m_{k\ell}$'s and the covariance structure of \underline{x} . A lengthy and tedious operation (see appendix A2.2) using the approximations to the $m_{k\ell}$'s in Equation (2.50) yields an interesting result (k and ℓ are from orthogonal scans) with regard to the variance of second term in Equation 2.66:

$$\begin{aligned} y &= \text{var}[(2\epsilon \sigma_a^{-2} (\text{row}_k(M) + \text{row}_\ell(M)) \underline{x})] \approx (2\epsilon)^2 \cdot 2\sigma_a^{-2} n^{-1} \\ &= 8\epsilon^2 \sigma_a^{-2} n^{-1} \stackrel{\Delta}{=} 8\epsilon^2 \sigma_b^2 \end{aligned} \quad (2.67)$$

Now, depending on the relative value of $2n-1$ and y either the first term in Equation (2.66) or the second one will generate most of the spread of the distribution of Q' . For

$$\frac{\epsilon}{\sigma_a} = c > \frac{n}{2} \quad (2.68)$$

the term y will become dominant for the variance of Q' . (e.g. for very

homogenous materials). The distribution of Q' , when approximated by a Gaussian distribution, is specified by its mean and variance. For the mean [from Equation (2.66) and Equation (2.50)] and the variance when equation 2.68 holds (very homogenous materials)

$$\begin{aligned} E[Q'] &\approx (2n-1) + 2\epsilon^2 \sigma_a^{-2} n^{-1} \\ \text{var}[Q'] &\approx 8\epsilon^2 \sigma_a^{-2} n^{-1} \end{aligned} \quad (2.69)$$

implying

$$Q' \sim N(2n-1 + 2\epsilon^2 \sigma_a^{-2} n^{-1}, 8\epsilon^2 \sigma_a^{-2} n^{-1}) \quad (2.70)$$

while for the correct model

$$Q \sim N(2n-1, 2n-1) \quad (2.71)$$

Both distributions are drawn in Figure 2.10. They show how much of the distribution of Q' falls into a region which contains almost all of Q . This implies, if we observe a value Q^* which satisfies

$$|Q^* - (2n-1)| > T\sqrt{2n-1} \quad (2.72)$$

we are, depending on the threshold value T (T typically 3...5) almost certain of the lack of fit of the assumed model. However, conversely, when

$$|Q^* - (2n-1)| \leq T\sqrt{2n-1} \quad (2.73)$$

there is still a good chance that this is simply due to the wide spread of Q' when using the false model. Thus a rough bound for accepting the false model (decision d_ℓ , $\ell \neq k$) when w_k arises with probability ζ_k is, from elementary considerations (Figure 2.10), use of Equation (2.70) and given value T ,

$$P_1 < \frac{1}{\sqrt{2\pi}} \frac{\sigma_a}{\epsilon} \exp \left\{ -\frac{1}{4} \epsilon^2 \sigma_a^{-2} n^{-1} \right\} \quad (2.74)$$

$$\approx \frac{T}{\sqrt{2\pi}} \frac{\sigma_a}{\epsilon} \exp \left\{ -\frac{1}{4} \epsilon^2 \sigma_b^{-2} \right\}$$

Conversely, the error probability P_2 for rejecting the correct model is found from normal integrals for $T=3$ to be about .1% ζ_k and for $T=5$ less than $10^{-6} \zeta_k$.

In order to demonstrate the results consider the following example

$\sigma_a = 2\%$	(material density variation)
$\epsilon = 100\%$	(a void over a whole pixel)
$n = 100$	(number of independent detectors per scan)
$T = 5$	(make $P_2 \leq 10^{-6}$)

In this case $(\epsilon/\sigma_a)^2 n^{-1} = 25$ and we obtain

$$P_1 < .08 \cdot \exp(-25/4) = 1.5 \cdot 10^{-4} \approx .15\%$$

Note, however, how quickly P_1 could increase when the void does not fill all of the pixel, but say only $\epsilon = 20\%$! We remark that in this event the variance of Equation 2.70 could permit a better approximation. For this latter situation, the approach presented subsequently, namely a sequential probability ratio test, will be particularly useful.

From above numerical example it may appear that error rates are not always low enough and it may appear desirable to reduce P_1 , say by taking a second set of measurements, possibly by rotating the object by 45 degrees.

However a new set of measurements is dependent on the previous set and thus we cannot strictly assume for p scans

$$P_1 < c^p, \quad 0 < c < 1 \quad \forall p \geq 1 \quad (2.75)$$

Fortunately, there is evidence that for $p \ll n$ above approximation is good. To illustrate this we discuss two considerations.

First we may try an educated guess about the distribution of Q' when p scans are performed. The value $y(p)$ corresponding to Equation (2.67) is presumably proportional to p when $p \ll n$. For example, in the derivation for $y(2)$ in appendix A2.2 summation over terms of order n^{-1} have to be performed in proportion to the number of stripes, (there $p=2$), over laying a flaw. Provided all other summations over terms of order n^{-2} contain many less than n terms, e.g. $p \ll n$, they may remain small. This argument hinges of course on the assumption that terms corresponding to t_i of Equation 2.50, for $p > 2$, do not change much in their proportion when p changes. This again seems plausible when $p \ll n$.

A second interesting consideration is the observation of the determinant of Σ_b . The square root of the determinant is comparable to volume in a space of random variables and is used for example as a scale for the Gaussian distribution. Compare now from Equation 2.50 how on the one hand $|\Sigma_b|^{1/2} \sigma_a^{-1} = M^{1/2}$ depends on n , namely, $|\Sigma_b|^{1/2} \propto n^{(n-1)}$. On the other hand, when all off diagonal elements are omitted, obviously $|\tilde{\Sigma}_b|^{1/2} \propto n^{n-1/2}$, showing it spans comparable volume despite neglect of these terms.

Furthermore, when only a single scan is used, neglect of off diagonal elements in Σ'_b leading to $\tilde{\Sigma}'_b$ does not change the determinant since Σ'_b is diagonal (only the left upper quadrant of Σ_b is used). Hence $|\Sigma'_b|^{1/2} = |\tilde{\Sigma}'_b| = n^{n/2}$. This result is summarized in Table 2.5 for $p=1$ and $p=2$ scans. It shows the exponent of $|\Sigma|^{1/2}$ grows nearly proportional to p and omission of off-diagonal terms (= considering dependency of measurements) changes the determinant only by a small factor (compared to changes associated with changing n). This

observation is suggestive of similar behavior of these determinants for $2 < p \ll n$ and is indicative of the usefulness of a stochastic model in which p independent scans (evenly distributed around the object) are taken.

TABLE 2.5: Value of Determinants

p	1	2
$ \tilde{\Sigma}_b $	n^n	n^{2n-1}
$ \Sigma_b $	n^n	$n^{2(n-1)}$

From all these considerations, we expect the distribution of Q' to "spread" only slowly with p and to a first approximation we may use

$$Q' \sim n(pn + p\epsilon^2 \sigma_a^{-2} n^{-1}, 4p \epsilon^2 \sigma_a^{-2} n^{-1}) \quad (2.76)$$

whenever $2\epsilon \sigma_a^{-1} \gg n$ and $p \ll n$. It seems that in practical situation this is only true for rather homogeneous materials and large flaws. (If this condition is not satisfied the variance will be much smaller and better bounds on detection of a flaw based on the method is possible). In terms of a detection scheme based on the quantity Q' one finds from elementary considerations (see Figure 2.10) the approximation

$$\begin{aligned} P_1(p) < c^p &= \frac{T}{\sqrt{2\pi}} \frac{\sigma_a}{\epsilon} \exp \{-p (\epsilon^2 \sigma_a^{-2} n^{-1})/8\} (1-\zeta) \\ &= \frac{T}{\sqrt{2\pi}} \frac{\sigma_a}{\epsilon} \exp \{-p \epsilon^2 \sigma_b^{-2}/8\} (1-\zeta) \end{aligned} \quad (2.77)$$

in concordance with Equation (2.75). Observe how the product $p\epsilon^2$ dominates error rates; this is a typical statistical phenomenon.

These observations suggest to use, with some care, approximations

leading to suboptimal decision schemes. Most importantly, it was indicated how increasing the number of projections can decrease error rates. The observation suggests to use more projections - possibly in a sequential fashion. Also for the purpose of the analytical treatment of a sequential problem, the structure of the problem has to be greatly simplified. Below we will discuss such a simplified approach which may have the robustness necessary to obtain a valid sequential approach.

2.3.3 Simplified models

A drastic simplification occurs when the correlation of measurements is neglected - at least as far as the use of their precision matrices are concerned. This is equivalent to considering only the marginal distributions of \underline{b} e.g. we assume

$$p(\underline{b}) = \prod_k p(b_k) \quad (2.78)$$

Clearly the marginals carry less information and thus any scheme based on them will perform suboptimally. Conveniently, in this simplified model measurement error is easily incorporated. Measurement error may arise from quantum mottle due to the primary beam and mottle due to scatter; scatter would introduce also a bias but we assume for the time being to know that bias and correct for it. Thus measurements are characterized for a single scan by

$$b_k \sim N(\mu_k, \sigma_k^2) \quad (2.79)$$

when no flaw is present. When a flaw of fractional area ϵ is present in, say, pixel (i,j) one of the elements of \underline{b} will change. For that element, say at location ℓ , in vector \underline{b} we obtain from Equation 2.12

$$b_\ell \sim N(\mu_\ell + \varepsilon, \sigma_\ell^2) \quad (2.80)$$

For p scans the joint distribution in the absence of a flaw may be written as

$$p(\underline{b}_1, \underline{b}_2, \dots, \underline{b}_p) = N \left(\begin{bmatrix} \underline{\mu}_1 \\ \underline{\mu}_2 \\ \underline{\mu}_3 \\ \vdots \\ \underline{\mu}_p \end{bmatrix}, \begin{bmatrix} \sigma_{11}^2 & & & & \\ & \sigma_{21}^2 & & & \\ & & \sigma_{n1}^2 & & \\ & & & \ddots & \\ & & & & \sigma_{np}^2 \end{bmatrix} \right) \quad (2.81)$$

The exponent Q of $p(\underline{b}_1, \underline{b}_2, \dots, \underline{b}_p)$ is well described by

$$Q \sim N(np, np) \quad (2.82)$$

although the slight dependency of measurements will call for some correction with small constants C_u (in dependence on σ_{k1}^2), e.g., $Q \sim N((1+C_1)np, (1+C_2)np)$. For the sake of simplicity of the analysis this small effect is neglected.

On the other hand when a flaw is present we obtain approximations for the distribution of Q' somewhat different from Equation 2.70. Similar to Equation (2.67) we compute the variance y due to the cross product between ε and $\underline{x} = \underline{b} - \underline{\mu}$. This time however, due to using a diagonal matrix in (2.81), the contribution of rows corresponding to Equation (2.66) is limited to these diagonal terms. One obtains immediately $y = (2\varepsilon/\sigma_\ell)^2$ for a single scan and for p scans, $y = \sum_{k=1}^p (2\varepsilon/\sigma_{\ell k})^2$, in concordance with the approximation Equation (2.67).

The diagonal approximation Equation (2.81) is motivated by the assumption of quantum mottle and the discussion following Equation (2.75). Here $\sigma_{\ell k}^2$ expresses the noise due to material along the entire projection stripe and will be of order $n\sigma_a^2$ plus the quantum mottle which is possibly of comparable magnitude. Hence we will use the approximation for Q'

$$Q' \sim N(np + \sum_{k=1}^p (\varepsilon/\sigma_{\ell k})^2, np) \quad (2.83)$$

In other words this model neglects the product due to ε and \underline{x} by virtue of $4 \sum_{k=1}^p (\varepsilon/\sigma_{\ell k})^2 \ll np$. For simplicity we will assume $\sigma_{\ell k}^2 = \overline{\sigma^2}$ and obtain for the presence of a single flaw

$$\sum_{k=1}^p (\varepsilon/\sigma_{\ell k})^2 = p \cdot c \quad (2.84)$$

Equations (2.83) and (2.84) suggest that the problem may be approached analytically using the sequential probability ratio test (SPRT).

From [11] define for the k^{th} single scan.

$$z_k = \log \frac{p_1(\underline{b}_k)}{p_0(\underline{b}_k)} = \log \left\{ \frac{\exp(-\frac{1}{2} Q'_k)}{\exp(-\frac{1}{2} Q_k)} \right\} \quad (2.85)$$

where all z_k have the same assumed distribution as Z , and form

$s = \sum_{i=1}^p z_i$. Choose now the following constants

$$\begin{aligned} a &\approx \log \frac{c_s}{f} - \log \frac{I_0(1-\zeta)}{\zeta} \\ b &\approx -\log \frac{c_s}{e} + \log \frac{I_1 \zeta}{1-\zeta} \end{aligned} \quad (2.86)$$

Where c_s is the sampling (scanning cost), f the cost if a flaw is missed, and e if a good object is rejected. The quantities I_0 and I_1 are given by, (using Equations (2.81), (2.82) and (2.85)) for $p=1$ scan

$$\begin{aligned} I_0 &= -E[Z | W=w_0] = \frac{1}{2} \left(\frac{\underline{\varepsilon}}{\sigma} \right)^2 \\ I_1 &= E[Z | W=w_1] = \frac{1}{2} \left(\frac{\underline{\varepsilon}}{\sigma} \right)^2 \end{aligned} \quad (2.87)$$

Then decide d_0 (no flaw) when $s \leq a$ and d_1 when $s \geq b$. If no decision is reached increase p by one (next scan). This procedure requires on the average (depending on w)

$$\begin{aligned}
p_0 &= E[k|W=w_0] \approx a \cdot \left(\frac{\sigma}{\epsilon}\right)^2 \approx 2 \left(\frac{\sigma}{\epsilon}\right)^2 \log \frac{f}{c_s} \\
p_1 &= E[k|W=w_1] \approx b \cdot \left(\frac{\sigma}{\epsilon}\right)^2 \approx 2 \left(\frac{\sigma}{\epsilon}\right)^2 \log \frac{e}{c_s}
\end{aligned} \tag{2.88}$$

scans. The Bayes risk $\rho^*(\zeta)$ is, with $\lambda = \max(f, e)$, bounded by

$$\rho^*(\zeta) < c_s' \log \frac{\lambda}{c_s} \cdot \frac{1}{\min(I_0, I_1)} = 2 \left(\frac{\sigma}{\epsilon}\right)^2 c_s \log \frac{\lambda}{c_s} \tag{2.89}$$

For illustration consider a $n \times n = 100 \times 100$ pixels area with $\sigma_a \approx 2\%$, but this time a single small void with say $\epsilon = 10\%$ only(!). Further assume the quantum mottle and other measurement noise σ_m^2 to be comparable to the noise in the projection, e.g. $\sigma_m^2 = 100 \sigma_a^2$. The total noise terms in the components of the measurement vector \underline{b} are thus $2 \times \sigma_m^2$. The variance σ_{kl}^2 in Equation (2.81) is then $n \times 2 \times \sigma_m^2 = 800 (\%)^2$. For the cost structure assume the cost of a decision error $= 10^4 c_s$ and possibly $c_s = 1\$$. Then the total risk per examination is

$$\rho \approx 1\$ \times 4 \ln 10 \times 2 \left(\frac{\sigma}{\epsilon}\right)^2 \approx \$147.4 \tag{2.90}$$

Similarly the average number of scans is 147.4. Such a large number of scans is comparable to full tomographic scanning.

If we had assumed $\epsilon = 100\%$, as in the previous example, only 1.5 scans would be suggested on the average. In this case, however, the model for I_0 and I_1 in Equation (2.87) is not valid anymore since $\epsilon^2 > (n\sigma_a^2 + \sigma_m^2)$. The SPRT suggested is limited to $\epsilon \approx 28\%$. When larger ϵ have to be considered Equation (2.87) has to be modified accordingly (crossterms leading to y of Equation (2.67) become dominant). For some further discussion of this example see also Section 4.2 where a crack of fixed orientation relative to the object is assumed while the object may have any orientation. In that case a drastic reduction of scans is possible. We should remark, when the structure of the object is simple and well

known, the computational burden for implementing this procedure is trivial as the inversion problem has not to be solved. Only the forward problem - finding the projections of the object for any given scan direction has to be computed one time by solving an expression of the type $\underline{b} = \underline{Aa}$.

An interesting question is now how the number of flaws could be determined. For a small number q of flaws, the number of possible arrangements is of the order of n^{2q} . Thus testing all of these arrangements is usually impossible.

An alternative approach is based on the use of an expression (Equation 2.82), modified to account for multiple flaws. From analogy, for q flaws

$$Q'' \sim N(np + q \sum_i (\epsilon/\sigma_i)^2, np). \quad (2.91)$$

Thus the mean of Q'' shifts q times faster with q flaws. This information can be used to estimate the number of flaws. Hence

$$E[Q'' - np] / \left[\sum_{i=1}^p (\epsilon/\sigma_i)^2 \right] = \hat{q} \quad (2.92)$$

and

$$\text{var } \hat{q} = np / \left[\sum_{i=1}^p (\epsilon/\sigma_i)^2 \right]^2 \propto p^{-1} \quad (2.93)$$

Thus, depending on the desired precision of estimating q the number p of projections can be chosen.

An alternative approach would be to observe the stopping time when decision d_1 caused stopping. Obviously, when there are more flaws one would expect a sequential sampling scheme to stop earlier - in fact - after p_1/q samples. A crude estimate of the number of flaws is therefore with p_{observed} , the number of scans at termination, and $d \neq d_0$.

$$\hat{q}' = E[k/W=w_1 = \text{single flaw}] / p_{\text{observed}} \quad (2.94)$$

One should be cautioned however when using estimate \hat{q}' . The problem is that little is known about the distribution of p observed. Already the computation of $E[p_{\text{observed}}]$ is a rather involved task - [Reference 11, section 12] and little is known about its higher moments. Thus very little can be said about the distribution of \hat{q}' (with the exception of the case $q \gg E[k|W=w_1]$; in that case Equation 2.92 or 2.93 may be used).

The location of flaws seems to require searches over all n^2 pixels. Fortunately it is unnecessary to form compound hypothesis. One way is again to use expression of the type (Equation 2.91), and treat it in precisely the same way we had used Equation 2.82 and 2.83 (or 2.91 respectively); However, instead of assuming no flaw - we assume a single flaw. With this assumption we compare the quadratic forms corresponding to the single flaw model on all n^2 pixels. When a flaw is encountered Q' is expected to change by $E[\Delta Q'] = 1 \times \sum_i^p (\epsilon'_i / \sigma_i)^2$. In this way one can proceed to search for the next flaw until q flaws are found.

A problem with this approach is again uncertainty in the actual change ΔQ of Q between hypothesis. From consideration of equt 2.69, with $x^T M x$ fixed (observed)

$$\text{var} [\Delta Q] = p \sigma_a^{-2} \text{var} [2\epsilon x_k] = 4p(\epsilon/\sigma_a)^2 \quad (2.95)$$

which we require to be small compared to $E^2[\Delta Q] \approx [p (\epsilon/\sigma_a)^2]^2$. This requirement will usually be met when p_1 close to $p_1 = E[k|W=w_1]$ scans have been performed (since this provided enough information to detect a single flaw almost certainly.) The probability of error for the detection of each individual flaw is approximately,

$$\text{Pr} [d_0 | W=w_1] \approx e^a \approx (c_s/f) \frac{\zeta'}{1-\zeta'} \left(\frac{\sigma}{\epsilon} \right)^2 \quad (2.96)$$

For the example above $\text{Pr}_{\text{ex}}[d_0|W=w_1] \approx 10^{-3} \zeta'/(1-\zeta')$ which may be an acceptable level. Here ζ' is the prior probability of a flaw on the particular location - so typically it will be $n^{-2}\zeta$, leading to $\text{Pr}_{\text{ex}}[d_0|W=w_1] \approx 10^{-7} \zeta$.

If termination of scanning is a random variable and $q > 1$ suggesting that only few scans are performed - considerably larger error probabilities would result. For the same reasons mentioned for finding the properties of \hat{q}' and the invalidity of approximation (Equation 2.96) in such a case, such simple estimation of error rates for locating flaws are not possible. In such a case one would also resort to some ranking statistics of the estimated probabilities, further complicating analysis. Some numerical studies (Monte Carlo methods) are suggested for evaluating this method.

At this point we may begin to be interested in the evaluation of the noise terms from a physical point of view. Especially, we have realized that signal-to-noise ratio determines efforts of finding flaws. The basic physics and technology are now addressed to resolve some of the associated issues. Subsequently we will turn to aspects of optimizing system performance e.g. minimizing $(\sigma/\epsilon)^2$.

3. PHYSICAL ASPECTS OF PROBLEM

The physical aspects of X-ray radiography can be divided into three major areas: (i) conversion of energy from high velocity (relativistic) electrons into X-ray energy; (ii) absorption and scattering of X-rays when trespassing matter; and (iii) detection of X-rays. This natural division into three areas corresponds to a simple modeling of components in primitive X-ray radiographic arrangement [Figure 3.1]. It will become clear later that such a strict association of physical mechanisms with systems components is not adequate. Instead, for more refined modeling, several physical mechanisms will have to be considered within each component. Since quantitative description of some of above mentioned areas is rather complicated it is clear that simultaneous consideration of these physical mechanisms will contain a considerable degree of uncertainty. How to cope with this uncertainty for the purpose of systems analysis will be described in subsequent Section 4 and 5 . This section will mainly address physical mechanisms and the relevant technology as it affects describing dominant physical mechanisms; it will indicate qualitatively the most important mechanisms to be considered in modeling systems components for a particular arrangement.

3.1 X-ray Sources

Depending on required mobility and intensity of X-ray sources either radioactive isotopes or tubes are used. Usually the X-ray intensity available in X-ray tubes is several orders of magnitude higher than in isotopes. Hence it often provides the X-ray source when stationary equipment is permissible. For the high speed NDE environment

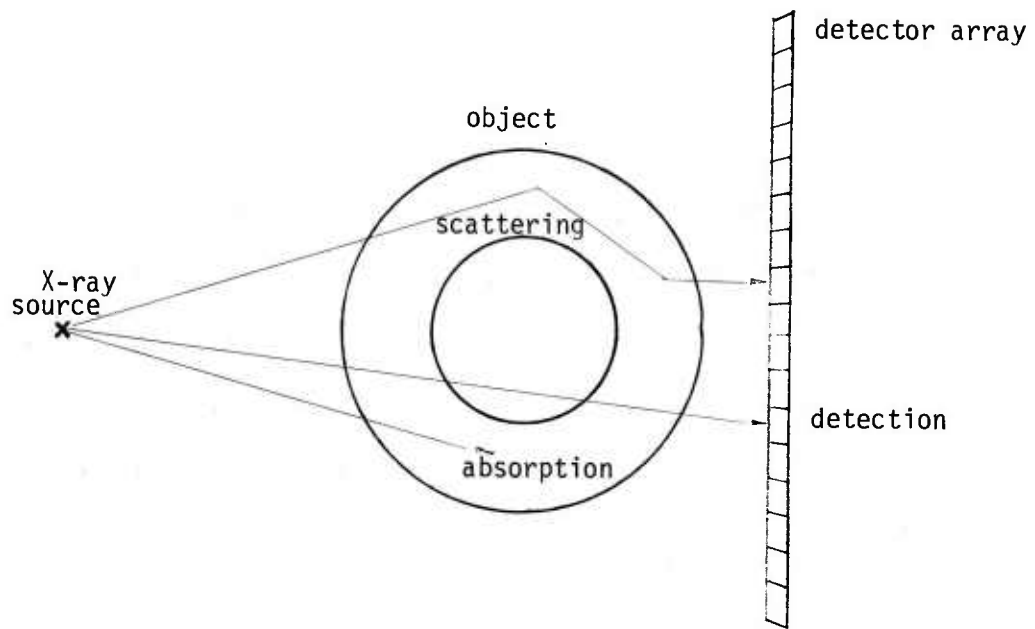


Figure 3.1: Schematic of basic X-ray imaging components

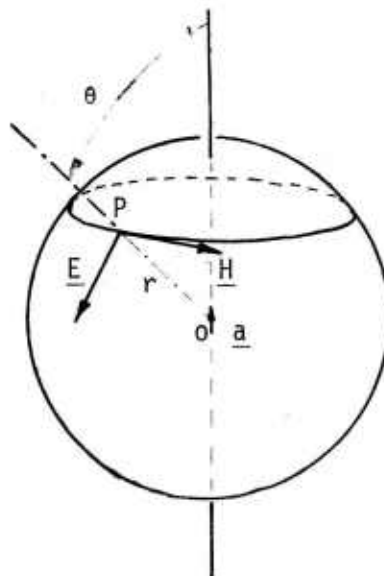


Figure 3.2: Vectorfields \underline{E} and \underline{H} , after time $t=r/c$, due to acceleration \underline{a} of a positive charge at O .

tubes appear to be preferable, as will be shown, and hence we will mainly concentrate on their performance characteristics and devote only little time to radioactive isotopes.

X-ray Tubes

Since the discovery of X-rays the technology of dedicated X-ray tubes has undergone considerable development. For different applications X-ray tubes are tuned in different ways [References 5, 22, 32] and differ in:

- spectral properties
- range of anode voltage and current
- beam shape and intensity
- mode of operation - pulsed versus continuous
- focal spot size and shape
- stability of characteristics and life expectancy
- power supply requirements (DC or radiofrequency for linear accelerators)
- mechanical robustness
- anode material (Tungsten, Molybdenum, Silver, etc)
- stationary vs. rotating anode
- anode cooling (radiative vs. fluid cooling)
- production of scattered electrons (which generate X-rays in areas other than the focal spot)
- control of electron beam geometry (due to filament aging, space charge)
- cost

Some of the basic considerations which lead to the variety of tubes in use today will now be given.

The earliest theory about the generation of X-rays is based on the

concept developed by JJ. Thompson and Lorentz; this theory is based on Maxwell's electrodynamics [Reference 8, Chapter 2]. According to this theory an electron which is accelerated (or decelerated) radiates a transverse electromagnetic wave (Figure 3.2). The electric field E at distance r from an electron after a time r/c is given by

$$\vec{E} = \frac{\vec{a} e}{r c^2} \frac{\sin \theta}{(1 - \beta \cos \theta)^3} \quad (3.1)$$

where \vec{a} is the acceleration (or deceleration) of the electron with relativistic speed $v = \beta c$ ($0 \leq \beta < 1$), c the speed of light in vacuum, and e the (negative) electron charge. The magnetic field \vec{H} has an intensity proportional to the intensity of \vec{E} with the direction indicated in Figure (3.2). Thus, by use of Poynting's vector \vec{S} [Reference 46] the flow of energy is given by

$$\vec{S} = \vec{E} \times \vec{H} \quad (3.2)$$

From these expressions it is apparent that roughly speaking (assume $\beta \ll 1$), "Bremsstrahlung" will occur in a direction perpendicular to the electron beam incident on the anode. If β is not much smaller than unity the beam intensity in the forward direction ($\cos \theta > 0$) will be larger than in the backward direction.

Modeling X-ray Beams

One might further suspect X-rays to be polarized in a plane passing through the vector \vec{a} . (Equation 3.1). However, when electrons hit a target material deviations from this simple theory occurs: the electron is not decelerated instantaneously but propagates within the anode material along some random trajectory. Furthermore one has according to de Broglie to consider the wave nature of electrons which constitute wavelets with length comparable to internuclear distances. A description of these relativistic quantum mechanical mechanisms were

given by Sommerfeld (1929) and are in reasonable accord with results on thin targets [Reference 27]; interesting is the observation of hard X-rays (most penetrating being highly polarized while lower energy components of the X-ray spectrum are not [Table 3.1]. We note at this point the relation between the shortest observed wavelength λ_{\min} in a spectrum generated by the tube with voltage U , as a consequence of quantum mechanics, is determined by [Reference 32]

$$\lambda_{\min} [\text{\AA}] \approx 12.3 U [\text{kV}] \quad (3.3)$$

Typical X-ray spectra are depicted in Figure 3.3 and show maximal intensity in a band $d\lambda$ at $3/2 \lambda_{\min}$. For a given supply voltage the intensity of the spectrum may be approximated by an expression of the type

$$I(\lambda) = cZ \left(\frac{1}{\lambda_{\min}} - \frac{1}{\lambda} \right) \cdot \frac{1}{\lambda^2} u(\lambda - \lambda_{\min}) \quad (3.4)$$

by use of [Reference 8, p. 105] and $d\nu = -cd\lambda/\lambda^2$. When it is desired to account also for characteristic spectral lines at wavelength λ_j and partial absorption of X-rays in the target, a more general model of the type

$$I(\lambda) = u(\lambda - \lambda_{\min}) I_0 [1 - \sum a_i e^{-\alpha_i (\lambda - \lambda_{\min})}] \left(\frac{\lambda_{\min}}{\lambda} \right)^p + \sum_j b_j \delta(\lambda - \lambda_j) \quad (3.5)$$

where $\delta(\cdot)$ is Dirac's delta function and $p \geq 2$ may be used.

From earlier discussion it might also be desirable to model partial polarization of X-rays at high energy. Excluding the unpolarized fluorescent lines in the spectrum, this may again be accomplished by functions of the type $e^{-\gamma\lambda}$. In a simple case such as with Kulenkampf's thin foil [Reference 8, his Figure II-20], the two

Table 3.1
THEORETICAL POLARIZATION OF THE CONTINUOUS RADIATION

Frequency	Percent Polarization
$\nu = \nu_{\max}$	100
$\nu = 3/4 \nu_{\max}$	82
$\nu = 1/2 \nu_{\max}$	57
$\nu = 1/4 \nu_{\max}$	24

From [42].

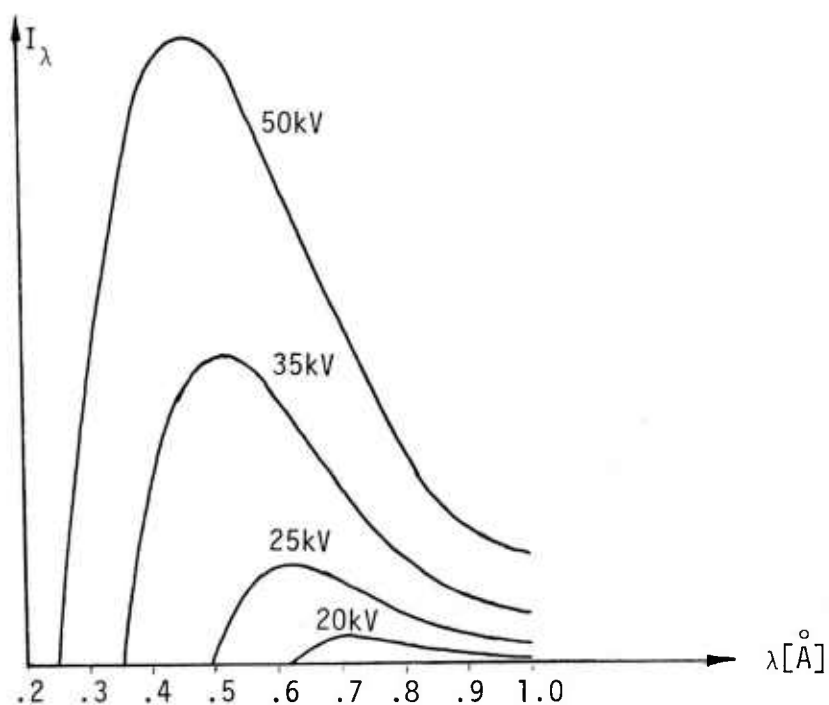


Figure 3.3: Schematic of typical X-ray intensities I_λ as function of λ and tube voltage (Tungsten target, after [8, p 38]).

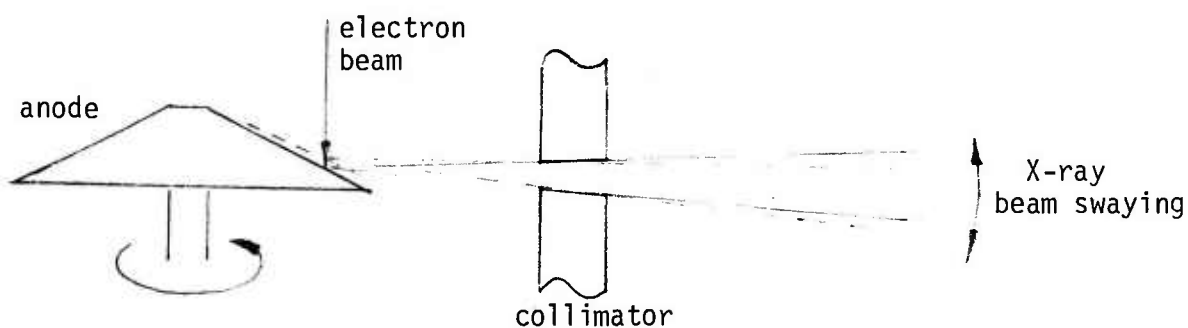


Figure 3.4: Problem of beam swaying due to wobble of target anode.

components may be approximated by

$$I_{\parallel}(\lambda) = c \cdot e^{-\gamma(\lambda - \lambda_{\min})} I(\lambda) \quad (3.6)$$

$$I_{\perp}(\lambda) = (1 - c \cdot e^{-\gamma(\lambda - \lambda_{\min})}) I(\lambda)$$

$$0 \leq c \leq 1$$

Following Compton [Reference 8, p95, p111, p112] c would have to lie between zero and unity. Further difficulties in describing X-ray intensity arise from consideration of spatial distribution. Equation (3.1) expresses already a dependency of X-ray intensity on spatial direction, but there is an additional effect called the heel effect. This effect arises in the following way: X-rays are generated in good part at some depth in the target material. Hence, depending on the direction in which they leave the target they have to trespass different distances of the target material and are filtered differently. Thus, not only will the intensity change in dependence on direction θ but also in dependence on the direction ϕ [Figure 3.6]. Presumably these variations will be slow functions of ϕ and θ . With this assumption and from symmetry around $\phi = 0$ we may use as an approximation for $I(\lambda)$

$$I(\lambda, \theta, \phi) = I_0(\lambda) \left\{ 1 - \begin{bmatrix} \theta - \theta_0 \\ \phi \end{bmatrix}^T \begin{bmatrix} g & 0 \\ 0 & h \end{bmatrix} \begin{bmatrix} \theta - \theta_0 \\ \phi \end{bmatrix} \right\} \quad (3.7)$$

in some neighborhood of $\theta = \theta_0$ and $\phi = 0$. Sommerfeld, as cited by Compton [Reference 8, p 114] (neglecting heel affect), suggests that near λ_{\min} the angle of maximum emission θ_0 should satisfy the differential equation

$$\frac{d}{d\theta} \frac{\sin^2 \theta_0}{(1 - \beta \cos \theta_0)^4} = 0; \quad (3.8)$$



Figure 3.5: Example of possible focal spot X-ray intensity, viewed face on through the pencil beam collimator of Figure 3.4. (after [Reference 5]).

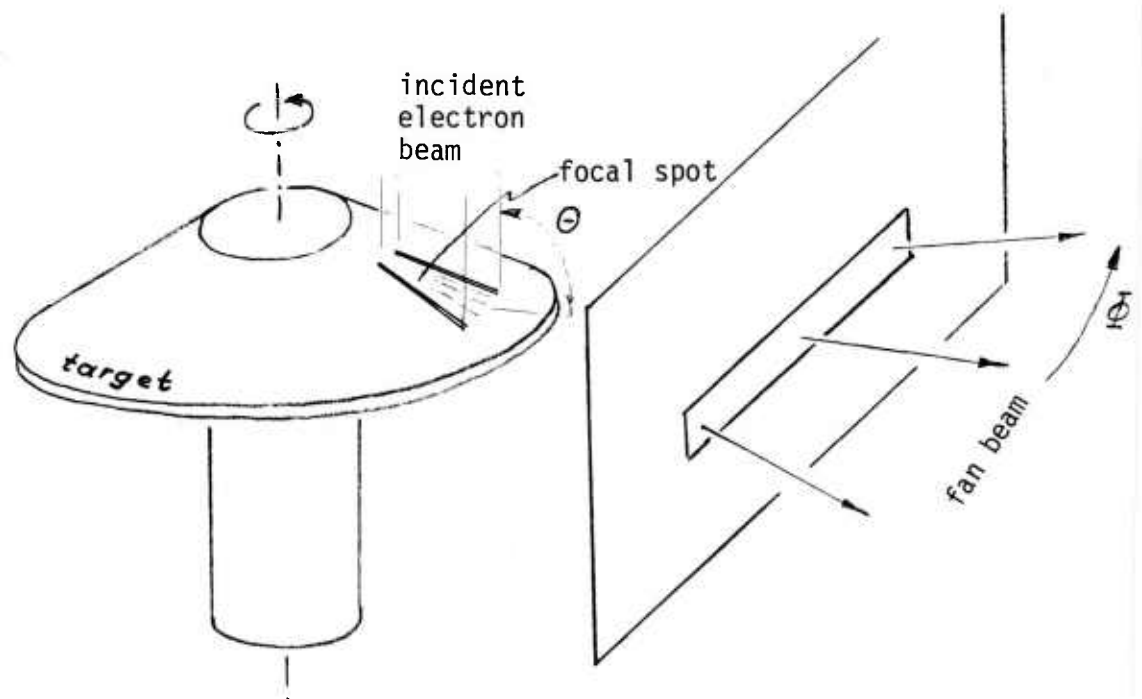


Figure 3.6: In a fan beam geometry the apparent focal spot shape depends on viewing direction

For small β , θ_0 is approximated by

$$\theta_0(\lambda_{\min}) \approx \arccos 2\beta. \quad (3.9)$$

For $\lambda > \lambda_{\min}$ it is found experimentally and theoretically [Reference 8, p. 115] that for maximum X-ray intensity $\theta_0(\lambda) < \theta_0(\lambda_{\min})$. For illustration, for $\beta = .25$ ($\approx 16.5\text{kV}$, $\lambda_{\min} = .75\text{\AA}$) $\theta_0 \approx 60^\circ$. As far as $g(\lambda)$ and presumably $h(\lambda)$ are concerned, it appears from Compton's data (his Figure II-11) that they are not strong functions of λ .

Another important variable in describing X-ray intensity is the anode voltage. Understanding its effect on the X-ray spectrum is important because slight variations of hardness may result in large variations of intensity of X-rays trespassing an object. Two references addressing this issue are Reference [5] and [22]. Kramers Reference [26] finds also as a description of anode performance as a function of supply voltage in relatively good accord with experimentation for the efficiency η of X-ray generation

$$\eta = \frac{4\pi}{3\sqrt{3}\ell} \frac{e^3}{m_e h} c^3 Z \cdot U \approx 10^{-6} Z U_{[\text{kV}]} \quad (3.10)$$

m_e mass of electrons

e electron charge

ℓ numerical factor of about 6

Z atomic number

h Planck's constant

c speed of light in vacuum

Thus for Tungsten target ($Z=74$) and $U=100\text{kV}$ an efficiency of about .75%

is found. In concordance [Reference 32] gives a quadratic relation for the intensity of the continuous spectrum to tube voltage U :

$$I = k U^2$$

McGonnaght describes furthermore that the maximum of the intensity in X-ray spectra (from tubes) occurs at about $1.5\lambda_{\min}$ corresponding to 2/3 of the supply voltage. These relationships suggest for the dependency of $I_\lambda(\lambda)$ on U , at the high frequency end (where most power is concentrated (under the condition of constant supply current of the tube) for a band of width $d\lambda$ (Appendix 3.1)

$$I_\lambda(\lambda, U) = \left(\frac{U}{U_0}\right)^3 I_\lambda\left(\lambda \cdot \frac{U}{U_0}\right) \quad (3.11)$$

and for the quantum count density S in $d\lambda$

$$S_\lambda(\lambda, U) = \left(\frac{U}{U_0}\right)^2 S_\lambda\left(\lambda \cdot \frac{U}{U_0}\right) = \frac{\lambda}{ch} I_\lambda(\lambda, U) \quad (3.12)$$

When anode power P_a is limited, e.g., anode current is given by

$I = P_a/U$, S is reduced in such a way that [Appendix 3.2]

$$\int_{\lambda_{\min}}^{\infty} S(\lambda, U, P_a) d\lambda = S_0(P_a) \quad (3.13)$$

This is an important relation which suggests that for power limited anodes only the fraction of X-rays penetrating an object can be controlled via U but not the incident flux of photons.

With regard to the tails in models for spectra (Equation 3.4) it should be said that Equation 3.11 is compatible with the observation that tails of X-ray spectra do not cross for different supply voltages [Figure 3.3], while other models would not necessarily satisfy this observation.

With regard to modeling the dependency of characteristic spectral lines on U we refer to Compton [Reference 8] who suggests from experimental evidence $b_j \sim (U/U_0)^n$ in Equation (3.5).

Heat Dissipation and Power Supply of X-ray Tubes

Below supply voltages of several MV most of the kinetic energy of the electron beam is converted into heat and only a small fraction into X-rays. Thus heat dissipation limits often X-ray output. Two methods are used to allow high local heat dissipation. One is to cool the anode material locally, for example with oil or water. Alternatively the electron beam is moved relative to the anode; this is accomplished either by rotating the anode with up to 10,000 rpm or in a technique currently under development [Reference 5] by guiding the electron beam over a large anode which encircles the target. The advantage of these latter techniques is the small permissible focal spot size with a relatively high power density; the disadvantages are either a rather limited total power dissipation (rotating anode) or high equipment cost and difficulties with electron beam steering (moving beam).

A few words should be said about the power supply. In high quality imaging systems it is desired to use DC supply voltage with little ripple (constant beam hardness). For high power outputs (pulsed up to 100kW) it is obtained from 3 or 6-phase systems. Additional electronic equipment controls supply voltage to within a fraction of a percent. Residual voltage fluctuations will usually contain some harmonics of the line voltage and possibly some flicker

noise due to electronic equipment.

In order to minimize detector noise (Section 3.4) and motion artifacts, the production of X-rays is often pulsed. Pulse duration is limited for a given flash energy by maximal cathode filament current, space charge, and heat storage of target material and lies for typical CT-scanners (GE 8800) between 1 and 12 msec. Note that for an anode rotating with 10000 RPM heat will be deposited on a 60° sector for a 1msec pulse. If these pulses do not occur in certain even intervals - so as to heat the anode evenly - the anode will warp due to uneven heat deposition [Reference 5]. In conjunction with collimation this may lead to beam swaying [Figure 3.3]. Furthermore, anode wear will be uneven and the anode will develop microcracks.

All of these effects will lead to periodic variations of the X-ray output. Braun [Reference 5] holds these mechanisms responsible for severe artifacts in fourth generation CT-scanners. Note that probably intensity and beam hardness vary as the angle of incidence of electron changes (compare Equation 3.1 and 3.7).

As a final characteristic of X-ray tubes one should consider focal spot size. Often the intensity of the focal spot is bimodal - possibly as shown in Figure 3.5. In case of fan beams it is also clear that the effective spot geometry will change in dependence on the direction within the fan beam [Figure 3.6]. In closing it should be pointed out that for the very high energy X-ray range (MV) linear accelerators and Betatrons are necessary. They use either RF linear arrays of electric fields, or magnetic fields with circular symmetry. In application to thick objects they are essential.

In retrospect many mechanisms contribute to uncertainty and hence noise in the test signal - the X-ray beam. The uncertainty concerns spectral composition, directional variations and uncertainty about the precise place of origin of an X-ray photon. Since signal-to-noise ratio limits acquisition of information the understanding of these noise mechanisms is important.

Radioactive isotopes

Radioactive isotopes produce in most application much less intensity than X-ray tubes. Activities of isotopes is measured in Curie-units. One Ci corresponds to $3,7 \cdot 10^{10}$ decays/sec. From typical values of such sources we find a production of between 10^{10} and 10^{11} rays/sec.

	halflife	activity/ci	spot size	-quanta MeV
Cs - 137	30a	.5	3 x 3	.662
Co - 60	5.26a	2	2 x 2	1.17, 1.33
Ir - 192	74d	25	2 x 2	.296, .308, .316 .468, .605

Table 3.2 after Glocker, [Reference 15, p 33-35]

For comparison a rotating anode tube at 100kV will produce within a 1msec pulse of .1A (typically they go up to .5A) in excess of 10^{12} photons. This implies the potential of performing NDE via tubes some four orders of magnitude faster than with any radioisotope. It will be shown later that this potential can usually be fully exploited by current detectors [Section 3.4].

An attractive feature of above radioactive isotopes (Table 3.2) is their short-term, say on a minute basis, stability and their simple and stable spectrum. Despite this apparent advantage it appears doubtful at the current time whether, or under what circumstances, performance superior

to that with X-ray tubes could be achieved.

3.2 Properties of X-rays Absorption and Secondary Radiation

When X-rays travel through matter their intensity decreases due to absorption, and scatter (and above 1.02 MeV pair production). The relation of the decline of intensity of a monochromatic X-ray beam passing through an object is well know to follow

$$I(x) = I_0(x) \cdot e^{-\mu \rho x} \quad (3.14)$$

where $\mu = \mu(\lambda)$ is the attenuation coefficient and ρ the specific density. The coefficient μ is composed of absorption τ and scatter σ ([Reference 15, p38])

$$\mu = \tau + \sigma \quad (3.15)$$

and is dependent on wavelength λ and chemical composition of the object.

For an object with fractions α_i of atoms species i the absorption is given by

$$\mu = \rho \sum_i \alpha_i \frac{\mu_i}{\rho_i} \quad (3.16)$$

Some typical values for μ/ρ for carbon, aluminum, silver and lead are given in Table 3.3.

Table 3.3 Specific Absorption μ/ρ after McGonnagle [Reference 32]; values are in $[\text{cm}^2/\text{g}]$.

U_{equiv}	$\lambda / \text{\AA}$	C	Al	Ag	Pb
100kV	.12	.151	.168	1.36	5.15
41kV	.3	.206	.55	17.5	13.6
24.67	.5	.325	1.92	9.7	55
17.37	.71	.61	5.22	28	140
12.3	1.00	1.37	14.1	73	77

Note that attenuation coefficients do not necessarily decrease monotonically with wavelength. This is particularly striking for heavy elements such as Ag and Pb and is a result of the so called absorption edges arising due to K, L, M etc shells of the atom (Figure 3.7). For light elements such as C (e.g. Z=29, below Cu) the high energy K- edges are at energies below 12 kV.

For us it is important to express μ and its components τ and σ as functions of λ algebraically. The expressions found by Compton [Reference 8] for τ are useful. He finds, for the photoelectric absorption depending on the particular absorption mechanism involved (K shell, L_I , L_{II} , L_{III} , etc are involved) for wavelength shorter than a particular absorption edge

$$\tau \propto \lambda^m Z^n \quad (3.17)$$

where $m = 3...4.5$ and $n = 3...7.5$. The dominant mechanism however result in a τ where $m \approx 3.5$ and $n \approx 4.5$.

For energies above 60kV Cho[Reference 6, p45] suggest a relation of the type

$$\tau = kf(\lambda) \cdot Z \quad (3.18)$$

and for still higher energies, say in the MV range,

$$\mu_{\text{pair}} = k_1 Z^2 \ln \frac{Z h}{\lambda_{m_e} c} - k_2 \quad (3.19)$$

As to the mechanisms of X-ray interaction Compton [Reference 8] realized that with increasing X-ray energy X-rays are not necessarily completely absorbed when ejecting an electron. Instead their energy is diminished and in relation to their new direction of propagation, eject a low energy Compton electron. The change of energy obeys the uncertainty

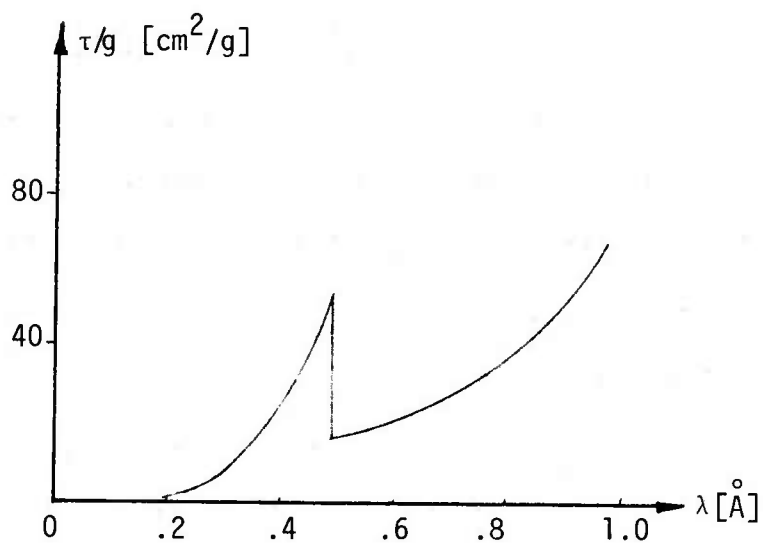


Figure 3.7: Schematic of K-absorption edge of Ag; after [Reference 15].

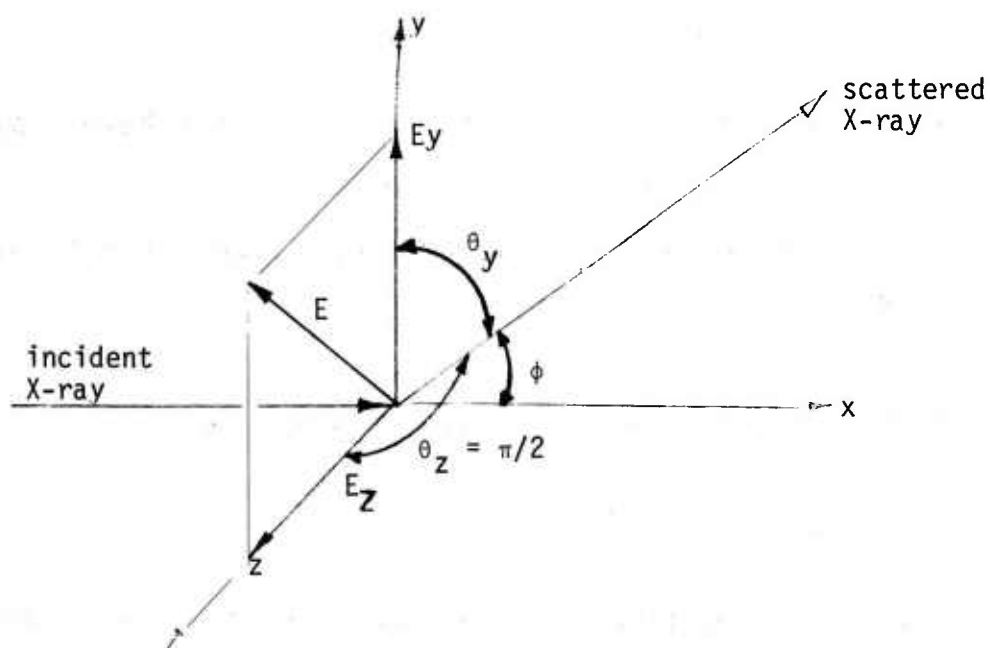


Figure 3.8: Notation used for J.J. Thomson's scattering model; after [Reference 8, p 117]

principle and hence the scattered radiation is incoherent.

The production of Compton scattered, incoherent, (or sometimes called modified) radiation can thus be related to the absorption by use of data regarding the relative production of photo electrons (complete absorption of X-ray) to the production of Compton Electrons. Such data is provided by Glocker [Reference 15] and shown for Water. [Table 3.4] An extra column expressed the ratio of the number of Compton scattered X-rays to photo absorbed X-rays. For still higher energies refer to Table 3.5. Here pair production [an electron and positron are generated] becomes important and eventually dominates Compton scattering.

These observations have some important consequences (consider Table 3.4). Roughly, when an object absorbs a fraction of X-rays (which seems to be desirable - otherwise no projections of the object would arise) the number of scattered X-rays must be proportional to N_c/N_{ph} times that fraction. Thus, when the absorbed fraction is large and the energy of primary X-rays is high, say 100 keV, almost all of the X-rays eventually leaving the object are scattered X-rays!

The pair production mechanisms seems to work in the reverse way [Table 3.5]. When the primary X-ray exceeds 1.02 MeV ($\alpha > 2$, compare Equation 3.30) it has a chance to generate an electron-positron pair of 1.02 MeV energy. The residual X-ray energy is thus 1.02 MeV smaller than that of the primary X-ray. This lower energy X-ray may have much less penetration than a primary X-ray and may disappear in a likely second interaction. However, from Table 3.5 it is seen that for energies slightly above 1.02 MeV only few X-rays are affected by this mechanism. Note, for still higher energy X-rays where a larger fraction of X-rays is affected by pair production of secondary X-rays the hardness of secondary X-rays comes close to that of the primary X-rays.

TABLE 3.4 Relation of number of photo absorbed and Compton scattered X-rays; E_{phot} and E_{compt} refer to the energy of respective electrons. After [Reference 15]

$\lambda[\text{\AA}]$	$h_{\gamma}[\text{keV}]$	%	$E_{\text{phot}}[\text{keV}]$	%	$E_{\text{compt}}[\text{keV}]$	$N_{\text{c}}/N_{\text{ph}}$
.809	15.3	99.6	14.8	.4	.87	.07
.404	30.7	98.7	30.2	6.3	3.3	.62
.202	61.4	52.4	60.9	47.3	11.9	4.65
.101	122.8	8.4	122.3	91.6	39.7	33.59

TABLE 3.5 Relation of pair production [requires $\alpha \geq 2$] to Compton scattering of X-rays. After [Reference 15]

$\lambda[\text{\AA}]$	$h_{\gamma}[\text{MeV}]$	%	$E_{\text{comp}}[\text{MeV}]$	%	$E_{\text{pair}}[\text{MeV}]$	$N_{\text{p}}/N_{\text{c}}$
.0124	1	100	.8	0	-	0
.0025	5	90	4.8	10	4	.13
.0012	10	73	9.8	27	9	.40
.0006	20	50	19.7	50	19	1.09
.00025	50	26	49.8	74	49	2.89

3.3 Scattering of X-rays

The simplest model for scattering of X-rays can be approached by J.J. Thomson's model of accelerated charges. Thus, the electric field of an incident X-ray accelerates an electron which in turn radiates a counterphase electromagnetic wave. In this model the radiated field has the same frequency (=coherent) as the incident X-ray. The electric field of radiation from a polarized X-ray is given by

$$E_{\theta} = \frac{E e^2 \sin \theta}{r m_e c^2} \quad (3.20)$$

(Compton, [Reference 8]) with circular symmetry around Y axis [Figure 3.8]. The ratio of the intensities of the incident and scattered ray is given by

$$\frac{I_{\theta y}}{I} = \frac{e^4 \sin^2 \theta y}{2 r^2 m^2 c^4} \quad , \quad \frac{I_{\theta}}{I} = \frac{e^4}{2 r^2 m^2 c^4} \quad (3.21)$$

and for unpolarized X-rays

$$\frac{I_{\phi}}{I} = \frac{e^4}{2 r^2 m^2 c^4} (1 + \cos^2 \phi) \quad (3.22)$$

[Reference 8]. For n independently scattering electrons (light elements) the fraction of primary energy scattered per unit length of path follows, [8] for n electrons

$$\sigma = \frac{8\pi n e^4}{3 m_e^2 c^4} \quad (3.23)$$

Under these conditions it can be shown that $\sigma/\rho \approx .2 \text{ cm}^2/\text{g}$ independent of the wavelength.

In the range of .2 to 1.0 \AA this theory gives within a factor of

1.5 the correct value of scattering for Carbon ($Z=6$). For heavier atoms scattering increases with Z fairly linearly including iron ($Z=26$) and more than proportional for heavier atoms [Reference 8, his Figure III-3].

There are further deviations from this theory Equation (3.23). One concerns the deviation of the scattered intensity as a function of scattering angle from that predicted by Thomsons Theory. For example for mesitylene (liquid) $[C_6H_3(CH_3)_3]$ at $\lambda = .71\text{\AA}$ a peak of the scattered intensity at $\theta = 10^\circ$ some 10 times that predicted theoretically is observed. This peak is due to the small phase difference between different atoms (with their associated electrons). More formally for polyatomic structures scattering (coherent scattering) is given by Debyes formula [Reference 8]

$$I_c = I \sum_1^p \sum_1^p F_m F_n \frac{\sin x_{mn}}{x_{mn}} \quad (3.24)$$

where in turn

$$x_{mn} = 4\pi \frac{s_{mn}}{\lambda} \sin(\phi/\lambda) \quad (3.25)$$

with s_{mn} the distance from the m^{th} to the n^{th} atom. The quantity F_m is the atomic structure factor of the m^{th} atom and F is

$$F = \sum_j f_j = \sum_{k=1}^Z \int_0^\infty u_k(a) \frac{\sin ka}{ka} da, \quad (3.26)$$

determined by the potentials u_k of its z electrons (the potential of the nuclei are neglected since their mass is very large and hence they cannot strongly radiate). These structure factors are tabulated in the International Tables of X-rays [Reference 20]. Note that with increasing beam hardness ($\lambda \rightarrow 0$) the maximal amplitude of scattered radiation must decline like $1/\lambda$ by virtue of Equations 3.25 and 3.24 respectively.

As mentioned before in addition to coherent scattering, Compton found an incoherently scattered X-ray component. The effect is due to the impulse of the X-ray photon $h\nu/c = h/\lambda$ which causes scattering electrons to recoil. Thus scattered X-rays have lower energy. The relation is expressed, for a scattering angle ϕ , by

$$\delta\lambda [\text{\AA}] = .0242 (1 - \cos\phi) \quad (3.27)$$

Considering the associated recoil factor R

$$R = 1/[1 + \frac{h}{mc\lambda} (1 - \cos\phi)]^3 \quad (3.28)$$

according to Breit and Dirac (as cited by [Reference 3]) the total scattering by a molecule is $I_m = I_c + I_i$

$$I_m = I_0 \left\{ \sum_m \sum_n F_m F_n \frac{\sin x_{mn}}{x_{mn}} + R \sum_m \left(Z_m - \sum_{j=1}^{Z_m} f_{mj}^2 \right) \right\} \quad (3.29)$$

Again this expression shows a reduction of scattering with increasing beam energy.

Above expression are only concerned with total scattering. For our purposes it is also important to understand the directional dependency of scattering intensity. A simplified model for this process is the free electron. Klein and Nishina [Reference 25] and Nishina [Reference 33] investigate for this case, based on Diracs relativistic quantum mechanics, intensity and polarization of scattered radiation. They find for a polarized beam with the notation shown in Figure 3.9

$$I = I_0 \frac{e^4}{m^2 c^4 r^2} \frac{\sin^2 \psi}{(1 + \alpha(1 - \cos\theta))^3} \left(1 + \alpha^2 \frac{(1 - \cos\theta)^2}{2\sin^2 (1 + \alpha(1 - \cos\theta))} \right), \quad (3.30)$$

$$\alpha = \frac{h\nu}{mc^2} \quad .$$

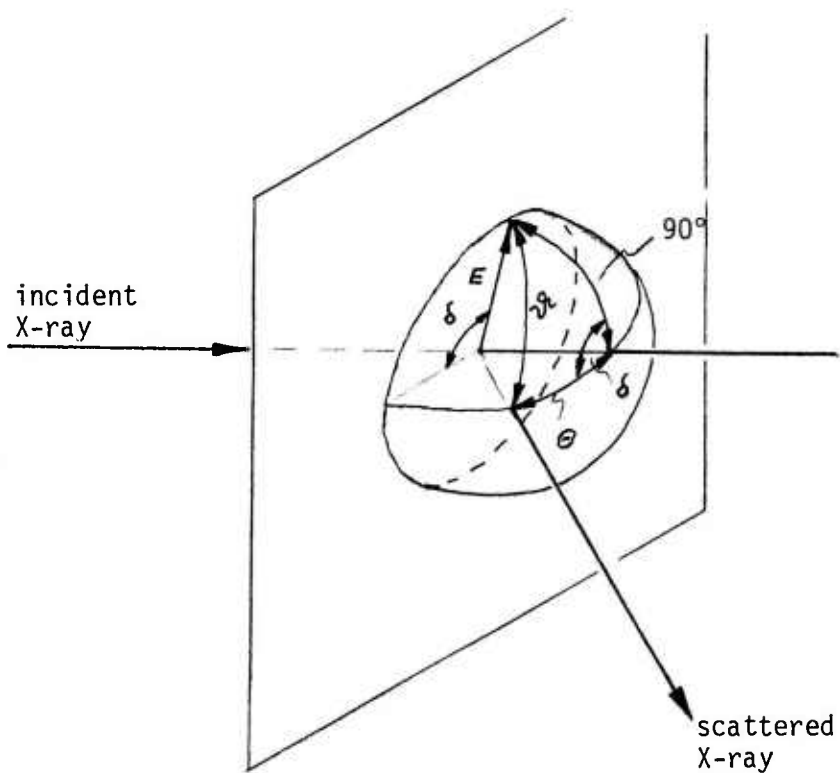


Figure 3.9: Notation used by Klein and Nishina [Reference 25,33] to describe intensity of scatter. For an unpolarized incident beam one has to average over all values of δ ; this can be done by use of the relation $\cos(\delta') = \sin(\theta) \cos(\delta)$ from spherical trigonometry.

For unpolarized radiation, averaging over ϑ with $\cos \vartheta = \sin \theta \cos \delta$,

leads to [3.31

$$I = I_0 \frac{e^4}{m^2 c^4 n^2} \frac{1 + \cos^2 \theta}{(1 + \alpha(1 - \cos \theta))^3} \left(1 + \alpha^2 \frac{(1 - \cos \theta)^2}{(1 + \cos \theta)^2 (1 + \alpha(1 - \cos \theta))} \right)$$

Note the leading term due to Thomson theory ($\alpha \rightarrow 0$). Tables 3.6, 3.7 and 3.8 show the functional behavior of these expressions. Note, in the forward direction ($\theta \rightarrow 0$) Thomson's theory describes scattering well. These expressions suggest scattering of X-rays in the order of $10^{-5}/\text{deg}^2$ and per g/cm^2 .

Above derivations are only valid for objects with negligible secondary scatter and constant intensity of trespassing radiation. Thus the volume element for which the analysis is valid must have dimensions small compared to $1/\tau$ and $1/\sigma$. For larger objects higher order scattering and the changing intensity of trespassing X-rays must be considered. The analytical complexity of the problem is considerable, even where simplifying assumptions such as the scattering on electron gas [Reference 25, 33] are made. Some efforts to solve the problem numerically have been made by [Reference 12] (personal communication) based on Monte Carlo methods. However this approach neglects polarization. Some of the difficulties lie in finding the proper relative occurrence of different mechanisms (absorption, modified scattering, unmodified scattering) independence on wavelength. Nevertheless he claims to obtain good estimates of scattered radiation when comparison is made with experimental data. One of the shortcomings of his method is the high computational effort necessary to find good approximations.

In summary, the modeling of absorption of X-rays (which usually induces the "signal") is relatively straight forward while that of scattering

TABLE 3.6 : Scattering coefficient for single electron and polarized X-ray, as shown in Figure 3.9, up to the coefficient e^4/m^2c^2 . Note: the equivalent voltage is $U = \alpha mc^2 \approx 512 \cdot \alpha \cdot \text{KV}$. Computed from [Reference 20].

$\omega = 2\pi \cdot 10^6 \text{ R FORTHUNG}$

$U \approx 5 \text{KV}$ $\delta \longrightarrow$

ALPHA EQUALS 0.01

	0	10	20	30	40	50	60	70	80	90	forward
0	1.0000	1.0000	1.0000	1.0000	1.0000	1.0000	1.0000	1.0000	1.0000	1.0000	1.0000
10	0.9694	0.9703	0.9729	0.9769	0.9819	0.9871	0.9920	0.9960	0.9986	0.9995	0.9995
20	0.8814	0.8949	0.9106	0.9297	0.9499	0.9704	0.9820	0.9940	0.9986	0.9995	0.9995
30	0.7450	0.7741	0.8092	0.8499	0.8931	0.9337	0.9690	0.9940	0.9986	0.9995	0.9995
40	0.5827	0.6307	0.6853	0.7522	0.8235	0.8904	0.9450	0.9806	0.9930	0.9982	0.9982
50	0.4088	0.4767	0.5539	0.6487	0.7495	0.8442	0.9215	0.9719	0.9904	0.9952	0.9952
60	0.2463	0.3327	0.4310	0.5516	0.6799	0.8004	0.8987	0.9629	0.9852	0.9925	0.9925
70	0.1147	0.2160	0.3312	0.4725	0.6228	0.7841	0.8793	0.9544	0.9852	0.9944	0.9944
80	0.0580	0.1136	0.2060	0.3420	0.5047	0.6850	0.8571	0.9414	0.9706	0.9857	0.9857
90	0.0293	0.0574	0.1036	0.1811	0.2907	0.4340	0.6166	0.8254	0.9509	0.9809	0.9809
100	0.0292	0.0574	0.1036	0.1811	0.2907	0.4340	0.6166	0.8254	0.9509	0.9809	0.9809
110	0.1125	0.1381	0.1746	0.2246	0.2955	0.3845	0.4901	0.6127	0.7510	0.9031	0.9372
120	0.2392	0.3231	0.4185	0.5355	0.6745	0.8215	0.9780	1.1485	1.3311	1.5244	1.7242
130	0.3936	0.5004	0.6250	0.7688	0.9312	1.1125	1.3125	1.5312	1.7688	2.0242	2.2985
140	0.5569	0.7097	0.8871	1.0879	1.3125	1.5625	1.8375	2.1375	2.4625	2.8125	3.1875
150	0.7097	0.9168	1.1485	1.4125	1.7000	2.0125	2.3500	2.7125	3.1000	3.5125	3.9500
160	0.8337	1.0871	1.3750	1.6969	2.0500	2.4375	2.8500	3.2875	3.7500	4.2375	4.7500
170	0.9145	1.2125	1.5625	1.9500	2.3750	2.8375	3.3375	3.8625	4.4125	4.9875	5.5875
180	0.9425	1.2875	1.6875	2.1375	2.6375	3.1750	3.7500	4.3500	4.9750	5.6250	6.3000

$U \approx 51 \text{KV}$

ALPHA EQUALS 0.10

	0	10	20	30	40	50	60	70	80	90	f
0	1.0000	1.0000	1.0000	1.0000	1.0000	1.0000	1.0000	1.0000	1.0000	1.0000	1.0000
10	0.9654	0.9660	0.9690	0.9729	0.9778	0.9831	0.9880	0.9919	0.9946	0.9955	0.9955
20	0.8673	0.8707	0.8807	0.8960	0.9147	0.9334	0.9534	0.9687	0.9787	0.9821	0.9821
30	0.7207	0.7280	0.7488	0.7808	0.8200	0.8617	0.9009	0.9328	0.9537	0.9609	0.9609
40	0.5477	0.5594	0.5928	0.6441	0.7070	0.7740	0.8369	0.8847	0.9216	0.9332	0.9332
50	0.3724	0.3884	0.4342	0.4907	0.5507	0.6124	0.6759	0.7391	0.7981	0.8533	0.8533
60	0.2170	0.2365	0.2928	0.3590	0.4347	0.5192	0.6024	0.6833	0.7609	0.8353	0.8353
70	0.0983	0.1203	0.1836	0.2506	0.3297	0.4203	0.5223	0.6353	0.7583	0.8913	0.8913
80	0.0262	0.0493	0.1157	0.2173	0.3470	0.5047	0.6850	0.8850	1.0950	1.3050	1.3050
90	0.0034	0.0261	0.0913	0.2112	0.3430	0.4901	0.6524	0.8254	1.0000	1.1750	1.1750
100	0.0030	0.0260	0.1074	0.2369	0.3357	0.4408	0.5595	0.6850	0.8125	0.9425	0.9425
110	0.0556	0.1039	0.1564	0.2149	0.2746	0.3403	0.4125	0.4875	0.5625	0.6375	0.6375
120	0.1708	0.1857	0.2285	0.2821	0.3428	0.4125	0.4875	0.5625	0.6375	0.7125	0.7125
130	0.2691	0.2804	0.3126	0.3621	0.4218	0.4901	0.5625	0.6375	0.7125	0.7875	0.7875
140	0.3684	0.3760	0.3981	0.4318	0.4732	0.5225	0.5750	0.6313	0.6913	0.7550	0.7550
150	0.4577	0.4622	0.4752	0.4951	0.5225	0.5564	0.5950	0.6375	0.6850	0.7375	0.7375
160	0.5280	0.5301	0.5361	0.5452	0.5564	0.5684	0.5813	0.5950	0.6088	0.6231	0.6231
170	0.5729	0.5735	0.5750	0.5773	0.5802	0.5832	0.5861	0.5884	0.5899	0.5905	0.5905
180	0.5883	0.5883	0.5883	0.5883	0.5883	0.5883	0.5883	0.5883	0.5883	0.5883	0.5883

$U \approx 102 \text{KV}$

ALPHA EQUALS 0.20

	0	10	20	30	40	50	60	70	80	90	f
0	1.0000	1.0000	1.0000	1.0000	1.0000	1.0000	1.0000	1.0000	1.0000	1.0000	1.0000
10	0.9611	0.9620	0.9646	0.9685	0.9734	0.9786	0.9835	0.9874	0.9900	0.9909	0.9909
20	0.8119	0.8250	0.8451	0.8701	0.8985	0.9286	0.9601	0.9835	0.9900	0.9909	0.9909
30	0.6131	0.6301	0.6501	0.6701	0.6901	0.7101	0.7301	0.7501	0.7699	0.7899	0.7899
40	0.4145	0.4325	0.4525	0.4725	0.4925	0.5125	0.5325	0.5525	0.5725	0.5925	0.5925
50	0.2150	0.2350	0.2550	0.2750	0.2950	0.3150	0.3350	0.3550	0.3750	0.3950	0.3950
60	0.0150	0.0350	0.0550	0.0750	0.0950	0.1150	0.1350	0.1550	0.1750	0.1950	0.1950
70	0.0050	0.0150	0.0250	0.0350	0.0450	0.0550	0.0650	0.0750	0.0850	0.0950	0.0950
80	0.0010	0.0020	0.0030	0.0040	0.0050	0.0060	0.0070	0.0080	0.0090	0.0100	0.0100
90	0.0000	0.0000	0.0000	0.0000	0.0000	0.0000	0.0000	0.0000	0.0000	0.0000	0.0000
100	0.0000	0.0000	0.0000	0.0000	0.0000	0.0000	0.0000	0.0000	0.0000	0.0000	0.0000
110	0.0000	0.0000	0.0000	0.0000	0.0000	0.0000	0.0000	0.0000	0.0000	0.0000	0.0000
120	0.0000	0.0000	0.0000	0.0000	0.0000	0.0000	0.0000	0.0000	0.0000	0.0000	0.0000
130	0.0000	0.0000	0.0000	0.0000	0.0000	0.0000	0.0000	0.0000	0.0000	0.0000	0.0000
140	0.0000	0.0000	0.0000	0.0000	0.0000	0.0000	0.0000	0.0000	0.0000	0.0000	0.0000
150	0.0000	0.0000	0.0000	0.0000	0.0000	0.0000	0.0000	0.0000	0.0000	0.0000	0.0000
160	0.0000	0.0000	0.0000	0.0000	0.0000	0.0000	0.0000	0.0000	0.0000	0.0000	0.0000
170	0.0000	0.0000	0.0000	0.0000	0.0000	0.0000	0.0000	0.0000	0.0000	0.0000	0.0000
180	0.0000	0.0000	0.0000	0.0000	0.0000	0.0000	0.0000	0.0000	0.0000	0.0000	0.0000

TABLE 3.6 (cont'd)

U≈205kV
ALPHA EQUALS 0.40

0	10	20	30	40	50	60	70	80	90
0	1.0000	1.0000	1.0000	1.0000	1.0000	1.0000	1.0000	1.0000	1.0000
10	0.9524	0.9559	0.9598	0.9646	0.9698	0.9746	0.9785	0.9811	0.9820
20	0.8223	0.8351	0.8496	0.8673	0.8863	0.9040	0.9185	0.9280	0.9313
30	0.6424	0.6674	0.6959	0.7308	0.7679	0.8078	0.8498	0.8908	0.9262
40	0.4518	0.4887	0.5307	0.5823	0.6371	0.6948	0.7307	0.7582	0.7677
50	0.2828	0.2946	0.3087	0.3252	0.3434	0.3629	0.3829	0.4024	0.4199
60	0.1543	0.1674	0.1828	0.2004	0.2197	0.2404	0.2624	0.2853	0.3083
70	0.0716	0.0848	0.1012	0.1194	0.1387	0.1594	0.1812	0.2045	0.2282
80	0.0302	0.0426	0.0584	0.0784	0.1024	0.1304	0.1624	0.1984	0.2382
90	0.0208	0.0318	0.0468	0.0668	0.0928	0.1248	0.1628	0.2068	0.2568
100	0.0331	0.0424	0.0589	0.0824	0.1124	0.1494	0.1924	0.2424	0.3024
110	0.0581	0.0744	0.1019	0.1384	0.1844	0.2404	0.3084	0.3884	0.4824
120	0.0885	0.0940	0.1099	0.1244	0.1484	0.1804	0.2204	0.2684	0.3244
130	0.1194	0.1233	0.1345	0.1517	0.1727	0.1984	0.2284	0.2624	0.2984
140	0.1475	0.1500	0.1583	0.1719	0.1904	0.2134	0.2404	0.2714	0.3044
150	0.1708	0.1722	0.1762	0.1825	0.1901	0.1984	0.2064	0.2144	0.2217
160	0.1879	0.1886	0.1904	0.1946	0.2002	0.2064	0.2122	0.2182	0.2242
170	0.1984	0.1986	0.1997	0.2006	0.2015	0.2023	0.2031	0.2038	0.2044
180	0.2020	0.2020	0.2020	0.2020	0.2020	0.2020	0.2020	0.2020	0.2020

U≈307kV
ALPHA EQUALS 0.60

0	10	20	30	40	50	60	70	80	90
0	1.0000	1.0000	1.0000	1.0000	1.0000	1.0000	1.0000	1.0000	1.0000
10	0.9438	0.9473	0.9512	0.9560	0.9611	0.9668	0.9723	0.9773	0.9820
20	0.7943	0.8066	0.8206	0.8377	0.8560	0.8754	0.8954	0.9154	0.9354
30	0.5971	0.6031	0.6107	0.6204	0.6324	0.6464	0.6624	0.6794	0.6974
40	0.4015	0.4099	0.4212	0.4354	0.4524	0.4714	0.4914	0.5124	0.5344
50	0.2413	0.2512	0.2632	0.2764	0.2914	0.3084	0.3264	0.3454	0.3654
60	0.1295	0.1398	0.1519	0.1654	0.1804	0.1964	0.2134	0.2314	0.2504
70	0.0637	0.0735	0.0845	0.0964	0.1094	0.1234	0.1384	0.1544	0.1714
80	0.0336	0.0423	0.0519	0.0624	0.0734	0.0844	0.0954	0.1064	0.1174
90	0.0225	0.0348	0.0484	0.0634	0.0794	0.0964	0.1134	0.1304	0.1474
100	0.0355	0.0414	0.0504	0.0614	0.0734	0.0864	0.1004	0.1144	0.1284
110	0.0504	0.0549	0.0624	0.0724	0.0844	0.0974	0.1114	0.1254	0.1394
120	0.0675	0.0708	0.0764	0.0844	0.0944	0.1054	0.1164	0.1274	0.1384
130	0.0840	0.0863	0.0908	0.0974	0.1054	0.1144	0.1234	0.1324	0.1414
140	0.0994	0.0998	0.1028	0.1074	0.1134	0.1194	0.1254	0.1314	0.1364
150	0.1098	0.1106	0.1129	0.1164	0.1204	0.1244	0.1284	0.1324	0.1364
160	0.1181	0.1184	0.1194	0.1209	0.1228	0.1248	0.1267	0.1286	0.1304
170	0.1230	0.1231	0.1237	0.1242	0.1247	0.1252	0.1257	0.1262	0.1267
180	0.1246	0.1246	0.1246	0.1246	0.1246	0.1246	0.1246	0.1246	0.1246

U≈410kV
ALPHA EQUALS 0.80

0	10	20	30	40	50	60	70	80	90
0	1.0000	1.0000	1.0000	1.0000	1.0000	1.0000	1.0000	1.0000	1.0000
10	0.9354	0.9363	0.9388	0.9427	0.9474	0.9525	0.9572	0.9611	0.9645
20	0.7678	0.7706	0.7793	0.7930	0.8122	0.8364	0.8654	0.8991	0.9374
30	0.5554	0.5620	0.5790	0.6025	0.6315	0.6645	0.7014	0.7424	0.7884
40	0.3596	0.3670	0.3854	0.4113	0.4414	0.4744	0.5114	0.5524	0.5974
50	0.2093	0.2176	0.2314	0.2504	0.2734	0.3004	0.3314	0.3664	0.4054
60	0.1119	0.1202	0.1294	0.1394	0.1504	0.1624	0.1754	0.1894	0.2044
70	0.0594	0.0659	0.0734	0.0814	0.0904	0.1004	0.1104	0.1204	0.1304
80	0.0353	0.0417	0.0484	0.0554	0.0624	0.0694	0.0764	0.0834	0.0894
90	0.0305	0.0357	0.0414	0.0474	0.0534	0.0594	0.0654	0.0714	0.0764
100	0.0333	0.0393	0.0454	0.0514	0.0574	0.0634	0.0694	0.0754	0.0804
110	0.0443	0.0473	0.0509	0.0549	0.0584	0.0624	0.0664	0.0704	0.0744
120	0.0542	0.0563	0.0594	0.0624	0.0654	0.0684	0.0714	0.0744	0.0774
130	0.0634	0.0649	0.0664	0.0679	0.0694	0.0704	0.0714	0.0724	0.0734
140	0.0712	0.0721	0.0729	0.0734	0.0739	0.0744	0.0749	0.0754	0.0759
150	0.0773	0.0778	0.0784	0.0789	0.0794	0.0799	0.0804	0.0809	0.0814
160	0.0815	0.0818	0.0824	0.0829	0.0834	0.0839	0.0844	0.0849	0.0854
170	0.0841	0.0841	0.0841	0.0841	0.0841	0.0841	0.0841	0.0841	0.0841
180	0.0849	0.0849	0.0849	0.0849	0.0849	0.0849	0.0849	0.0849	0.0849

TABLE 3.6 (cont'd)

U \approx 512kV
ALPHA EQUALS 1.00

0	10	20	30	40	50	60	70	80	90
0	1.0000	1.0000	1.0000	1.0000	1.0000	1.0000	1.0000	1.0000	1.0000
10	0.9271	0.9304	0.9343	0.9390	0.9440	0.9487	0.9525	0.9550	0.9559
20	0.7422	0.7452	0.7487	0.7527	0.7568	0.7608	0.7648	0.7684	0.7712
30	0.5198	0.5249	0.5306	0.5366	0.5424	0.5484	0.5542	0.5597	0.5650
40	0.3341	0.3398	0.3459	0.3524	0.3592	0.3664	0.3738	0.3814	0.3891
50	0.1912	0.2115	0.2428	0.2811	0.3218	0.3661	0.4117	0.4588	0.5040
60	0.0968	0.1248	0.1543	0.1904	0.2292	0.2654	0.2950	0.3210	0.3418
70	0.0543	0.0770	0.1028	0.1344	0.1680	0.1996	0.2254	0.2422	0.2481
80	0.0356	0.0543	0.0754	0.1014	0.1291	0.1550	0.1762	0.1900	0.1948
90	0.0313	0.0459	0.0625	0.0829	0.1046	0.1250	0.1416	0.1525	0.1563
100	0.0338	0.0448	0.0574	0.0728	0.0892	0.1046	0.1172	0.1254	0.1282
110	0.0370	0.0471	0.0567	0.0674	0.0794	0.0906	0.0997	0.1057	0.1078
120	0.0448	0.0504	0.0568	0.0646	0.0730	0.0808	0.0872	0.0914	0.0928
130	0.0500	0.0538	0.0580	0.0632	0.0687	0.0739	0.0781	0.0809	0.0818
140	0.0544	0.0567	0.0592	0.0624	0.0658	0.0690	0.0716	0.0733	0.0739
150	0.0577	0.0589	0.0603	0.0620	0.0639	0.0656	0.0670	0.0680	0.0683
160	0.0599	0.0601	0.0611	0.0627	0.0640	0.0653	0.0664	0.0670	0.0674
170	0.0613	0.0614	0.0616	0.0618	0.0620	0.0621	0.0623	0.0624	0.0624
180	0.0617	0.0617	0.0617	0.0617	0.0617	0.0617	0.0617	0.0617	0.0617

U \approx 768kV
ALPHA EQUALS 1.50

0	10	20	30	40	50	60	70	80	90
0	1.0000	1.0000	1.0000	1.0000	1.0000	1.0000	1.0000	1.0000	1.0000
10	0.9067	0.9100	0.9137	0.9183	0.9232	0.9278	0.9316	0.9349	0.9374
20	0.6839	0.6944	0.7064	0.7212	0.7368	0.7515	0.7635	0.7714	0.7741
30	0.4427	0.4596	0.4788	0.5023	0.5274	0.5509	0.5701	0.5827	0.5870
40	0.2565	0.2761	0.2984	0.3257	0.3548	0.3822	0.4045	0.4241	0.4410
50	0.1399	0.1588	0.1804	0.2068	0.2349	0.2613	0.2829	0.2970	0.3018
60	0.0766	0.0930	0.1116	0.1345	0.1588	0.1816	0.2002	0.2124	0.2166
70	0.0462	0.0593	0.0743	0.0927	0.1122	0.1306	0.1456	0.1587	0.1687
80	0.0332	0.0433	0.0548	0.0689	0.0839	0.0980	0.1095	0.1170	0.1196
90	0.0288	0.0363	0.0448	0.0552	0.0664	0.0768	0.0853	0.0909	0.0928
100	0.0281	0.0335	0.0396	0.0472	0.0552	0.0627	0.0688	0.0728	0.0742
110	0.0289	0.0326	0.0369	0.0422	0.0478	0.0531	0.0574	0.0602	0.0611
120	0.0300	0.0325	0.0354	0.0390	0.0428	0.0464	0.0493	0.0512	0.0518
130	0.0310	0.0327	0.0345	0.0369	0.0393	0.0416	0.0435	0.0447	0.0451
140	0.0319	0.0329	0.0340	0.0354	0.0369	0.0382	0.0394	0.0401	0.0404
150	0.0326	0.0330	0.0336	0.0344	0.0352	0.0359	0.0365	0.0369	0.0370
160	0.0329	0.0331	0.0334	0.0337	0.0340	0.0344	0.0346	0.0348	0.0349
170	0.0331	0.0332	0.0333	0.0333	0.0334	0.0335	0.0336	0.0336	0.0336
180	0.0332	0.0332	0.0332	0.0332	0.0332	0.0332	0.0332	0.0332	0.0332

U \approx 1.02MV
ALPHA EQUALS 2.00

0	10	20	30	40	50	60	70	80	90
0	1.0000	1.0000	1.0000	1.0000	1.0000	1.0000	1.0000	1.0000	1.0000
10	0.8870	0.8902	0.8939	0.8984	0.9031	0.9076	0.9113	0.9137	0.9145
20	0.6321	0.6418	0.6529	0.6664	0.6807	0.6944	0.7055	0.7127	0.7152
30	0.3818	0.3962	0.4125	0.4325	0.4538	0.4748	0.4901	0.5008	0.5045
40	0.2091	0.2244	0.2418	0.2631	0.2858	0.3071	0.3245	0.3358	0.3397
50	0.1115	0.1252	0.1406	0.1596	0.1799	0.1989	0.2144	0.2245	0.2280
60	0.0653	0.0735	0.0839	0.1012	0.1175	0.1328	0.1453	0.1534	0.1542
70	0.0395	0.0478	0.0573	0.0689	0.0812	0.0948	0.1085	0.1106	0.1106
80	0.0292	0.0353	0.0422	0.0507	0.0597	0.0682	0.0751	0.0796	0.0812
90	0.0258	0.0290	0.0340	0.0400	0.0464	0.0525	0.0574	0.0606	0.0617
100	0.0227	0.0258	0.0292	0.0334	0.0379	0.0421	0.0456	0.0478	0.0486
110	0.0219	0.0224	0.0233	0.0243	0.0252	0.0261	0.0268	0.0270	0.0270
120	0.0218	0.0218	0.0224	0.0226	0.0230	0.0234	0.0238	0.0238	0.0238
130	0.0215	0.0215	0.0221	0.0223	0.0226	0.0228	0.0228	0.0228	0.0228
140	0.0211	0.0211	0.0216	0.0219	0.0223	0.0226	0.0227	0.0227	0.0227
150	0.0210	0.0210	0.0212	0.0214	0.0216	0.0217	0.0218	0.0218	0.0218
160	0.0209	0.0209	0.0211	0.0213	0.0215	0.0216	0.0216	0.0216	0.0216
170	0.0208	0.0208	0.0210	0.0211	0.0212	0.0212	0.0212	0.0212	0.0212
180	0.0208	0.0208	0.0208	0.0208	0.0208	0.0208	0.0208	0.0208	0.0208

FOR IF-4N 510F

TABLE 3.7 Scatter coefficient for single electron, and unpolarized X-ray, up to the coefficient e^4/m^2c^2 .

	ALPHA EQUALS 0.01		ALPHA EQUALS 0.40		ALPHA EQUALS 1.00	
	0	1.0000	0	1.0000	0	1.0000
10	0.9845		10	0.9672	10	0.9415
20	0.9398		20	0.8768	20	0.7913
30	0.8715		30	0.7493	30	0.6055
40	0.7879		40	0.6097	40	0.4341
50	0.6991		50	0.4793	50	0.3014
60	0.6157		60	0.3713	60	0.2099
70	0.5476		70	0.2907	70	0.1512
80	0.5025		80	0.2361	80	0.1152
90	0.4853		90	0.2030	90	0.0938
100	0.4974		100	0.1860	100	0.0810
110	0.5367		110	0.1797	110	0.0734
120	0.5978		120	0.1801	120	0.0688
130	0.6730		130	0.1839	130	0.0659
140	0.7530		140	0.1891	140	0.0641
150	0.8280		150	0.1942	150	0.0630
160	0.8890		160	0.1984	160	0.0623
170	0.9287		170	0.2010	170	0.0619
180	0.9425		180	0.2020	180	0.0617

ALPHA EQUALS 0.10		ALPHA EQUALS 0.60		ALPHA EQUALS 1.50	
0	1.0000	0	1.0000	0	1.0000
10	0.9804	10	0.9585	10	0.9208
20	0.9247	20	0.8468	20	0.7290
30	0.8408	30	0.6962	30	0.5149
40	0.7405	40	0.5408	40	0.3403
50	0.6365	50	0.4052	50	0.2209
60	0.5409	60	0.3002	60	0.1466
70	0.4630	70	0.2264	70	0.1024
80	0.4084	80	0.1785	80	0.0764
90	0.3791	90	0.1495	90	0.0608
100	0.3736	100	0.1335	100	0.0512
110	0.3882	110	0.1255	110	0.0450
120	0.4174	120	0.1222	120	0.0409
130	0.4551	130	0.1215	130	0.0381
140	0.4952	140	0.1220	140	0.0361
150	0.5325	150	0.1239	150	0.0348
160	0.5624	160	0.1238	160	0.0339
170	0.5817	170	0.1244	170	0.0334
180	0.5883	180	0.1246	180	0.0332

ALPHA EQUALS 0.20		ALPHA EQUALS 0.80		ALPHA EQUALS 2.00	
0	1.0000	0	1.0000	0	1.0000
10	0.9760	10	0.9499	10	0.9007
20	0.9083	20	0.8184	20	0.6737
30	0.8086	30	0.6485	30	0.4431
40	0.6924	40	0.4830	40	0.2744
50	0.5764	50	0.3474	50	0.1698
60	0.4730	60	0.2486	60	0.1094
70	0.3907	70	0.1826	70	0.0751
80	0.3329	80	0.1411	80	0.0552
90	0.2990	90	0.1162	90	0.0432
100	0.2855	100	0.1019	100	0.0357
110	0.2876	110	0.0936	110	0.0307
120	0.3002	120	0.0894	120	0.0273
130	0.3186	130	0.0871	130	0.0250
140	0.3488	140	0.0859	140	0.0233
150	0.3575	150	0.0853	150	0.0221
160	0.3724	160	0.0851	160	0.0214
170	0.3820	170	0.0849	170	0.0209
180	0.3853	180	0.0849	180	0.0208

TABLE 3.8 Total scatter coefficient of X-ray up to a^2c^2

ALPHA EQUALS 0.01	1.3382
ALPHA EQUALS 0.10	1.1217
ALPHA EQUALS 0.20	0.9826
ALPHA EQUALS 0.40	0.8090
ALPHA EQUALS 0.60	0.7028
ALPHA EQUALS 0.80	0.6292
ALPHA EQUALS 1.00	0.5743
ALPHA EQUALS 1.50	0.4804
ALPHA EQUALS 2.00	0.4188

FORTAN STOP

(which will mainly generate noise) is rather complicated and in itself contains much uncertainties (many approximations). Some approaches to describe the quality of scattered radiation is discussed in Section 4.2.

3.4 Measurement of X-rays

Measurement of X-rays is limited in several ways. Perfect measurement would imply knowledge of X-ray energy, direction of propagation and polarization. However in most applications the X-ray detector notes the occurrence of an X-ray and in some special situation estimates energy content. Measurement of direction and polarization requires additional devices. In practice additional uncertainty arises because not all X-rays are detected and several mechanisms distort estimates.

Since our current investigation is concerned with high speed (real time) data acquisition and processing we discuss only detectors with electronic output. Regardless of the particular technology utilized the block diagram of Figure 3.10 can be used to describe most detectors - such as a Photomultiplier, Proportional counter Scintillation detector or other device.

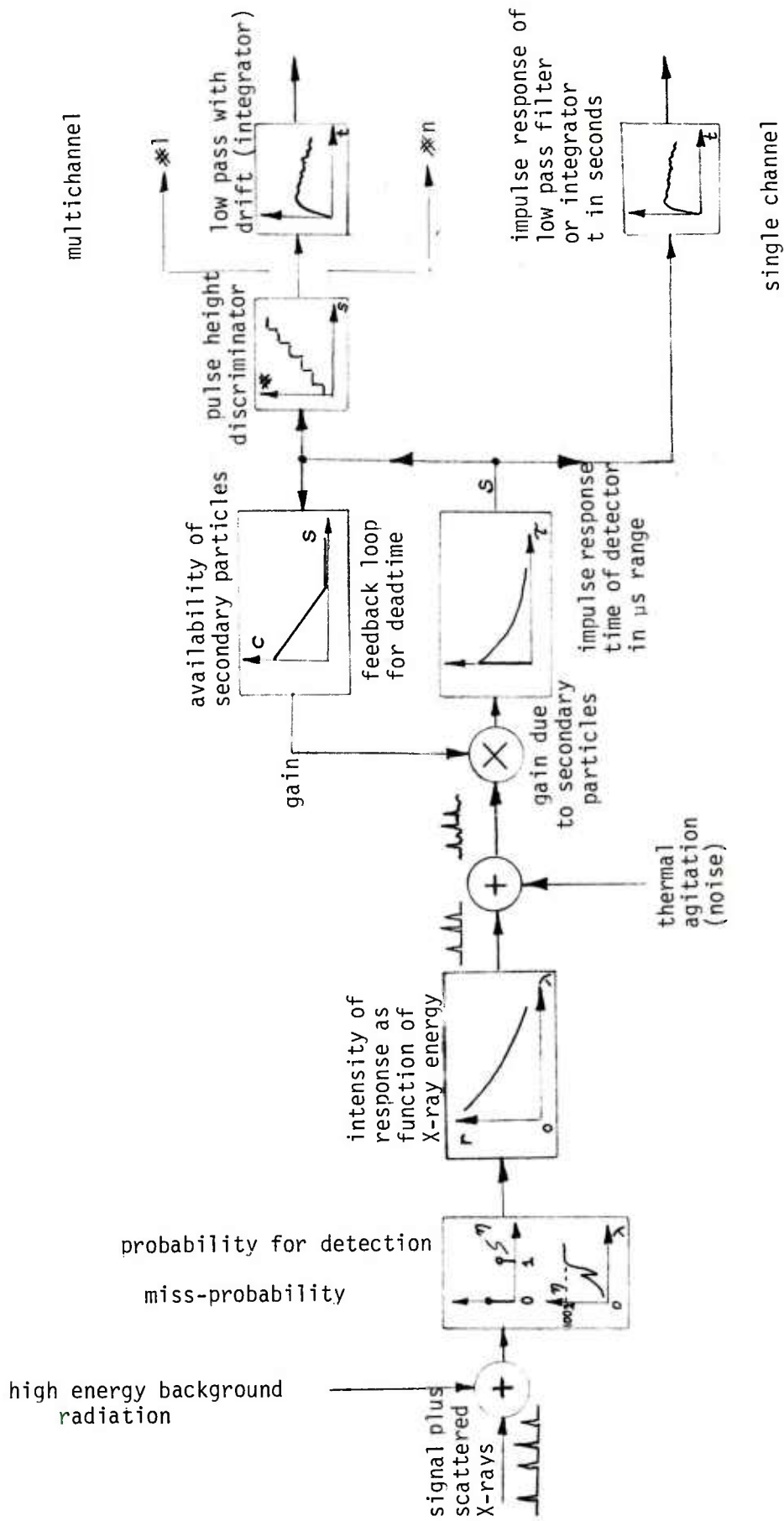


Figure 3.10: Schematic of model for X-ray detection process; see text for discussion

Following this schematic we will discuss the effects of the individual components.

1. The first component in the schematic expresses an energy dependent response probability for X-rays. Thus, given an X-ray has passed the detector a response of strength E will occur with probability $\eta(E)$. Typical values for η with $E \sim 60\text{keV}$ are between 30% for (Xe - pressurized system by GE and 100% for NaI(Tl) scintillation detector. For fixed geometry there is a strong dependency of η on E , as shown in Figure 3.10. One way to increase efficiency η is to increase the size of the detector and (pressure in case of a gas detector). Note, that in some instances the conversion of X-ray photon energy into signal can occur in stages (e.g. by diminishing X-ray energy in two stages) leading to an "escape peak" in photon statistics [Reference 22]. In some situations the secondary response can be suppressed.
2. The actual conversion of X-ray photon energy into another form of energy may exhibit a nonlinear relationship (Figure 8, p3-3 of [Reference 22])
3. Often a conversion of X-rays into another form of energy is associated with a change of the number of "particles" such as photons, ions, or electrons representing the original X-ray. Often the relation is not given by a fixed ratio x ; instead the number of generated particles x follow some probability law and this adds noise. When however $E[x] \gg 1$ the noise of the total detector, will be nearly that of quantum mottle only [Appendix A3.3].
4. Thermal agitation occurs in many detectors. Its presence and the presence of the background radiation are the motivation to

take measurements over short time intervals so as to avoid their cumulative effect. In detector arrays where analog-to-digital conversion requires a significant amount of time those detectors with the weakest signal should be measured first - as is done in the GE-8800 where the detectors in the center are sampled first. The thermal agitation (flicker and Johnson noise) manifests itself as a drift of the signal.

5. Conversion of X-ray energy into some other form of energy is often associated with dynamics which lead to a refractory time. Thus, during this time another X-ray photon induces either no or a reduced response. The result is an apparent nonlinear relationship between photon flux and signal. Good detectors have a refractory period in the μ -sec range. We remark that an approximation to this nonlinear behavior (superposition principle fails) could be done in terms of Wiener kernels $h_n(\tau_1, \tau_2 \dots \tau_n)$. The total system response would be approximated by a truncated expansion [Reference 29]

$$S_g(t) = \sum_{i=0}^n \underbrace{\int \int \dots \int}_{i \text{ times}} h_i(\tau) S_x(t-\tau_1) S_x(t-\tau_2) \dots S_x(t-\tau_n) d\tau \quad (3.32)$$

where S_x represents the train of incident X-rays and S_g the output signal.

Truncation of the expansion would here be determined by the probability of more than n events falling within the refractory period.

A few more words should be said about the possibility of the detector to resolve energy E of X-ray quanta. As mentioned a number of secondary "particles" may be released by incident

X-ray photon. Let us assume this number n_{sec} is proportional to $E = h\nu$. As shown in the Appendix A3.5 this number n_{sec} determines spectral resolution $\Delta\nu$ ($\pm 2\sigma$ - channel width)

$$\Delta\nu = 4\nu n_{\text{sec}}^{-1/2} \quad (3.33)$$

Hence, from data in [Section 3-11 of Reference 22] for $n_{\text{sec}} = 250 \times .2 = 50$, when Na I(Tl) @ 8keV is used, a relative bandwidth of $\frac{\Delta\nu}{\nu} = 55\%$ is with 48% [Section 3-29, Reference 22] of comparable magnitude.

This statement does however not imply that estimation of the X-ray spectrum is limited to this value. The statement concerns only the blurr with which the spectrum is seen by the detector and "de-blurring" is possible by deconvolution. However, what is gained in resolution in terms of ν is lost in terms of accuracy of $I(\nu)$ - no information can be gained by "deblurring".

From these considerations it becomes clear that information acquisition about $I(\nu)$ is limited by the spectral resolution of the detector. Since most of the energy in tube generated X-rays and those emanating from an object (including the scattered radiation) lie within a factor of 2 (corresponding to ≈ 3 channels) it appears that spectral estimation will not bring very valuable information for void and crack like flaw detection.

In case of a monochromatic spectrum from a radioactive source some improvement of signal to noise ratio seems possible. Recall the effect of Compton scatter of Equation 3.27 and assume on isotope source with about 1.2 MeV. A 25% channel width translates into the selection of a scattering angle of

26°. When multiple scattering is of significance, such as in almost any material of a few centimeter width some improvement of estimation of spatial properties of an object may be possible. Note that detector materials other than Na I(Tl) (possible CsI(Na), [Reference 39]) have to be used for this purpose. At least, however, by use of energy selective channels, one can discriminate against omni-present high energy background radiation which could manifest itself as large noise otherwise.

4. STRUCTURAL MODELING

In this section we investigate the possibilities to model the performance of an X-ray flaw detection scheme. There is a tremendous freedom to the possibilities of design for the range of different materials. No closed form approach as in the previous sections is possible. Instead, some approaches, some general concepts and possibilities are presented.

For the purpose of flaw detection a separation into three major areas is useful. First we address the possibilities of modeling objects in order to use prior information about them. Next we consider the possibilities to model the projection process in the presence of quantum mottle and scatter for several beam geometries. Finally we analyze signal-to-noise ratio and how it may be optimized.

4.1 Modeling of Object

The main purpose of modeling the object is to find what projection one has to expect from a scan e.g. it is desired to model the mean for any particular scan. This problem is considerably simpler than the inversion problem. If a good job can be done on this part much of the computational effort associated with image reconstruction can be avoided. It might even be possible to obtain performance superior to CT as far as flaw detection and location is concerned because the projection problem may be solved incorporating more of the physical phenomena.

A planar object may be described by its density $n(x,y)$. This density may be factored into the product $n(x,y)=n_0(x,y) n_1(x,y) n_2(x,y)$. Here n_0 represents the shape and average density of the object, n_1 the random density variation due to variation in chemical composition and micropores, and n_2 the 0-1 function representing voids of area ϵ or cracks of length Δ and width δ .

The component $n_0(x,y)$ calls for some more discussion. For example, machined holes may be shifted or weavings may be distorted locally leading to kinks and bows (Figure 4.1). In this situation, as far as prior information is concerned one has usually an idea about the number of holes in an object and also the number and extent of permissible kinks and bows. Such location errors could easily be estimated from projections - provided they are few and do not belong to unobservable patterns. In some objects there may also be a systematic change of density with location - for example material density in a round object may increase towards the surface. For the modeling of these density variations of material low order polynomials or, when a large number of objects for training are available, Karhunen - Loeve expansion might be used [Reference 13]. In any event it appears that the projections of these deviations could easily be modeled, e.g. by low order polynomials or simple patterns. We give now some examples how this might be done.

Consider first a radial density variation of a solid cylinder. For example a simple radial density variation of a cross section orthogonal to the axis could be given by

$$n_0(x,y) = 1 + \begin{bmatrix} x \\ y \end{bmatrix}^T \begin{bmatrix} c & 0 \\ 0 & c \end{bmatrix} \begin{bmatrix} x \\ y \end{bmatrix}, \quad x^2 + y^2 < r^2. \quad (4.1)$$

A more complicated relationship would be

$$n'_0(x,y) = 1 + f \left\{ \begin{bmatrix} x \\ y \end{bmatrix}^T \begin{bmatrix} 1 & 0 \\ 0 & 1 \end{bmatrix} \begin{bmatrix} x \\ y \end{bmatrix} \right\} \quad (4.2)$$

where $f(\cdot)$ is some suitable polynomial. This polynomial may however contain some variations in its coefficients from one cylinder to the next. The affect of these variations on the projections are easily computed - at least when no scatter is present. This will permit one to select some set of polynomials - possibly of the Pade

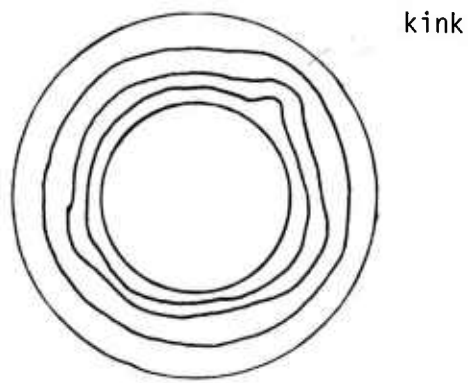


Figure 4.1: Deviation of density $n_0(x,y)$ from ideal density due to kink of matrix.

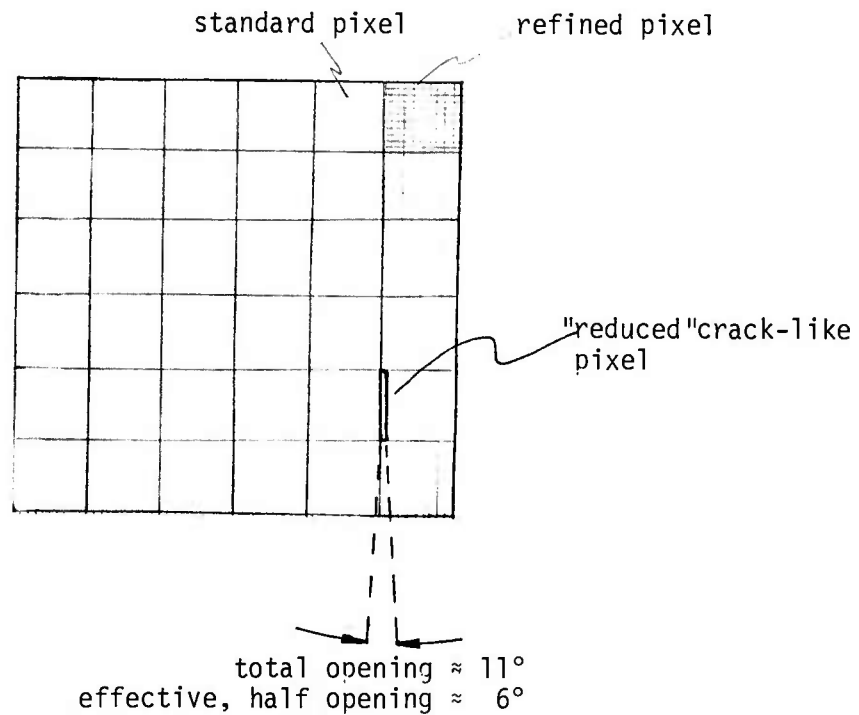


Figure 4.2: Crack-like pixel with effective opening angle of about 6° . These slender pixels have, conceptually, to point to the detector array.

type - which in a few parameters (coefficients) give good approximations for the range of possible projections. These few coefficients are then estimated for each scan individually by weighted (depending on quantum mottle) least squares from the raw projection data \underline{b}' . The numerical efforts for doing this are usually small. Then the resultant polynomial is subtracted from \underline{b}' and the difference would provide the input \underline{b} for the estimation procedures discussed in Section 2.3. We remark, that adjusting for deviation of locations of holes (misalignment) is also easily treated by least squares.

Some care has to be taken though for several reasons. First, the distribution of the quadratic forms in Section 2 will be changed. Typically $E(Q)$ and $E(Q')$ (and similarly their variance) will be decreased by an amount proportional to the number of coefficients used in the polynomial representation. This has to be considered in the development of the flaw detection algorithm.

Second, the number of these coefficients should be kept small. Several methods exist to perform a data dependent selection of a good number of coefficients. Among the most prominent are Akaike's [Reference 2] AIC and Schwarz's [Reference 39] asymptotic Bayes approach.

Third, these polynomials should not be able to remove the effect of flaws, at least not for all scans considered. The problem is closely related to signal transmission through bandpass filters. Statistical concepts [Reference 45] are again very useful to study this. Here, no particular problem is anticipated, since cracks and voids have a rather distinct character from other material density variations such as kinks, bows and low order polynomials.

A few more remarks should be made about the random density variations $n(x,y)$ of an object. Usually there will be a region over which the density variation takes place. In other words points very

closely together will show typically a positive correlation of their densities while farther apart the correlation will diminish.

When pixels of the size of these regions are chosen they may be regarded as uncorrelated and hence justify the models discussed in Section 2.3. As far as the variance σ_a^2 of the absorption of these pixels is concerned - it is proportional to the area Δ^2 (volume) of the individual n^2 pixels. However, as far as the value σ_a relative to the mean absorption μ_a is concerned it is inversely proportional to Δ , e.g.

$$\frac{\sigma_a}{\mu_a} \propto \frac{1}{\Delta} \propto n \quad (4.3)$$

From the results in Section 2.3 it becomes clear that best void detection is accomplished when the size of a pixel coincides precisely with the size of a void. This is a pleasing result since it allows to optimize performance for a given size of voids. In a sense this result may also be viewed as a primitive form of modeling, and as is usually the case, modelling improves performance in signal detection.

This observation suggest also another aspect: could it be useful to use pixels shaped like cracks (of unknown orientation) or possible a series of cracks? Without going into details of the argumentation - the advantage of doing so can only be fully realized when scans could accumulate information over all projections (range $\pi/2$) of the crack before arriving at a decision.

For the example given and with the use of a sequential probability ratio test ($\epsilon = 10\%$ for a rectangular pixel in Section 2.3.4), an array of 10 times finer pixels (Figure 4.2) (- which is only meaningful with correspondingly finer detectors -) and ten of these fine pixels stacked to model a crack would give a value $(\epsilon'/\sigma)^2$ ten times as large than in Equation 2.90. This would cut the number of necessary scans (prior to a

decision) to about 15. By coincidence, for two orthogonal projection directions, 15 scans, and an assumed angular opening of the crack model (Figure 4.2) of $\theta = \sin^{-1}(.1) \approx 5.74^\circ \approx 6^\circ$, 15 steps with rotational increment θ take it (almost over a full 90° rotation; this allows averaging of the information prior to a decision. Thus, it appears such single cracks could reliably be detected with relatively few scans. For an object of some 50cm x 50cm size single cracks as fine as .5mm in a material with 2% density variation over 5mm x 5mm areas (and $\sigma_{\text{mottle}}^2 = 100 \sigma_a^2$) could be detectable (the width of detectors has to be .5mm or less). This result is still much stronger than the detection probability if the crack is seen only edge on. Nevertheless, it appears that most of the information regarding the existence of the crack is due to those few views(only) which see the crack nearly edge on. From this consideration simplified detection schemes could be constructed.

4.2 Modeling Projection

There are at least three important aspects of estimating the line integrals of Equation 2.1 which represent the projection of an object. First, there is a bias when exponentiation of the ratio of incident of existing radiation is used. It is simply a result of quantum mottle. Second, X-ray spectra, with the exception of those arising from certain radioactive isotopes, are polychromatic. Different spectral components are however absorbed differently (see Section 3.2). The effect of an increased fraction of high energy X-rays in the spectrum behind the object is regarded as beam hardening. This leads to a further deviation from the exponential attenuation of X-ray intensity with path length. Third, scattering changes the mean and variance of the X-ray intensity measured by the detector.

Regarding the compensation of the bias introduced in estimation of line integrals a first order correction was suggested in Equation 2.29.

Somewhat more difficult is the compensation for polychromaticity. One way to approach modeling the bias is to consider limiting situations. For example for a thick object ($\ell \rightarrow \infty$) only the hardest X-rays will penetrate and they may be approximated as a monochromatic beam. For thin objects, the hard components will pass unaffected while only the soft X-rays will be attenuated by the object. This suggests to use in practice a polynomial fraction of the form

$$b = \frac{\alpha_1 u + \alpha_2 u^2 + \dots + \alpha_n u^n}{\beta_0 + \beta_1 u + \dots + \beta_n u^n} \cdot \frac{1}{\mu \rho} \quad (4.4)$$

$$u = -\ln(r)$$

where $\mu \rho$ is the absorption per unit path length and $r \leq 1$ is the ratio of measured to incident X-ray intensity. Thus for $\frac{I}{I_0} \rightarrow 1$ (no object) $b \rightarrow 0$ and for $r \rightarrow \infty$, $b = (\mu \rho)^{-1} \cdot \ln(r)$. The necessary order of expansion may be studied from the properties of Equations 3.5 and 3.17 by numerical techniques. The final choice of the coefficients α_i and β_i would depend on the characteristics of the X-ray spectrum and might be adjusted by regression or some nonlinear parameter estimation technique, [Reference 4].

For example for p scans and n measurements per scan a total of pn measurements should be fit by relation Equation 4.4. For this purpose form the weighted squares cost function

$$\sum_{i=1}^{pn} \frac{\left(b_i - \frac{\alpha_1 u_i + \dots + \alpha_n u_i^n}{\beta_0 + \dots + \beta_n u_i^n} \right)^2}{v_i}$$

and minimize it with respect to α_j and β_k . Here v_i are the variance of measurements b_i composed of quantum mottle and material density variations.

When also the bias due to low photon count has to be compensated the approach of replacing $u = -\ln(r)$ by $u = -\ln(r) + 1/I$ as suggested in Equation 2.29 would be useful.

Finally scatter has to be considered. We may assume that scatter has a low spatial frequency [Reference 43] and may thus be described by an additional Poisson distribution, incident on the detector i . The parameter $\lambda(i)$ is a slow function of i - possible a low order polynomial. Again we may remove this scatter component by weighted least squares directly from the measurements of the I_i . Care has to be taken here because measurements (photon counts) have to be positive numbers. Nonlinear parameter estimation techniques are available to handle this. Closely related to this problem a second problem arises when the photon count from the primary beam is weak. Mainly the measurement correction for bias will have a large standard deviation relative to its mean complicating the series expansion of Equation 2.27 for the bias. However it seems that in extremes of such situations the measurement contains very little information and it may very well be omitted altogether. Of course the estimation scheme has to correct for the missing measurement - but this is easily accomplished (Note also the reduced observability).

Related to scatter let us investigate a few more interesting aspects of scanning especially its effect on the projection matrix A . The following three geometries of beams are interesting in this context: (i) the pencil beam; (ii) the fan beam - or as a simplified version a flat, sheet-like X-ray beam; and (iii) full exposure of an entire object.

The pencil beam may be viewed as an elementary unit. Other beams may (within limits) be composed of it. Assume for the moment the path of the pencil beam is described by a straight line and for simplicity assume a monochromatic X-ray source. In this case the intensity of the

primary beam as a function of the location of the point $P(x,0)$ (Figure 4.3) in a homogeneous object described by

$$I_p = I_0 e^{-\alpha(L-x)} \quad (4.6)$$

We may ask now what the intensity field of the scattered radiation looks like. A simple model for the intensity (neglecting end effects) as a function of the distance from the pencil beam, say at a point $P(x,y)$ is

$$I_{sc} = \tau I_p \frac{e^{-\alpha\sqrt{y^2 + z^2}}}{\sqrt{y^2 + z^2}} \quad (4.7)$$

Several questions can be approached with this model. Most important for us are: the intensity of the primary beam of the detector, the intensity due to the scattered beam at the detector, and the intensity of scattered radiation around the detector.

Clearly, the intensity of radiation due to the primary beam is $I_{p,det} = I_p(L) = I_0 \exp(-\alpha L)$. The intensity due to scatter requires integration. For this purpose find first the contribution \tilde{I} of a point $P(x,y,z)$ to what is received at the detector. From Figure 4.3

$$\begin{aligned} \tilde{I}_{sc} &= I_{sc}(x,y,z) \cdot \frac{1}{v^2} \exp(-\alpha u) \\ u &= x \sqrt{1 + \frac{y^2 + z^2}{(D-x)^2}} = x \sqrt{1 + \frac{r^2}{(D-x)^2}} \\ v &= (D-x) \sqrt{\sim} \end{aligned} \quad (4.8)$$

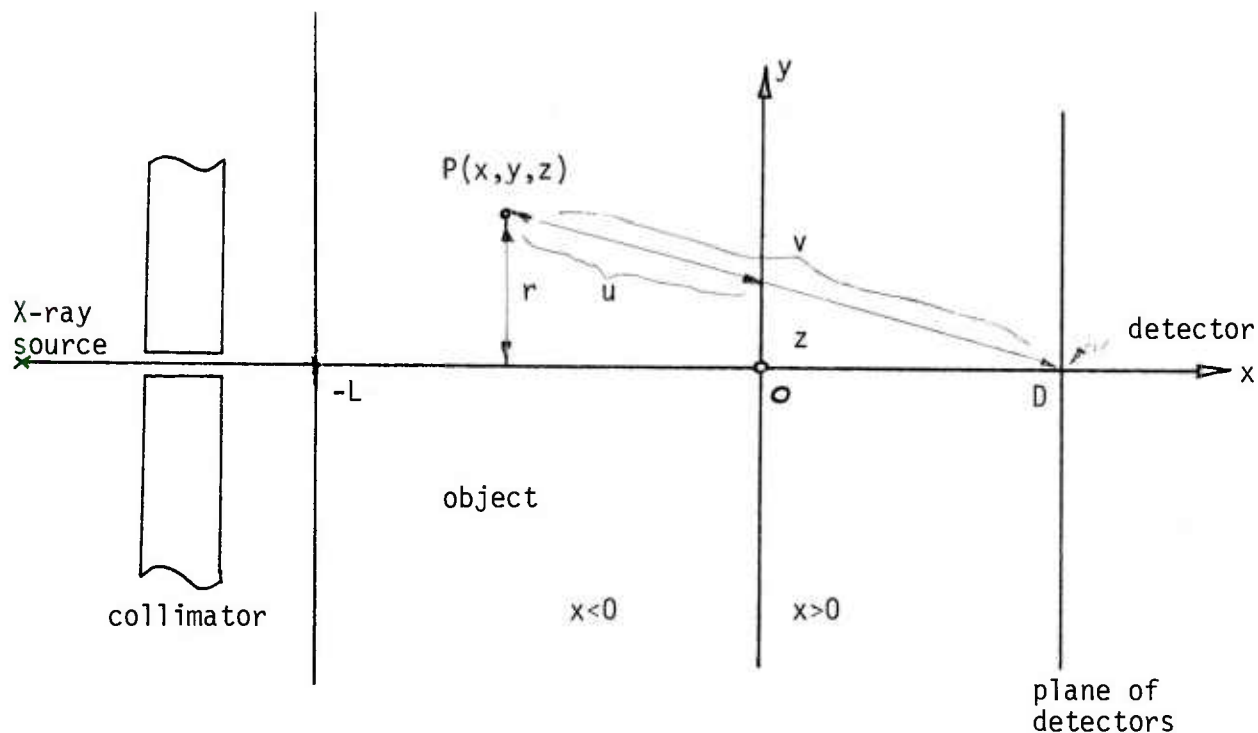


Figure 4.3: Geometry to find bound on intensity of scattered radiation at a given detector location.

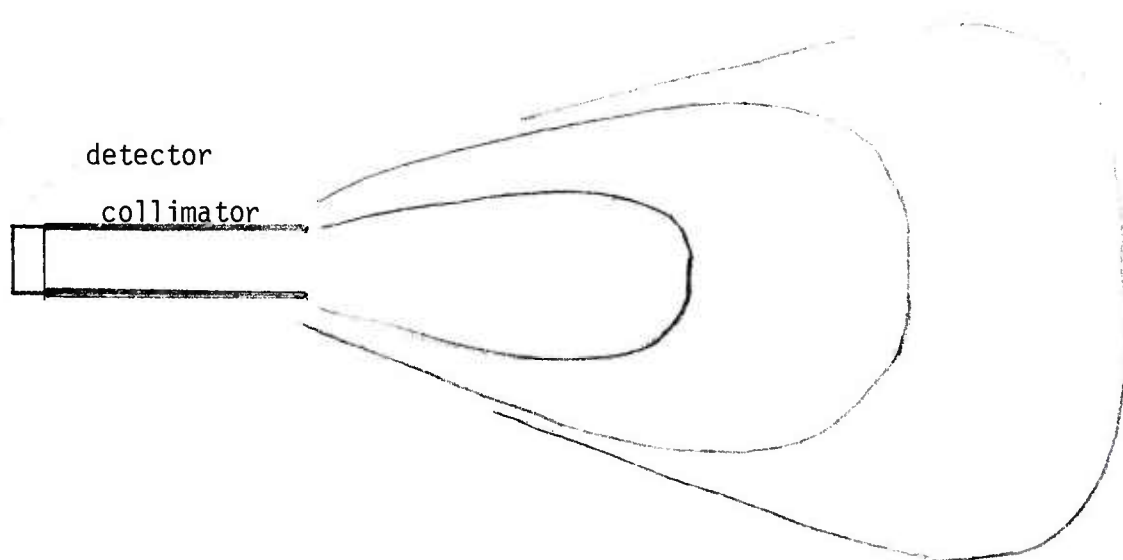


Figure 4.4: Schematic of receptive field in fan beam geometry. Note that a pencil beam geometry would yield a much narrower field.

and thus the total scattered intensity for the pencil beam

$$I_{sc, Det} = \int_0^L \int_0^\alpha I_0 e^{-\alpha(L-x)} \tau \frac{\exp[-\alpha r]}{r} \times \frac{1}{(D-x)^2 \left[1 + \frac{r^2}{(D-x)^2} \right]} \exp(-\alpha x \sqrt{1 + \frac{r^2}{(D-x)^2}}) \cdot 2 r dr dx \quad (4.9)$$

Explicit integration of this expression is not simple, but some approximations seem to be useful for certain cases. For example we may be interested in an approximation when $L \rightarrow \infty$. In this event the term $r^2/(D-x)^2$ may be neglected because with increasing r the scattered field intensity declines rapidly. With this approximation, mainly the farfield contribution is explained and one obtains after integration over r

$$I'_{sc, Det} \cong \int_0^L I_0 e^{-\alpha L} \cdot \frac{\tau}{\alpha} \cdot \frac{1}{(D-x)^2} dx$$

$$\cong \frac{I_0 \tau e^{-\alpha L}}{\alpha} \left[\frac{1}{D} - \frac{1}{D+L} \right] \quad (4.10)$$

Observe the ratio of primary to secondary beam intensity as $L \rightarrow \infty$ converges with $I_p = I_0 e^{-\alpha L}$ to

$$\frac{I_p}{I_{sc}} = \tau^{-1} \alpha D \quad (4.11)$$

Thus it appears that "signal-to-noise" ratio (aside from quantum mottle) remains above some minimal value for arbitrary large objects; conveniently it can be increased proportional to D . On the other hand, for $L \rightarrow 0$ scatter could be reduced proportional to D^{-2} . From geometric consideration it is clear that the approximation will only work for $D > \alpha^{-1}$.

Next let us consider a flat, sheet like X-ray beam, assuming all X-rays are parallel. For this case we can adopt Equation 4.7 for the scattered intensity by

$$I_{sc} = \tau I_p e^{-\alpha z} \quad (4.12)$$

and hence

$$I_{sc, Det} = \int_0^{-L} \int_{-\infty}^{+\infty} \int_{-\infty}^{+\infty} I_0 e^{-\alpha(L-x)} \tau e^{-\alpha z} \frac{1}{(D-x)^2 \left[1 + \frac{z^2 + y^2}{(D-x)^2}\right]} \cdot \exp \left[-\alpha x \sqrt{1 + \frac{z^2 + y^2}{(D-x)^2}} \right] dz dy dx \quad (4.13)$$

This time the contribution of the scattered radiation from a point $P(x, y, z)$ does not allow the approximation $u \approx L+x$. Only the contribution due to elevation z may be neglected since in this direction the radiating field declines rapidly.

Thus, as an approximation, integration over z (x, y fixed and at least one of them large compared to D and α^{-1}) gives only a factor α^{-1} .

Thus we obtain a 2 dimensional approximation for the intensity field and

$$I_{sc, Det} \approx \alpha^{-1} \int_0^{-L} \int_{-\infty}^{+\infty} I_0 e^{-\alpha(L-x)} \tau \frac{1}{(D-x)^2 \left[1 + \frac{y^2}{(D-x)^2}\right]} \cdot \exp \left[-\alpha x \sqrt{1 + \frac{y^2}{(D-x)^2}} \right] dy dx \quad (4.14)$$

As far as the behavior of this integral is concerned for $L \gg R \gg D$ one may study

$$I_1 = \int_R^L \int_{-\infty}^{+\infty} \frac{e^{-\alpha(\sqrt{u^2 + v^2} - u)}}{u^2 + v^2} du dv \quad (4.15)$$

where u corresponds to $\alpha(L-x)$ and v to αy . Considering a coordinate transform $u = r \cos \phi$, $v = r \sin \phi$ it is seen that this integral is related to

$$I_2 = \int_R^L \int_{-\pi}^{+\pi} \frac{e^{-\alpha r(1 - \cos \phi)}}{r} dr d\phi \quad (4.16)$$

This latter integral is bounded from below by $I_3 < I_2$ where

$$I_3 = \frac{1}{L\alpha} \int_{-\pi}^{+\pi} \frac{e^{-\alpha R(1-\cos \phi)} e^{-L(1-\cos \phi)}}{(1-\cos \phi)} d\phi \quad (4.17)$$

For large $L \gg R$ this integral has a singularity of the type

$$I_4 = \frac{1}{\alpha L} \int_{-\Psi}^{+\Psi} \frac{e^{-\alpha R\phi^2}}{\phi^2} d\phi, \Psi > 0 \quad (4.18)$$

This suggests that scatter intensity over a narrow angular range dominates the intensity of the parallel component of the primary beam. Fortunately for a narrow range ϕ scatter may not be so detrimental since this strong component will carry some spatial information - but it is virtually indistinguishable from the primary X-rays. Nevertheless for finite size object some "smearing out" of the field, over which the detector is sensitive, will occur (Figure 4.4). Knowledge of this field is important for the selection of adequate models of the matrices of the type shown in Equation 2.12.

When comparing the receptive fields for the pencil beam and the flat sheet parallel beam (or similarly fan beam) the latter will obviously yield much wider fields at some distance from the detector. While for the pencil beam the receptive field will not extend much over α^{-1} one might expect that of the flat parallel beam to extend over some angle 2Ψ , or, in other words to grow in width proportional to the distance from the detector. This suggests, for example, to examine an object from both sides when a fan beam is used.

Another important problem which arises in this context is the choice of the use of either a pencil beam or a flat parallel beam (or fan beam). Both have to be generated and approximated from point sources and collimation selects the beam shape. Thus the pencil beam will contain vastly fewer X-rays. For any given object the question arises which procedure would yield more information per unit time for the flaw

detection process. The importance of the term $(\epsilon/\sigma)^2$ and the discussion of the importance of matching pixel size to flaw size seem to be the major components for selecting one or the other method. In other words it appears to be most important to match receptive field width to flaw size when the variation of measurements is mainly due to material uncertainties (use pencil beam for small flaws).

It should be pointed out that here we neglected the use of a collimator which is a very useful means to narrow receptive fields (Section 4.34). Thus, by use of effective collimators the fan beam may in many cases provide superior acquisition of information, e.g. larger information rates. Some numerical studies seem to be necessary to decide about the best choice of the method for a particular problem setting (flaw size, object size, collimator properties, object material, attainable beam hardness and X-ray intensities)

From considerations similar to above discussion of scatter in flat parallel beam geometries it is clear that irradiation of a large volume rather than a slice (or a pencil) will yield still more severe scatter. Thus, limiting the primary X-ray beam to the region of interest (e.g. slice) is an important concept. Related to these concepts is also the importance never to have several X-ray sources operate simultaneously as the scatter produced by one will contribute to total scatter intensity. Instead one may operate different sources in a sequential, pulsed mode.

The discussions have pointed out the importance to describe receptive fields of detectors. This concept should replace the oversimplification of a modulation transfer function (MTF/ or point response function) when analyzing X-ray images. One of the consequences is of

course, in case of use of full scan CT, to give up on the idea of using a simple backprojection method as presented in Section 2.1. Instead appropriate weighting matrices should be used [see discussion of generalization of backprojection].

4.3 Basic Signal-to-Noise considerations

Some basic concepts which have to be considered in system designs are discussed now. There is no particular hierarchical structure to their importance - they have to be seen simultaneously for any NDE problem. For this reason the presentation in this section deviates from that of others. We will shortly expose each of the ideas.

4.3.1 Concept of optimal beams hardness

The problem addressed here is motivated in the following way. On the one hand consider an object through which "infinitely hard" X-rays are passed. Obviously no absorption would occur and it would not be possible to tell with any measurement device whether any flaw changed the flux of X-rays. On the other hand if one takes very soft X-rays none of them even arrives at a detector. Again one could not tell the presence of any flaw. Thus there must be intermediate values of beam hardness for which better results can be obtained - possible a single optimal hardness.

For derivation consider the following model

- a) monochromatic beam
- b) no scatter
- c) only quantum noise (Poisson) and independent measurement noise V
- d) small flaw

For the effect of a small flaw see schematic in Figure 4.5. Objective

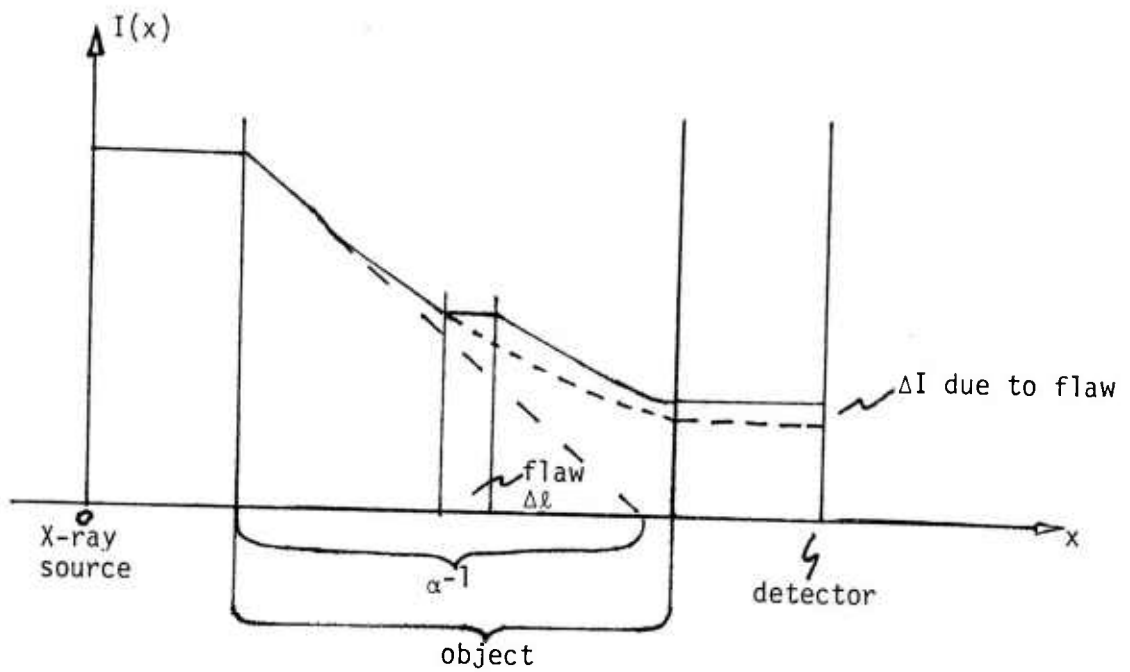


Figure 4.5: Effect of a small flaw on detector. Observe dependency of ΔI on α^{-1} .

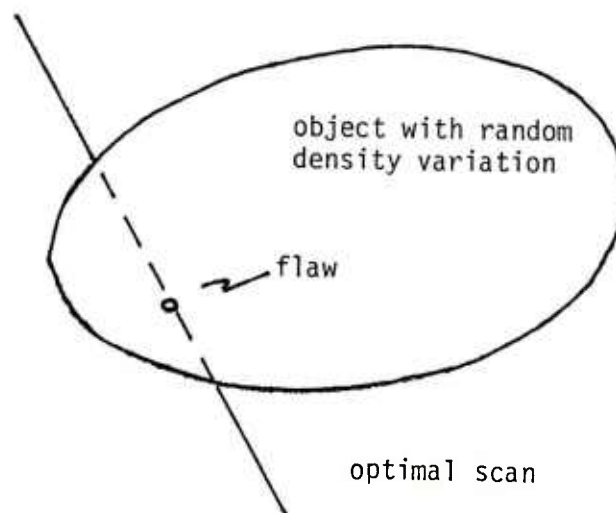


Figure 4.6: Choice of (single) optimal scan direction by choice of shortest path through object.

is to maximize the effect ΔN of the flaw on the output, versus $\sigma = \sqrt{\lambda}$, the uncertainty due to quantum noise

Solution:

$$\begin{aligned}\Delta N &= N_0 [e^{-\alpha(\ell-d)} - e^{-\alpha\ell}] \\ &= N_0 e^{-\alpha\ell} [e^{\alpha d} - 1] \\ \sigma^2 &= N + V = N_0 e^{-\alpha\ell} e^{\alpha d} + V\end{aligned}\tag{4.19}$$

for a small flaw $\alpha d \ll 1$ minimize $\sigma^2/(\Delta N)^2 = f(\alpha)$ w.r.t. α .

$$\begin{aligned}f(\alpha) &\cong \frac{N_0 e^{-\alpha\ell} + V}{N_0^2 e^{-2\alpha\ell} \cdot (\alpha d)^2} \\ &= \frac{1}{N_0} \left[e^{-\alpha\ell} (\alpha d)^{-2} + \frac{V}{N_0} e^{2\alpha\ell} (\alpha d)^{-2} \right]\end{aligned}\tag{4.20}$$

$$\begin{aligned}f'(\alpha) &= \frac{1}{N_0} \left[\ell e^{-\alpha\ell} (\alpha d)^{-2} - 2(\alpha d)^{-3} d e^{-\alpha\ell} \right] \\ &\quad + \frac{V}{N_0} \left[2\ell e^{2\alpha\ell} (\alpha d)^{-2} - 2(\alpha d)^{-3} d e^{2\alpha\ell} \right]\end{aligned}\tag{4.21}$$

Solution for extreme cases:

- 1) $V \gg N_0$ (small photon count relative to independent measurement noise)

then let $f'(\alpha) \rightarrow 0$

Result: $\alpha_{\text{opt}} = 1/\ell$. In other words beam hardness should be adjusted until a fraction e^{-1} of the incident N_0 X-rays exit.

- 2) $V \ll N_0$ (large photon count dominates independent measurement noise)

then let $f'(\alpha) \rightarrow 0$

Result: $\alpha_{\text{opt}} = 2/\ell$. Thus beam hardness should be adjusted until a fraction e^{-2} of the incident N_0 X-rays exit.

In summary, when V and N_0 are not well known one should choose beam hardness so that between 37% and 14% of the radiation are passed by the object to be tested.

4.3.2 Selection of best projection

Model: a) object with fixed random density ($\sigma_a^2 = \text{const}$)
 b) known location of possible flaw (Figure 4.6)
 c) no scatter
 d) measurement noise V
 e) quantum noise λ

The information obtained from a single projection from the presence of a flaw is characterised similar to Equation 4.20 by

$$\begin{aligned} f(\ell) &= \sigma^2/(\Delta N)^2 = (V + \ell\sigma_a^2 + N_0e^{-\alpha\ell})/(\Delta N)^2 \\ &= (\sigma_m^2 + \ell\sigma_a^2 + N_0e^{-\alpha\ell})/N_0^2e^{-2\alpha\ell} \cdot (\alpha d)^2 \end{aligned} \quad (4.22)$$

This function is monotonic increasing in ℓ and hence is minimized by minimizing ℓ . This is done by choosing the shortest path through an object.

4.3.3 The relation of Noise terms to multiscan

Model: a) constant random material density variation $\alpha_1(x,y)$ (Figure 4.7)
 b) monochromatic beam
 c) no scatter
 d) round void of known location

Nomenclature: $\alpha(x,y) = \alpha_0 + \alpha_1(x,y)$ absorption

$u(c_i)$...line integral along straight line c_i

N_{0i} ...incident photon count for scan i (index i sometimes omitted)

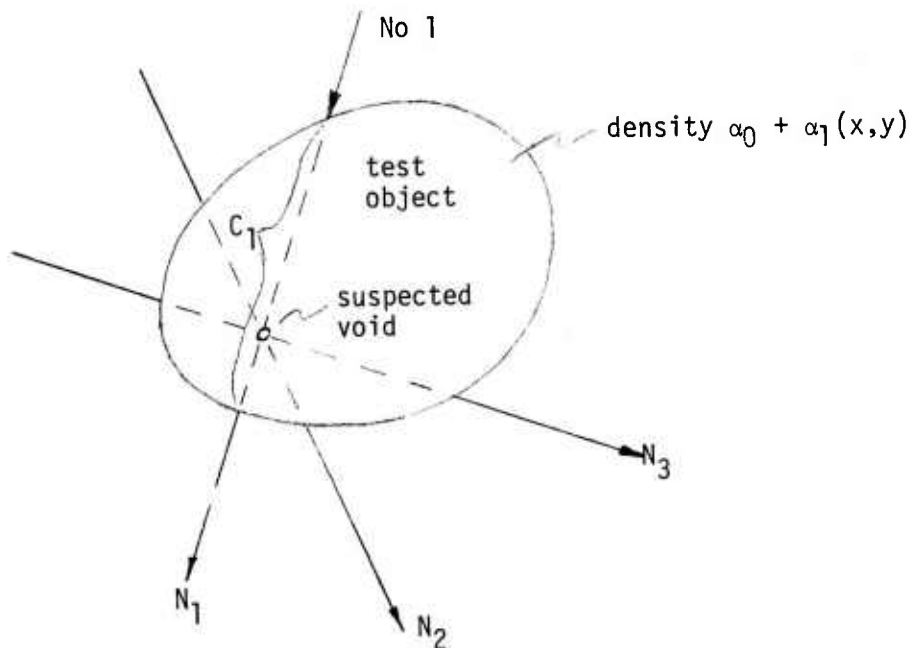


Figure 4.7: Use of multiple scan angles for flaw detection at a suspicious location.

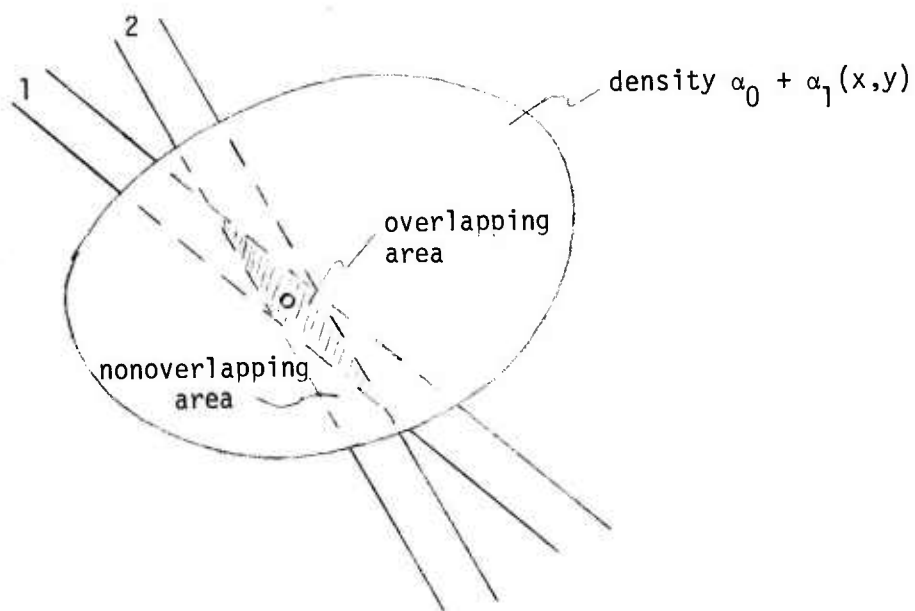


Figure 4.8: Simple model for finite width of receptive field of detector. Overlapping areas introduce correlation between measurements and degrade accuracy of estimation of size of void. See text for analysis.

N_i exiting photons for scan i

d_i size of flaw in projection i

Evaluation of noise due to material - σ_m^2 (corresponds to σ_b^2 in Section 2)

$$\sigma_m^2 = E[(N - \bar{N})^2] \quad (4.23)$$

$$\approx N_0^2 E \left\{ \left[\exp\left(-\int_{c_i} \alpha_1 ds - \alpha_0 \ell_i\right) - \exp(-\alpha_0 \ell) \right]^2 \right\}$$

This may be approximated (for short tailed distribution of $\int_{\Delta c} \alpha_1 ds$) by

$$\sigma_m^2 \approx N_0^2 \exp(-2\alpha \ell) E \left\{ \int_{c_i} \alpha_1 ds \right\}^2 \quad (4.24)$$

By characterizing the material with $u(c_i) = \int_{c_i} \alpha_1 ds$ and

$$E[u(\Delta c_i) u(\Delta c_j)] = \sigma_a^2 \delta(\Delta c_i, \Delta c_j) \quad (4.25)$$

one obtains for a "white noise" model of material density variation

$$\delta(\Delta c_i, \Delta c_i) = \Delta c_i \quad (4.26)$$

$$\delta(\Delta c_i, \Delta c_j) = 0 \quad i \neq j.$$

The total measured noise due to material density variation is then given by

$$\sigma_m^2 = \underline{N_0^2} e^{-2\alpha \ell} \cdot \ell \cdot \sigma_a^2 = N_i^2 \ell \sigma_a^2 \quad (4.27)$$

Observe the second power in the photon count.

The contribution due to photon statistics is simply

$$\sigma_{ph}^2 = \underline{N_0} e^{-\alpha \ell} = N_i \quad (4.28)$$

and depends linearly on photon count. Finally, noise due to amplifiers

and background radiation is independent of the object and hence

$$\sigma_c^2 = N_0^0 \cdot \text{const}_1 = N_i^0 \cdot \text{const}_2 \quad (4.29)$$

Performance for multiscan. In this case several ways exist to combine measurements and noise terms to specify a signal-to-noise ratio.

A simple way would be to add for p projections signals ΔN_i due to a flaw, e.g. form

$$\Delta N = \sum_{i=1}^p \Delta N_i \quad (4.30)$$

In this case one would try to minimize

$$f = \frac{\sum_{i=1}^p N_{0i}^0 \text{const} + N_{0i} e^{-\alpha_0 \ell_i} + N_{0i}^2 e^{-2\alpha \ell_i} \cdot \ell_i \cdot \sigma_a^2}{\sum N_0 e^{-\alpha_0 \ell_i} e^{\alpha d_i}} \quad (4.31)$$

Special cases are interesting for understanding the behavior of Equation 4.31.

Let the noise due to the material dominate. In this case

$$f \propto \frac{\sum N_i^2}{\sum N_i} = N_i^2$$

Simplify by assuming $\ell_i = \ell_j = \ell$; then by $N_0 = N_i e^{\alpha \ell}$ and $N_{\text{tot}} = \sum_i N_{0i}$

$$f \propto \frac{\sum_{i=1}^p N_0^2}{N_{\text{tot}}} \quad (4.33)$$

As far as the optimal distribution of incident intensities is concerned clearly $N_{0i} = \frac{1}{p} N_{\text{tot}}$ should be chosen. In this case

$$f \propto \frac{1}{p} \quad (4.34)$$

This suggests to use a large number of projections p to obtain much information about the presence or absence of a flaw. (compare results in Equation 4.39).

It would be interesting to see how intensities should be distributed when path lengths are different. For a two-scan technique and a rectangular object of dimension ℓ_1 and ℓ_2 the problem may be solved analytically when σ_m^2 is dominant. The lengthy derivation (omitted here) suggests for $\ell_2 = \ell_1 + \Delta\ell$ $\Delta\ell \ll \ell_1$, that to a first approximation equal intensities should be used along the dimension ℓ_1 and ℓ_2 . It is only in the higher terms of $\Delta\ell$ that differences in intensity distribution arise. A second interesting case is $\ell_2 = 2\ell_1$. In this case it is found that the N_i should be kept very nearly the same with $N_2 \sim 80\%N_1$. However incident intensity (at constant beam hardness!) would give $N_{02} \sim 6N_{01}$, while $N_0 = N_{01} + N_{02}$ is kept fixed.

We present these results merely as illustrations. In more general situations other noise terms have to be considered, the possibility of variable beam hardness (especially when using the pencil beam) should be incorporated in the model and clearly only numerical techniques can find "optimal" solutions to Equation 4.31. With variable beam hardness one has also to include the variable radiation characteristics of X-ray tubes in the forward direction (Equation 3.8) and variable scatter. Furthermore it appears that instead of ΔN in Equation 4.30 a weighted set of measurements should be formed, e.g.

$$\Delta N = \left[2 \sum_{i=1}^p \left(\frac{\Delta N_i}{\sigma_i} \right)^2 \right]^{1/2} \quad (4.35)$$

For such an expression analytic optimization is unfeasible and numerical techniques are called for.

4.3.4 Uncertainty in multiscan when beams overlap

An important generalization occurs when beams have much overlap as

illustrated in Figure 4.8 . The question is - how does performance of an estimation scheme deteriorate due to this overlap?

Consider stripes $i=1\dots p$. Assume that each stripe has an area a_{ii} and overlaps strips j over an area a_{ij} . Thus the covariance of the measurements y_i with those of stripe j (assuming material density to be uncorrelated between different points) is described by (neglecting quantum mottle)

$$\Sigma = \text{cov}(y, y^T) = \sigma^2 A = \begin{bmatrix} a_{11} & \cdot & \cdot & a_{1p} \\ \cdot & \cdot & \cdot & \cdot \\ \cdot & \cdot & \cdot & \cdot \\ a_{p1} & \cdot & \cdot & a_{pp} \end{bmatrix} \Delta_{\sigma^2}^{-1} = \sigma^2 \begin{bmatrix} \gamma_{11} & \cdot & \cdot & \gamma_{1p} \\ \cdot & \cdot & \cdot & \cdot \\ \cdot & \cdot & \cdot & \cdot \\ \gamma_{p1} & \cdot & \cdot & \gamma_{pp} \end{bmatrix}^{-1} \quad (4.36)$$

When these stripes intersect on a void of unknown size, say ε , we wish to find an estimate $\hat{\varepsilon}$. The best estimate in the sense of a quadratic loss function is found by determining w.r.t. $\hat{\varepsilon}$

$$\min(\underline{y} - \hat{\varepsilon} \begin{bmatrix} 1 \\ 1 \\ 1 \end{bmatrix})^T \Sigma^{-1} (\underline{y} - \hat{\varepsilon} \begin{bmatrix} 1 \\ 1 \\ 1 \end{bmatrix}) \quad (4.37)$$

As a measure of information we may use now the variance which we obtain from this estimate. With a flat prior distribution $p(\varepsilon)$ and the Gaussian distribution of y (justified from the central limit argument when many local density variation within stripe i cause the variation of y_i) it follows from Bayes theorem (Equation 2.18) and $p(\varepsilon|y) \propto p(y|\varepsilon)$

$$\text{var}[\hat{\varepsilon}] = \sigma^2 \begin{bmatrix} p & p & \\ \sum_{i=1} & \sum_{j=1} & \gamma_{ij} \end{bmatrix}^{-1} \quad (4.38)$$

When we assume for simplicity $a_{ii}=1$, $a_{ij}=0$ (nonoverlapping) then clearly $\gamma_{ii}=1$, $\gamma_{ij}=0$ and hence

$$\text{var}[\hat{\varepsilon}] = \sigma^2 / p. \quad (4.39)$$

If however almost all of the stripes overlap possibly yielding

$$\Sigma = \sigma^2 \begin{bmatrix} 1 & 1-\delta & 1-2\delta & 1-(p-1)\delta \\ 1-\delta & 1 & 1-\delta & \cdot \\ & & \cdot & \\ 1-(p-1)\delta & \cdot & \cdot & 1 \end{bmatrix}, \delta > 0 \quad (4.40)$$

(for small δ) it is somewhat more difficult to find $\text{var}(\hat{\epsilon})$. One of the difficulties is, that although for small δ explicit expression for approximations to γ_{ij} and $|A|$ can be found (the determinant is approximately 2δ and $\sum \gamma_{ij} \approx 1$) this first order expansion is unfortunately insufficient to describe the precise behavior in which $\text{var}(\hat{\epsilon})$ decreases with δ .

However the explicit solution for $p=2$ can easily be found and gives

$$\text{var}_2(\hat{\epsilon}) = \sigma^2 \sum_{i=1}^2 \sum_{j=1}^2 \gamma_{ij}^{-1} = \frac{2-\delta}{2} \sigma^2 \quad ; 0 \leq \delta \leq 1 \quad (4.41)$$

Observe, for $\delta=0$ (complete overlap of two stripes) this gives the result for a single stripe, $\sigma^2/p_1 = \sigma^2$. In the other extreme, no overlap is represented by $\delta=1$ and gives the result $\sigma^2/p_2 = \sigma^2/2$ in agreement with Equation 4.39.

4.3.5 Collimators

It appears the importance of well designed collimators cannot be overemphasized. Some basic considerations indicate the use of rather large devices when compared to the object size. Here we present a simple model and its idealization. The derivations are by no means rigorous as the necessary integrations, for quantifying collimator performance precisely, are too complicated. Nevertheless, a useful description seems to result.

Consider the arrangement of Figure 4.9. In order to characterize the performance of this device we wish to describe its directivity much in the same way as is done for antennas at radiofrequencies or with

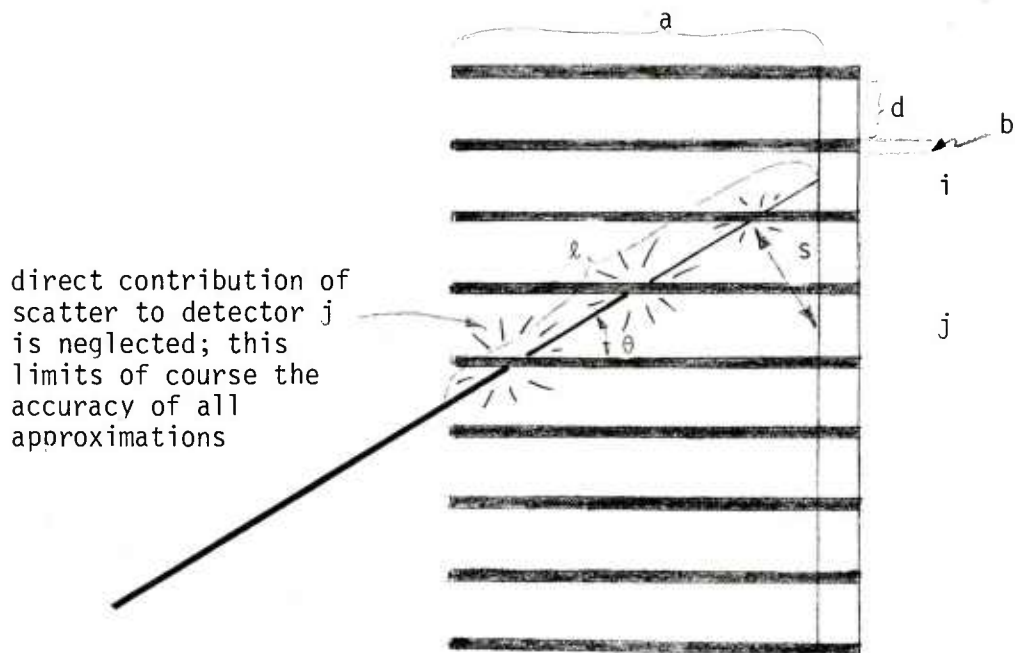


Figure 4.9: Attenuation of a X-ray beam which is not aligned with direction of blades in collimator. For the model it is assumed that $(b+d) \ll (\alpha^{-1}, \tau^{-1})$, (the absorption coefficient, and scatter coefficient respectively,) and $a \gg \alpha^{-1}$; in this event the scattered intensity field of a pencil beam may be assumed (Equation 4.7) and the scattered radiation reaching a detector directly may be neglected (especially in the case when $d \ll b$).

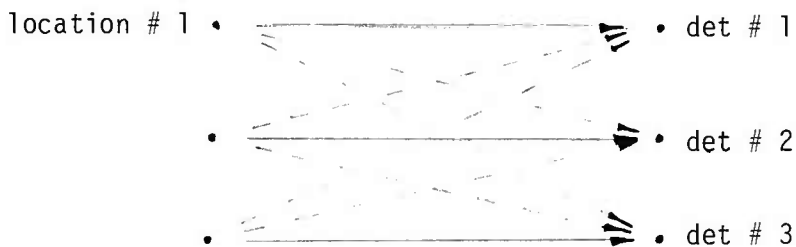


Figure 4.10: Schematic of crosstalk between channels due to imperfect collimation - e.g. any material density variation at location # 1 has effects on all detectors via scattered, and by the collimator imperfectly rejected, beams.

microphones. We assume a thin pencil beam with crosssectional area P and total flux I_0 is incident. Now we separate the problem into three parts. First we describe the fraction I of the intensity I_0 which reaches a detector without passing through any of the fans. Next we find the intensity when the beam passes through the blades; and finally we evaluate the amount of scattered radiation reaching a detector. The derivations assume short enough wavelength λ of X-rays so that no reflection mechanisms due to a narrow glancing angle of a fan relative to the beam occurs.

From geometry, the intensity reaching a detector i in a free path, averaging overall possible positions of the pencil beam is

$$\begin{aligned} I_d &= I_0 \cdot \frac{d}{b} \max [0, d - a \cdot \tan(\theta)] \\ &\approx I_0 \frac{d}{b} \max [0, d - a \cdot \theta] \end{aligned} \quad (4.42)$$

Second, the intensity of a more strongly tilted beam incident on detector i , but attenuated by the blades is given by

$$I_1 = I_0 \cos(\phi) e^{-\alpha \ell \delta} \quad (4.43)$$

where $\delta = b/d$ and $\ell = a/\sin \phi$. The remaining problem is to evaluate the scattered radiation. Note, here, a contribution not only to detector i but to any detection j occurs and may be summarised as "crosstalk" between detector channels. Its evaluation is based on bounding and roughly guessing the value of certain integrations.

Consider at first the scattered radiation received by detector j . Provided the detector is at some distance $s > \alpha^{-1}$ from the primary beam (Figure 4.9) one may replace that value by α^{-1} and bound the intensity received by the detector (we require actually all dimensions, except ℓ , to be much shorter than α^{-1} so that we may treat the collimator as homogeneous material)

$$I_2 < \alpha^2 \tau (\lambda \delta) (\Delta d) I_0 e^{-\alpha \delta a} \quad (4.44)$$

where (Δd) is the total detector area. For detector i , (which is also receiving the primary beam) the scattered radiation will be larger presumably by a factor of the order of e . With this assumption we write for any detector as a bound on scatter (corresponding to channel crosstalk, including detectors near i)

$$I_2' < \alpha^2 \frac{a}{\sin \phi} \frac{\Delta d^2}{b} \cdot I_0 e^{-\alpha \frac{ab}{d}} + 1 \quad (4.45)$$

The total intensity at detector j , $j \neq i$ is then by Equations 4.43 and 4.45

$$I_3 < \left[\frac{\alpha^2 \tau a \Delta d^2}{b \sin \phi} + \cos \phi \right] I_0 e^{-\alpha \left(\frac{ab}{d} \right) + 1} \quad (4.46)$$

where the dimension of α and τ are in cm^{-1} . From this rough bound the importance of a large $\alpha \frac{ab}{d}$ is seen. (long narrowly spaced blades of collimator).

The result suggest that flat beams can create much "noise" due to crosstalk. This problem is characterized for beams $i=1 \dots n$ and detectors $j=1 \dots n$ by what the detectors see. [Figure 4.10]. Let g_{ij} be the contribution of the i^{th} beam to the j^{th} detector, $g_{ii}=1$, $g_{ij}=\delta$ for $i \neq j$. Then for any disturbance ϵ_i in the i^{th} beam, the detectors receive a variation of signal, say γ_i proportional to ϵ_i and receive noise. Formally

$$\underline{\gamma} = [g_{ij}] \underline{\epsilon} + \underline{n} = \begin{bmatrix} \gamma_1 \\ \gamma_2 \\ \vdots \\ \gamma_n \end{bmatrix} = \begin{bmatrix} 1 & \delta & \delta & \delta \\ \delta & 1 & \delta & . \\ \delta & & 1 & . \\ \delta & . & . & 1 \end{bmatrix} \begin{bmatrix} \epsilon_1 \\ \epsilon_2 \\ \epsilon_i \\ \epsilon_n \end{bmatrix} + \underline{n} \quad (4.47)$$

where $\text{cov}[\underline{n} \ \underline{n}^T] = \sigma^2 \mathbf{I}$. Estimating $\underline{\epsilon}$ e.g. by least squares gives

$$\hat{\underline{\epsilon}} = E[\underline{\epsilon}] = [G^T G]^{-1} G^T \underline{\gamma} \quad (4.48)$$

with

$$\text{cov}[\underline{\varepsilon}] = \sigma^2 [\mathbf{G}^T \mathbf{G}]^{-1} = \sigma^2 \begin{bmatrix} [1+(n-1)\delta^2] & 2\delta+(n-2)\delta^2 & 2\delta+(n-2)\delta^2 & \vdots \\ 2\delta+(n-2)\delta^2 & \ddots & \ddots & \vdots \\ & & [1+(n-1)\delta^2] \end{bmatrix}^{-1} \quad (4.49)$$

This matrix is ill conditioned for large n . In particular large variances of ε_i occur, when, roughly speaking, $2\delta n > 1$. If this happens a pencil beam will presumably yield superior performance for estimating $\underline{\varepsilon}$, outweighing the time savings for generating high X-ray intensities in the flat beam (e.g. fan beam) configuration. This result allows one to choose $\alpha \frac{ab}{d}$ in Equation 4.46 when fan beams are considered.

5. COMPARISON OF PERFORMANCE OF STATE OF THE ART CT AND LIMITED SCAN FLAW DETECTION

Comparison of performance of state-of-the-art computed tomography and limited scan flaw detection should be based on

- i) computational complexity (time);
- ii) data-acquisition time;
- iii) error rates.

For several reasons no general conclusion about the superiority of one or the other method can be given. The preference will depend mainly on object size, material density variations within the object (homogeneity), and the characteristics of the flaw (e.g. void and/or cracks).

5.1 Computational complexity

In order to characterize computation complexity and function $O(N)$ is defined. A function $f(n)$ is $O(n)$ when $f(n)/N \rightarrow c$ for $N \rightarrow \infty$, where c is an arbitrary fixed number. In what follows this constant will usually be of the order 2...10. For example $f(N)=3N^2$ is $O(N^2)$.

Fast reconstruction algorithms in state-of-the-art CT require $O(p^s q^t)$ arithmetic operations, where $s+t=3$ [Reference 30], p is the number of projections and q the number of detector elements. These quantities are specified for any CT scanner. Typically $q=100...300$ and $p = 100...200$. Thus somewhere in the neighborhood of $10^7...10^9$ operations have to be performed for image reconstruction. By means of dedicated hardware (array processors) reconstruction times today are several tens of seconds.

The analysis of limited scan flaw detection is in principle divided into two parts. The first is to find approximations for the

projections of an object of known shape. This part which has to be performed only once for any test objects requires $O(n^2p)$ operations as each of n^2 pixels (or other orthogonal expansion of the image) has to be projected on p scan directions. In our situation we will typically have $q=n$, for reasons explained in section 4.1.

The second step, detection of a flaw requires only the evaluation of a quadratic form without crossterms between detectors (there would be some crossterms when consideration is given to imperfect collimation. This however would change the operations count only by a multiplicative constant). Thus, including removal of polynomials (see Section 4.2), other signal conditioning and executing a procedure, such as the sequential probability ratio test (Section 2.34), the total operations count is, for p scans, $O(pq)$. Depending on the particular problem, p is much smaller than for full scan CT. One may therefore anticipate to cut the operations count per object examination by a factor of 1000.

5.2 Data Acquisition Time

For current CT scanners anode heat loading (pulsed, up to 100kW) poses the major limitation for data acquisition [Reference 5]. One of the problems is a restriction on the size of the anode because the X-ray tube has to be moved around the patient. When stationary tubes (possibly with rotating anode in order to allow small focal spots) could be used, larger continuous power outputs may be achieved. When multiple scans are necessary the possibility of rotating an object may be considered.

One of the possible advantages in case of the limited scan approach is the use of larger and more effective collimators than those used in

state-of-the-art CT scanners. In this situation dose requirement may be reduced, cutting exposure time. The problem can be studied numerically following Section 4.3.4.

Another advantage in the limited scan tomography arises when a sequential approach is taken. For example, one may start out to take two orthogonal projections of an object; they should determine the presence of any voids or gross structural defects. Next, when this test is passed one may invest time by a sequential projection method to rule out the presence of any cracks-which are harder to detect. In this way time can be saved mainly when large defects are frequent and when they require an object to be discarded.

5.3 Error Rates

For the sake of simplicity of comparison we will assume either an error free human observe of CT images or, equivalently, optimal processing of image information by signal detection techniques. After this simplification, performance with regard to error rates has two aspects. First, there is a theoretical error rate which one arrives at from a particular model. Second there is the error rate which can acutally be achieved.

The error rates are strongly dependent on the character of noise. For CT-scanners this problem has been studied theoretically [References 18, 24]. However, the models used are highly idealized with regard to the structure of the projection matrix A , e.g. it neglects the spread of the receptive field of any detector or channel crosstalk [Section 4.3.4] This suggest that at some distance from the detector resolution is overestimated and the noise level underestimated. It is apparently for this reason that theoretical treatments agree with measurements of CT

image noise only for the low spatial frequency range [Reference 18]. Equivalently, only detection of large objects is well described by these analysis. However, for flaw detection the interest is mainly in the capability to detect small objects such as cracks. As a consequence of these inaccuracies an object may be regarded as free of flaws despite the possible presence of a flaw.

Thus, for any particular problem setting the following approaches exist for finding useful solutions to above problem. For the limited scan technique a numerical evaluation of certain matrices is feasible and could allow evaluation of precision of estimates (e.g. in the sense of Equation 4.49). This result could be compared to the empirical data of CT scanners [(Reference 44; their Figures 8 and 9)]. Alternatively, by a combination of numerical and analytic techniques the behavior of very large matrices as they arise in full scan CT might be extrapolated from smaller matrices and permit more precise theoretical prediction of state-of-the-art CT performance when large objects have to be considered.

Currently, in order to evaluate full scan CT performance phantoms are used to determine the noise and resolution, and thus sensitivity. When sensitivity is insufficient for a particular purpose dose, and with it exposure time, have to be increased. With reduced noise (due to quantum mottle) filter functions which yield higher spatial resolution (compare Section 2.1) can be used. Nevertheless it appears that information is wasted; it would appear necessary to use generalizations of the reconstruction algorithm as suggested in Section 2.1.

In this respect the limited scan may offer some advantages. In limited scan typically only the forward problem of projections has to be solved (much prior information). For the forward problem, however, the use of a more sophisticated projection matrix is feasible for describing the receptive field of a detector more accurately. This is mainly a consequence of the relative simplicity of solving the forward problem when compared with the inversion problem. Thus it would be feasible to parameterize the receptive field of a detector (expressed in the elements of the projection matrix A) and use regression or some other parameter estimation technique to identify it, e.g. the matrix could be calibrated. For limited scan it seems to be feasible (say $p \approx 10$) to actually evaluate the covariance structure of measurements and the variance of estimates of flaws (similar to the techniques of Section 4.3.4 and 4.3.5). The possibility to evaluate the covariance structures would be mainly possible due to matrices smaller than in full scan CT but also due to better conditioning of the various matrices involved (smaller ratio of largest to smallest eigenvalue due to stronger diagonals). In this way a sequential procedure can be designed which stops more precisely at the time when enough information about an object has been acquired to decide about the presence or absence of a flaw.

In retrospect, it appears that the driving force for modeling here is the goal to achieve a low risk associated with missing flaws while keeping the speed of examination high. It is important to observe that the (believed) absence of flaws is what calls for a long continuation of performing scans. Once a flaw has been detected location and classification are fairly simple. Thus, rather than calling for a two stage technique for detecting flaws by the limited scan

technique with subsequent location by full scan CT, full scan CT could only be useful for examining those objects in which the limited scan technique was not capable to detect flaws. This would mainly apply to the situation where only a few cracks are present (see Section 4.1).

REFERENCES

1. Adamczewski, I., "The Absorption of X-rays and γ -rays", in Ionization, Conductivity and Breakdown in Dielectric Liquids, Taylor & Francis, Red Lion Court, London, 1969.
2. Akaike, H., (1974a), "Stochastic Theory of Minimal Realization," IEEE Trans. on Automatic Control, Vol AC-19, No 6, December, 667-674.
3. Alvarez, R., and Seppi, E., "A Comparison of Noise and Dose in Conventional and Energy Selective Computed Tomography", IEEE Trans. on Nuclear Sci., Vol. NS-26, No.2, April 1979.
4. Bard, Y., Nonlinear Parameter Estimation, IBM Corp., Academic Press, New York, 1974.
5. Braun, M., "Physics of X-ray Tubes For CT Scanners", IEEE Trans. on Nuclear Sci., Vol. NS-26, No. 2, April 1979.
6. Cho, Z.H., "General Views on 3-D Image Reconstruction and Computerized Transverse Axial Tomography", IEEE Trans. on Nuclear Sci., Vol. NS-21, supported by U.S. Atomic Energy Commission under Contract AT(04-1) GEN-12, June 1974.
7. Cho, Z.H., and Burger, J.R., "Construction, Restoration, and Enhancement of 2 and 3-Dimensional Images", IEEE Trans. on Nuclear Sci., Vol. NS-24, No. 2, April 1977.
8. Compton, A.H., and Allison, S.K., X-rays in Theory and Experiment, D. Van Nostrand Co., Inc., Princeton, N.J., 1954.
9. Cormack, A.M., "Reconstruction of Densities from Their Projections, with Applications in Radiological Physics", Phys. Med. Biol., 1973, Vol. 18, No. 2, 195-207.
10. Davison, M.E., "Filtered Backprojection Methods for Reconstructing a Function from an Arbitrary Finite Set of its Projections", Ph.D. Thesis, University of Calif., Berkeley, 1978.
11. DeGroot, M.H., Optimal Statistical Decisions, McGraw-Hill Book Co., New York, 1970.
12. Doi, Kunio, personal communication, Dept. of Radiol., Univ. of Chicago, (312) 947-5729.
13. Fukunaga, K., Introduction to Statistical Pattern Recognition, Academic Press, New York, 1972.

REFERENCES (cont'd)

14. Galvin, J.M., "In Vivo Determination of Attenuation Coefficients For Radiation Therapy", in Application of Optical Instrumentation in MEDICINE III, Proceed. of Soc. of Photo-Optical Instr. Engineers, August 1-2, 1974, Kansas City, Missouri.
15. Glocker, R., Materialprüfung mit Röntgenstrahlen, Springer-Verlag Berlin Heidelberg, New York, 1971.
16. Gordon, R., Herman, G.T., Johnson, S.A., "Image Reconstruction From Projections", Scientific American, October, 1975.
17. Gordon, R., "Dose Reduction in Computerized Tomography", Guest Editorial, reprint from Investigative Radiology, Vol. 11. No. 6, 1976
18. Hanson, K.M., "Detectability in Computed Tomographic Images", Am. Assoc. Phys. Med., 1979.
19. Hounsfield, G., Süsskind, C., "Biological Effects and Medical Applications of Electromagnetic Energy", in Proceed. of the IEEE, Vol. 68, No. 1, January 1980.
20. International Union of Crystallography, Tables relating to the Production, Wavelengths and Intensities of X-rays, in International Tables of X-ray Krystollography, Kynoch Press, 3rd edition, 1969.
21. Jazwinski, A.H., Stochastic Processes and Filtering Theory, Academic Press, New York, 1970.
22. Kaelble, E.F., Handbook of X-rays, McGraw-Hill Book Co., New York, 1965.
23. Kashyap, R.L., "Picture Reconstruction from Projections", IEEE Trans. on Computers, Vol. c-24, No. 9, September 1975.
24. Kelcz, F., Joseph, P.M., and Hilal, S.K., Noise Considerations in Dual Energy CT Scanning, Neurological Institute, Columbia-Presbyterian Medical Center, N.Y., 1979.
25. Klein, V.O., Nishina, Y., "Über die Streuung von Strahlung durch freie Elektronen nach der neuen relativistischen Quantendynamik von Dirac", in Zeitschrift für Physik, 52, p. 869, 1929.
26. Kramers, H.A., Phil. Mag 46, 836. 1923
27. Kulenkampff, H., Ann. d. Phys. 69, 548 (1922).
28. Kulenkampff, H., Ann. der Phys, 87, 579 (1928).

REFERENCES (cont'd)

29. Lee, Y.W., and Schetzen, M., "Measurement of the Wiener kernels of a Nonlinear System by Cross-Correlation," Int. J. Control, vol. 2, pp. 237-254, 1965.
30. Louis, A.K., "Picture Reconstruction from Projections in Restricted Range", Math. Meth. in the Appl. Sci. 2 209-220. (1980)
31. Mason, J.F., "Crack-Detectives Foil Aircraft Failure", IEEE Spectrum, February 1980.
32. McGonnagle, W.J., Nondestructive Testing, Gordon and Breach, New York, 1966
33. Nishina, V.Y., "Die Polarisation der Comptonstreuung nach der Diracschen Theorie des Elektrons," in Zeitschrift für Physik, 52, p. 853, 1928.
34. Radon, J., "Über die Bestimmung von Funktionen durch ihre Integralwerte längs gewisser Mannigfaltigkeiten, Berichte Saechsische Akademie der Wissenschaften 69 (1917) 262-277.
35. Rao, C.R., Linear Statistical Inference and Its Applications," John Wiley & Sons, Inc., New York, 1965.
36. Rockmore, A., The Maximum Likelihood Approach to Image Reconstruction, University Microfilms International, Michigan, 1977.
37. Sage, A.P., and Melsa, J.L., Estimation Theory with Applications to Communications and Control, McGraw-Hill Book Co., New York, 1971.
38. Schwarz, G., "Estimating the Dimension of a Model," The Annals of Statistics, Vol. 6, No. 2, 461-464, (1978).
39. Shapiro, E.G., and Anderson, A.L., "Dual Energy Analysis Using Phoswich Scintillation Detectors for Low-Level In-Vivo Counting", Univ. of Calif., Livermore, Calif,
40. Shepp, L.A., and Logan, B.F., "Reconstructing Interior Head Tissue From X-ray Transmissions," Bell Labs., Murray Hill, NJ, 1974
41. Shepp, L.A., and Logan, B.F., "The Fourier Reconstruction of a Head Section," IEEE Trans. on Nucl. Sci., Vol. NS-21, June 1974.
42. Sommerfeld, A., Prod. Nat. Acad. Sci, 15, 393 (1929). Annalen der Physik II, 257 (1931).
43. Stonestrom, J.P., and Macovski, A., "Scatter Considerations in Fan Beam Computerized Tomographic Systems", IEEE Trans. on Nuclear Sci., Vol. NS-23, No. 5, October 1976.

REFERENCES (concluded)

44. Wagner, R.F., Brown, D.G., Pastel, M.S., "Application of Information Theory to the Assessment of Computed Tomography", Med. Phys. 6(2), Mar./Apr. 1979.
45. Wozencraft, J.M., Jacobs, I.M., Principles of Communication Engineering, John Wiley & Sons, Inc., New York, 1965.
46. Zinke, O., and Brunswig, H., Lehrbuch der Hochfrequenztechnik, Springer-Verlag, New York, 1965.

BIBLIOGRAPHY

- Adhikari, B.C., Chanda, D.K., and Jana, S., "On the Determination of the Depth of a Planar Defect by Radiography," in Depth Determination of Planar Defect by Radiography, Materials Division, Central Mechanical., Eng. Res. Inst., West Bengal, India, 1977.
- Ault, G.M., and Freche, J.C., "Composites Emerging for Aeropropulsion Applications," NASA Lewis Research Center, 1979.
- Baily, N.A., "The Fluoroscopic Image as Input Data for Computed Tomography," IEEE Trans. on Nuc. Sci., Vol. NS-26, No. 2, April 1979.
- Brooks, R.A., et al, "Aliasing: A Source of Streaks in Computed Tomograms", in Journal of Computer Assisted Tomography, Raven Press, p. 511 New York, 1979.
- Budinger, T.F., and Gullberg, G.T., "Three-Dimensional Reconstruction in Nuclear Medicine Emission Imaging", IEEE Trans. on Nuc. Sci., Vol. NS-21, June 1974.
- Chan, J. L.-H., Alvarez, R.E., and Macovski, A., "Measurement of Soft Tissue Overlying Bone Utilizing Broad Band Energy Spectrum Techniques", IEEE Trans. on Nuc. Sci., Vol NS-23, No 1, Feb. 1976.
- Cho, Z.H., "3-Dimensional Radioisotope Imaging With Circular Ring Transverse Axial Positron Camera", Univ. of Calif., Los Angeles, Calif.,
- Cho, Z.H., and Chan, K., "A Comparative Study of 3-D Image Reconstruction Algorithms With Reference to Number of Projections and Noise Filtering", IEEE Trans. on Nucl. Sci. Vol. NS-22, Feb. 1975.
- Duerinckx, A.J., and Macovski, A., "Nonlinear Polychromatic and Noise Artifacts in X-ray Computed Tomography Images", in Journal of Computer Assisted Tomography, Raven Press, p. 519, New York, 1979.
- EPRI Journal, "NDE: In-Depth Search for Flaws", Vol. 5, No. 6. July/August 1980.
- Fenn, J.O., Frey, G.D., and Gajewski, W.G., "An Iterative Computer Routine for X-ray Spectra Generation: Technique and Application", Proc. 3rd Ann. Symp. Comp. Appl. Med. Care, Oct 14-17, 1979
- Fontijn, L.A., and Peugeot, R.S., An Operational 150 kV Microfocus Rod Anode X-ray System for Non-destructive Testing, IPC Business Press, 1978.
- Friedlander, B., Denton, R.V., and Rockmore, A.J., "The Inverse Problem in Radar and Optical Imaging", IEEE, WP8-4:30, 1978.

BIBLIOGRAPHY (cont'd)

- Fu, K.S., "First International Joint Conference on Pattern Recognition," Oct.-Nov. 1973, Washington, D.C.
- Gilbert, J.F., Carrick, D.P.A., "A High Energy Flash X-Ray Facility", British J. of NDT, 1973.
- Goncharov, V.I., Gorbunov, V.I., and Epifantsev, B.N., The Design of Automatic Control Systems in Radiation Flaw Detection, Plenum Publishing Corp. 1976.
- Gorbunov, V.I., and Melikhov, V.S., Semiconductor Detectors of Hard Bremsstrahlung in Flaw Detection, Plenum Pub. Corp., 1978.
- Gordon, R., "A Tutorial on ART (Algebraic Reconstruction Techniques)", IEEE Trans., on Nuc., Sci, Vol NS-21, June 1974.
- Gordon, R., "Dose Reduction in Computerized Tomography", Reprinted from Investigative Radiology, Vol. 11, No. 6, Nov.-Dec. 1976.
- Gordon, R., Herman, G.T., and Johnson, S.A., "Image Reconstruction From Projections", Scientific American, October, 1975.
- Gordon, R., and Herman, G.T., "Three-Dimensional Reconstruction from Projections: A Review of Algorithms", reprint by the U.S. Dept. of HEW.
- Gordon, et al, "Tomography Signal Processing System", United States Patent, Jan 16, 1979.
- Halmshaw, R., and Hunt, C.A., Can Cracks be Found by Radiography?, Wykeham Publications [London] Ltd. 1978
- Harrison, W.D., "The Significance of Defects with Regard to Castings", British Journal of NDT, London, April 1977.
- Hart, H.E., Warshaw, B., and Stoller, H.I., "Geometric Efficiency and Other Performance Characteristics of Focusing Collimators", IEEE Trans. on Bio-Medical Eng., Vol. BME-14, No. 2, April 1967.
- Hartmann, F., "Aerospace-AFML Conference on NDT of Plastic/Composite Structures", AF Materials Lab (MAMN), Wright-Patterson AFB, Ohio, 20 March 1969.
- Hawkesworth, M.R., "Practical Neutron Radiography," in Non-Destructive Testing Views, Reviews, Previews, Oxford Univ. Press, 1969.
- Hendee, W.R., Medical Radiation Physics, Year Book Medical Publ. Inc., Chicago, 1979.
- Herman, G.T., and Lung, H-P., "Reconstruction From Divergent Beams: A Comparison of Algorithms with and without Rebinning," Comput. Biol. Med. Vol. 10, pp. 131-139, 1980.

BIBLIOGRAPHY (cont'd)

- Horn, B.K.P., "Density Reconstruction Using Arbitrary Ray-Sampling Schemes", Proc. of the IEEE, Vol. 66, No. 5, May 1978
- Huddleston, A.L., Bhaduri, D., and Weaver, J., Geometrical Considerations for Compton Scatter Densitometry, Am. Assoc. Phys. Med. 1979.
- Jain, A.K., and Jain, J.R., Partial Differential Equations and Finite Difference Methods in Image Processing- Part II: Image Restoration, IEEE Trans. on Autom. Control, Vol. AC-23, No. 5, October 1978.
- Kaelble, E.F., Handbook of X-rays, McGraw-Hill, New York, 1967.
- Kak, A.C., Jokowatz, C.V., Jr., Baily, N.A., and Keller, R.A., "Computerized Tomography Using Video Recorded Fluoroscopic Images", IEEE Trans. on Biomed. Eng., Vol. BME-24, No. 2, March 1977
- Kambic, G.X., and Wake, R.H., "Computed Tomography With an X-ray Transmission Pencil Beam Scanner", IEEE Trans. on Nucl. Scien., Vol. NS-24, No. 2, April 1977.
- Kowalski, G., "Suppression of Scattered Radiation in Radiography and Improvement of Resolution by Spatially Modulated Intensity", Applied Optics/Vol. 15, No.3, March 1976.
- Lobaev, V.P., Kuchumov, G.V., and Leonov, B.I., "Statistical Analysis of Radioscopic Inspection Data", in Radiation Methods, Plenum Publishing Corp, New York,
- Macovski, A., Brody, W., Lehmann, L., Strul, B., and Yeh, P-S., "Future Trends in Projection Radiography", SPIE Vol. 206, Recent and Future Developments in Medical Imaging II, (1979).
- Muntz, E.P., "Analysis of the Significance of Scattered Radiation in Reduced Dose Mammography, Including Magnification Effects, Scatter Suppression, and Focal Spot and Detector Blurring", Med. Phys, 6(2), March/April 1979.
- Oppenheim, B.E., "More Accurate Algorithms for Iterative 3-Dimensional Reconstruction", IEEE Trans. on Nucl. Sci., Vol. NS-21, June 1974.
- Pang, S.C., and Genna, S., "Corrections For X-ray Polychromaticity Effects on Three-Dimensional Reconstruction", IEEE Trans. on Nucl. Scien., Vol. NS-23, No. 1, February, 1976.
- Parish, R.W., and Cason, D.W.J., "High Definition Radiography of Cast Turbine Blades as a Method of Detecting and Evaluating the Incidence of Microporosity", NDT International, August 1977.
- Phelps, M.E. et al, "Design Considerations for a Positron Emission Transaxial Tomograph (PETT III)", IEEE Trans. on Nucl. Scien, Vol. NS-23, No. 1, February 1976.

BIBLIOGRAPHY (cont'd)

- Pokrovskii, A.V., "Automatic Processing of Radiometric Data", in Radiation Methods, Plenum Publishing Corp, New York,
- Prasad, S.C., "Effects of Focal Spot Intensity Distribution and Collimator Width in Reconstructive X-ray Tomography^a", Med. Phys, 6(3), May/June 1979.
- Pullen, D.A.W., "Dynamic Radiography, using an Image Intensifier," NDT Centre, AERE, Harwell, November 1978.
- Redington, R.W., "Computed Tomography", SPIE Vol. 206 Recent and Future Developments in Medical Imaging II(1979).
- Rektorys, K., Survey of Applicable Mathematics, The M.I.T. Press,
- Robinson, A.L., "Making Nondestructive Evaluation a Science", SCIENCE, Vol. 205, 3 August 1979.
- Rockmore, A.J., and Macovski, A., "A Maximum Likelihood Approach To Transmission Image Reconstruction From Projections", IEEE, Joint Autom. Contr. Conf., pp. 782-786, San Francisco, 1977.
- Rumyantsev, S.V., et al, "Flaw Detection with Ionizing Radiation at the Eighth All-Union Conference on Nondestructive Physical Monitoring Instruments and Methods, Defektoskopiya, No. 6, pp. 107-112, June, 1978.
- Sanderson, J.G., "Reconstruction of Fuel Pin Bundles by a Maximum Entropy Method", IEEE Trans. on Nucl. Scien., Vol. NS-26, No. 2, April 1979.
- Schnitger, D., and Mundry, E., "Improvements of Contrast of X-ray Images by the Use of Filters Between the Specimen and Film", British Journal of NDT, November 1976.
- Shepp, L.A., Kruskal, J.B., and Logan B.F., "Computed Tomography: The New Medical X-ray Technology", AMS and MAA meetings in Toronto Canada, August 24, 28, 1976.
- Siedband, M.P., Jennings, R.J., Eastgate, R.J., and Ergun, D.L., "X-ray Beam Filtration for Mammography", SPIE Vol. 127 Optical Instrumentation in Medicine VI (1977).
- Silyuk, V.F., "Selection of Certain Optimal Parameters of a Gamma-Ray Flaw Detector with Analog Data Processing", in Radiation Methods, Plenum Publishing Corp., New York, 1976.
- Smith, P.R., Peters, T.M., Muller, H.R., and Elke, M., "Towards the Assessment of the Limitations on Computerized Axial Tomography", Neuroradiology 9, 1-8, Springer-Verlag, 1975.
- Sondhi, M.M., "Image Restoration: The Removal of Spatially Invariant Degradations", Proc. of the IEEE, Vol. 60, No. 7, July 1972.

BIBLIOGRAPHY (concluded)

Synder, D.L., and Cox, J.R., Jr., "An Overview of Reconstructive Tomography and Limitations Imposed by a Finite Number of Projections", supported in part by Picker Corp, Cleveland Ohio.

U.S. Army Materiel Command, "Quality Assurance Guidance to Nondestructive Testing Techniques", AMCP 702-10, April 1970.

Varoutas, P.P., Nardizzi, L.R., and Stokely, E.M., "Digital Image Processing Applied to Scintillation Images from Biomedical Systems," IEEE Trans. on Biomed. Eng., Vol. BME-24, No.4, July 1977.

Waller, V.I., "Die Streuung von Strahlung durch gebundene und freie Elektronen nach der Dirac'schen relativistischen Mechanik," Proc. Roy. Soc. London (A) 126, 360, 1930.

Warren, B.E., X-ray Diffraction, Addison-Wesley Publ. Co., Reading, 1969.

Wiener, N., "Nonlinear Prediction and Dynamics", Proc. Third Berkeley Symp. Math. Stat. and Probability, Vol. 3, Univ. of Calif. Press, pp. 247-252, 1956.

Appendix A2.1

Evaluation of $A^* = \frac{\partial b}{\partial a}$.

Recall from Section 2.2 $a(k)=a(i,j)$, $k= (n-1)i+j$, and from Equation (2.36)

$$b(i) = -\ln(I_i/I_0) + \frac{1}{2I_i}$$

By Equation (3.14) with $f=\mu\rho$,

$$b(i) = \iint_A f(x,y) dx dy + \frac{1}{2I_0} \exp \iint f(x,y) dx dy.$$

Furthermore from the convention of Equation 2.9 about pixels (with unit area)

$$b(i) = \sum_j a(\ell,j) + \frac{1}{2I_0} \exp \sum_j a(\ell,j)$$

and hence

$$\frac{\partial b(i)}{\partial a(j)} = \begin{cases} (1 + \frac{1}{2I_i}) & ; \quad \text{if pixel } a(k) \text{ in stripe } b(i) \\ 0 & ; \quad \text{otherwise} \end{cases}$$

follows.

Thus A^* differs from A only by a factor $(1 + 1/2I_i)$ in row i . This can be expressed as shown in Equation 2.37.

Appendix A2.2

Computation of variance of cross product term $\underline{\epsilon}^T M \underline{x}$.

This computation utilizes the patterned structure of $(AA^T)^{-1} = M$ (as shown for $n \leq 4$ in Tables 2.1-2.4) and the asymptotic values of the coefficients t_i in Equation (2.51). Select two rows corresponding to orthogonal directions, e.g. $k=1$ and $\ell=n+1$. From this, for the 2-scan technique,

$$\begin{aligned}
 y &\approx \text{var}[2\epsilon\sigma_a^{-2} \left(\frac{1}{n} x_1 - \frac{1}{n^2} x_2 - \frac{1}{n^2} x_3 - \dots - \frac{1}{n^2} x_n \right. \\
 &\quad \left. + \frac{1}{n} x_{n+1} + 0 + 0 + \dots + 0 \right)] \\
 &= 4\epsilon^2 \sigma_a^{-4} \left[E\left[\sum_i \sum_j \cdot \frac{1}{n^4} x_i x_j \right] + E\left[\sum_{i \neq k} \frac{1}{n^3} x_k x_i \right] \right. \\
 &\quad \left. + E\left[\sum_{j \neq \ell} \frac{1}{n^3} x_\ell x_j \right] + E\left[\frac{1}{n^2} (x_k^2 + x_\ell^2) \right] \right] \\
 &= 4\epsilon^2 \sigma_a^{-4} \sigma_a^2 \left[o(n^2) + o(n^2) + o(n^2) + \frac{2}{n} \right]
 \end{aligned}$$

Hence we obtain approximation Equation 2.67

$$y \approx 4\epsilon^2 \sigma_a^{-2} 2n^{-1} = 8(\epsilon/\sigma_a)^2 n^{-1}$$

Appendix A3.1

Models for X-ray Intensity $I(\lambda, U)$ from tubes

The similarity of spectra for different tube voltages (Figure 3.3) suggests that all spectra are related by

$$c_1 I(\lambda_1 \cdot U_1) = c_2 I(\lambda_2 \cdot U_2)$$

An important question is how the constant c depends on U under this condition. For this purpose recall Equation 3.10 and regard P_a as the anode heat dissipation. With this notation

$$\eta = \alpha U = \frac{c(U) \int I(\lambda \cdot U) d\lambda}{P_a} = \frac{c(U) \int I(\lambda \cdot U) d\lambda}{U \cdot J}$$

where J is the anode current. For $J = \text{constant}$ and $\lambda U = a$

$$\alpha \cdot U^2 = \frac{c(U)}{U} \int_{a_{\min}}^{\infty} I(a) da = \frac{c(U)}{U} \text{ const.}$$

This leads to

$$c(U) = \alpha'' U^3 \triangleq (U/U_0)^3$$

Alternatively when P_a is constant, such as when heat dissipation limits tube performance one obtains immediately

$$I(\lambda, U) = (U/U_0)^2 I(\lambda \cdot U).$$

Appendix A3.2

Relation of X-ray quanta to tube voltage

The energy of a single quantum is $E = h\nu$. Thus the number of quanta in a band $d\lambda$ are

$$S_{\lambda} = \frac{I_{\lambda}}{E} = \frac{I_{\lambda}}{h\nu} = \frac{I_{\lambda}}{h \cdot c} \lambda$$

The total number of quanta in the spectrum is

$$S_{\text{tot}} = \int_{\lambda_{\text{min}}}^{\infty} S_{\lambda} d\lambda = K \int \lambda I_{\lambda} (\lambda \cdot U) d\lambda$$

where by Appendix A3.1

$$I_{\lambda} = \left(\frac{U}{U_0} \right)^n I_{\lambda} (\lambda \cdot U) \quad \begin{cases} n = 3 & \text{for constant current } J \\ n = 2 & \text{for constant heat dissipation} \end{cases}$$

Thus, with $\lambda U = a$ and $U d\lambda = da$

$$\begin{aligned} S_{\text{tot}} &= K \frac{\lambda}{U} \int \left(\frac{U}{U_0} \right)^n I(a) da \\ &= K' U^{(n-2)} \int_{a_{\text{min}}}^{\infty} a I(a) da = K'' U^{(n-2)} \end{aligned}$$

Hence the number of quanta grows proportional to the tube voltage at constant current $J(n=3)$ but remains fixed for constant heat load of the anode ($n=2$).

Appendix A3.3

Noise due to conversion of X-ray photon into secondary particles

Assume x secondary particles are generated per X-ray photon and, because of finite X-ray energy

$$0 \leq x \leq n_{\max} .$$

The distribution for x with maximum entropy (worst case) under this condition is the uniform distribution

$$x \sim U[0, n_{\max}]$$

For this distribution

$$E[x] = n_{\max}/2$$

and

$$\text{var}[x] = (n_{\max})^2/12$$

The relative uncertainty of a measurement of secondary particles is described (independently of the number of secondary particles) by

$$u = \frac{\sqrt{\text{var}[x]}}{E[x]} = \frac{1}{\sqrt{3}}$$

However it appears more plausible to assume for the distribution of x one which peaks near $E[x]$. A Poisson variate (which represents counting statistics) seems to be a more reasonable model. In that case one would obtain

$$u = [E(x)]^{-1/2} .$$

In other words uncertainty diminishes as the average number of secondary particles increases. This model seems to be useful for a situation where physically secondary particles are generated independently along the trajectory of the X-ray photon through the detector.

Another rather extreme model would be to assume each photon's energy is completely converted into secondary particles. In that event no uncertainty would arise. This model could be viewed as unrealistic and one may consider a model in which after complete conversion of an X-ray photon into one species of secondary particles, a fraction escapes. This latter assumption leads to a multinomial distribution for the measured particles which gives again

$$u \propto [E(x)]^{-\frac{1}{2}}$$

Appendix A3.4

Estimation of spectral channel width of X-ray detector

Assume, on the average, a number λ of secondary particles are generated independently by the X-ray photon. In this case the number x of secondary particles obeys a Poisson variate and

$$E[x] = \mu = \text{var}[x].$$

Assume furthermore the parameter λ depends linearly on the energy of the incident X-ray, and let λ be large, say $\lambda > 10$.

Consider now two X-rays with energy E_1 and E_2 where

$$E_1 = h\gamma_1 = \frac{h c}{\lambda_1} = a\mu_1$$

$$E_2 = h\gamma_2 = \frac{h c}{\lambda_2} = a\mu_2$$

Then the two distributions for the two X-ray beams are approximated by

$$x_1 \sim N\left(\frac{h c}{a\lambda_1}, \frac{h c}{a\lambda_1}\right)$$

$$x_2 \sim N\left(\frac{h c}{a\lambda_2}, \frac{h c}{a\lambda_2}\right)$$

When the two distributions can be well separated they may be regarded as corresponding to separate channels. A typical value for such separation is the use of a "2- σ distance".

Thus we can describe channel separation for two wavelength by

$$\sqrt{\frac{h c}{a\lambda_1}} + \sqrt{\frac{h c}{a\lambda_2}} = \left| \frac{h c}{a\lambda_1} - \frac{h c}{a\lambda_2} \right|$$

This expression can be solved approximately by Taylor series expansion for small $\Delta\lambda/\lambda = (\lambda_2 - \lambda_1)/\lambda_1, (\lambda_2 > \lambda_1)$. One obtains

$$\sqrt{\frac{hc}{a\lambda}} \left(2 - \frac{\Delta\lambda}{2\lambda} \right) \approx \left| \frac{hc}{a\lambda} \frac{\Delta\lambda}{\lambda} \right|.$$

This expression can be rearranged to give the relative channel width

$$\frac{\Delta\lambda}{\lambda} = \frac{2}{(\sqrt{\mu} + \frac{1}{2})} \approx 2\mu^{-1/2}$$

where $\mu = hc/a\lambda$.